Computational Modelling of Failure Mechanisms in Fibre Metal Laminates

University of Sheffield

Ibrahim Hamed Ali Abuzayed

A thesis is submitted towards the fulfilment requirements for the degree of

Doctor of Philosophy

Supervised by
Dr. Jose Luis Curiel-Sosa

The Department of Mechanical Engineering

At The University of Sheffield

June 2024

Abstract

In this thesis, a numerical framework is developed for predicting the mechanical behaviour and failure mechanisms of Fibre Metal Laminates (FMLs). Modelling the behaviour of these materials is challenging due to the diverse material behaviours of its constituents, combined with the heterogeneous nature of composites, which result in various failure modes. In order to accurately predict the damage process of these materials, a 3D damage model is required. Therefore, a comprehensive 3D finite element model incorporating various material models, failure criteria and damage evolution laws has been developed. In this model, a user-defined subroutine is developed in Fortran and linked with the Finite Element (FE) solver Abaqus/Explicit. Through this subroutine, physically verified theories are utilized for predicting the onset of damage in composites. A criterion for predicting the fracture plane at the onset of failure in composites is implemented where the efficiency of the subroutine is enhanced by implementing a fast search algorithm. The damage propagation is simulated with an evolution law, modified to align with the damage initiation criteria. Additionally, the crack paths are predicted by deleting the failed elements using volume-based criteria. The subroutine is validated by comparing the results of a simulated tensile test of CFRP with experimental data, which demonstrated excellent agreement between the stress-strain curves and reasonable prediction of the failure modes.

The framework is applied for simulating two mechanical tests: the open-hole tensile test of GLARE and the flexural test of CARALL. In both studies, the conditions of the experimental setup were replicated in the FE models and the specimens were tested at both on-axis and off-axis fibre angle orientations. Mesh sensitivity studies were conducted to ensure the accuracy of the results and the predicted stress-strain curves showed overall excellent agreement with experimental data. Additionally, the studies highlighted the failure modes captured during the simulations, where the FE models successfully distinguished between fibre and matrix damage modes, plastic deformation and delamination.

Acknowledgements

Nomenclature

Abbreviations

2D	Two dimensional
3D	Three dimensional
ARALL	Aramid Reinforced Aluminium Laminate
CARALL	Carbon fibre laminates and aluminium
CDM	Continuum damage mechanics
CFRP	Carbon fibre reinforced polymers
CLT	Classical laminate theory
CZM	Cohesive zone model
d	Damage variable
E	Youngs modulus
EGSS	Extended Golden Section Search
FE	Finite element
FML	Fibre metal laminates

FPF	First ply failure
FRP	Fiber reinforced polymer
G	Shear modulus
Gc	Energy dissipation
GFRP	Glass fibre reinforced polymers
GSS	Golden Section Search
IFF	Inter fibre fracture criterion
MFB	Master fracture body
RVE	Representative volume element
SPIS	Simple parabolic interpolation search
SRGSS	Range Golden Section Search
SSM	Stepwise Search Method
UD	Unidirectional
XFEM	Extended finite element

Symbols

δ_{eq}°	Equivalent displacements at damage initiation
δ_{eq}^{f}	Equivalent displacements at full failure
$\parallel$	Longitudinal
σ	Stress tensor
$\sigma_{\circ}$	Yield point

$\sigma_n, \tau_{nt}, \tau_{n1}$	Fracture plane stresses
$\sigma_\parallel$	Longitudinal normal stressing
$\sigma_\perp$	transverse normal stressing
$\sigma_{i,j}$	Stress vector components (i=1,2,3)
$\tau_\perp$	Transverse shear stressing
$\tau_{\perp\parallel}$	Longitudinal shear stressing
θ	Action plane angle (IFF)
θ_{fp}	Fracture plane orientation
ε	Stain tensor
ε_0^{pl}	Equivalent plastic strain
ε_f^{pl}	Equivalent plastic strain at failure
F_I	Damage initiation parameters $I \in \{f_t, f_c, m_t, m_c\}$
$f_{E,IFF}$	IFF failure exposure
F_{fc}	Fibre compressive damage mode
F_{ft}	Fibre tensile damage mode
F_{mc}	Matrix compressive damage mode
F_{mt}	Matrix tensile damage mode
G_f	Fracture energy
L_c	Characteristic length
$p_{\perp\parallel}^{t,c},\ p_{\perp\perp}^{t,c}$	Inclination parameters

R^A Fracture resistance of the action plane (IFF)

S^L In-plane shear strength

v Poisson's ratio

X^C Fibre compressive strength

X^T Fibre tensile strength

Y^C Matrix compressive strength

Y^T Matrix tensile strength

Contents

List of Figures

List of Tables

Chapter 1

Introduction

1.1 Motivation and background

Since decades aerospace researchers have been actively focusing on developing innovative materials consisting of two or more materials aiming to result in a composite material with improved material characteristics. One of those concepts can be traced back to 1916 when Anthony Fokker incorporated the idea of stacking layers of plywood at certain fibre orientations to meet the required strength for his wing structure of Fokker F.VII-3m [100]. Since then Fokker continued the research and development of laminated materials for his aerospace industry, where he found that fracture toughness of bonded laminates is 25% more than that of monolithic materials [100]. In the following years extensive amount of research has been carried out by Delft University Technology along with its industrial partners: ALCOA, AKZO and 3M on bonding metal sheets with fibre reinforced polymer laminates. They discovered that fatigue crack growth was significantly delayed as the intact fibres restrained crack opening. Upon the discovery of the superior properties of Fibre metal laminates (FMLs), they were recognized as

UD Preperg

Metal Layer
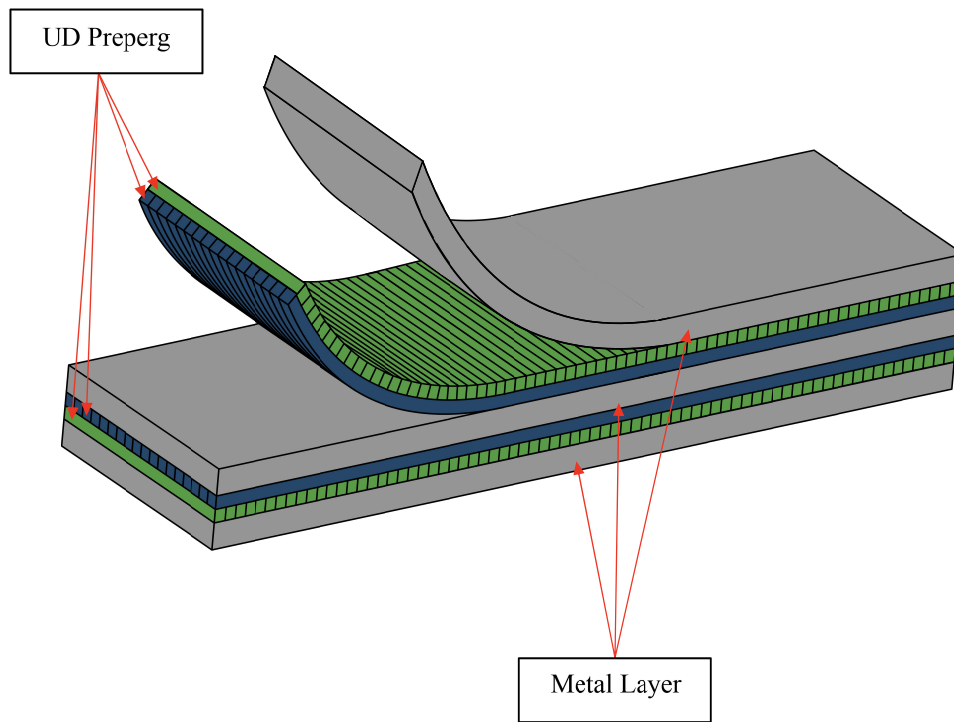
Figure 1.1: A schematic diagram of a typical FML

hybrid composite materials that integrate metal and Fiber-reinforced polymer (FRP) layers and they gained a reputation in the aerospace industry following the registration of the patent in 1981 [99]. A schematic diagram showing the configuration of FMLs is illustrated in Figure 1.1.

The first commercially produced FML was Aramid Reinforced Aluminium Laminates (ARALL), where two panel wings made from ARALL were applied to the aircraft F-27 and tested, the project was successful and results showed 25% weight reduction compared to aluminium [99]. The first commercial application of ARALL was on the C-17 military transporter aircraft, ARALL provided a lightweight yet durable solution [63].

This followed the development of a more advanced FML known as GLARE, which consisted of glass fibre laminates reinforced with aluminium sheets. GLARE has excellent impact and fire resistance properties, therefore, it was implemented

in the cargo floor of Boeing 777. Furthermore, cross-plied variants of GLARE
such as GLARE 3 & 4 incorporate fibres in two directions, with one direction
perpendicular to the other. Those variants were designed for fuselage applications
for example curved GLARE fuselage panels are used for the Airbus A380, in the
cargo floor of the Airbus A330 and the front bulkhead of the Bombardier Learjet
125 [99, 100].

The concept of FMLs can be extended to other types of metals, fibre laminates
and adhesives, thereby creating new materials with improved material character-
istics. For instance, the combination of carbon fibre laminates and aluminium
(CARALL) resulted in a hybrid material with higher stiffness. Indeed magnesium
and titanium are receiving extensive attention from researchers for their potential
use with various fibres including glass fibre [3, 85] and carbon fibre [14, 109].

The mechanical behaviour of FMLs is quite challenging to understand due to
its composition of multiple materials with diverse mechanical behaviours. Metal
sheets tend to exhibit elasto-plastic behaviour, FRPs behave elastically and ad-
hesives are viscoelastic materials. Therefore complex multiple failure modes are
associated with the failure of FMLs, these include fibre breakage/kinking, matrix
cracking, delamination and plastic damage of metal layers. The failure modes
could vary depending on which metal, fibre or matrix is used in the FML. More-
over, it is influenced by the FML grade which includes a unique metal-fibre layup
and fibre orientations in the prepreg. Understanding the failure of FMLs is very
critical for the aerospace industry mainly for ensuring the safety of aircraft com-
ponents. Additionally, it helps design engineers estimate the aircraft's life cycle
and optimise routine maintenance to improve the lifespan of the part.

Aircrafts undergo extensive testing for certification, including the maximum wing
bending at limit load, fuselage pressure test, and fatigue test [9]. However, these

testing campaigns require long running time and costly operations. For example, the A380's fatigue testing lasted 26 months, at which the testing accumulated a total of 47,500 flight cycles [9]. Conversely, numerical simulations are capable of replicating aircraft testing campaigns, assisting design engineers in optimising the development lead-time of the aircraft. Furthermore, numerical simulations provide a powerful and cost-effective tool for investigating the failure mechanisms of aircraft components made from FMLs. The so-called FE-simulation (finite element) is capable of predicting the behaviour and failure modes of FML components, which might be difficult to detect using experimental processes such as C-scan [63]. As FMLs contain different materials, various failure criteria have to be taken into account to accurately assess their failure process.

The investigation of FML's failure modes using FEA requires the development of a comprehensive model capable of distinguishing the different behaviours and failure modes of the materials contained in FMLs. This creates a challenging problem due to the high non-linearity of the model which is related to the damage constitutive model, the failure criteria, the damage evolution law, the interface and the element deletion algorithms.

1.2 Research gap

The increasing demand for hybrid composite materials requires precise models to predict their behaviour under various loading conditions. The complexity of the mechanical behaviour of FMLs lies in the diverse properties of their constituents and the damage mechanisms that occur during the progressive failure process. Therefore, there is a necessity for a comprehensive failure model accounting for 3D stress states and considering diverse material behaviours to enhance the accuracy of predicting the failure process in FMLs. The current state of research on FMLs requires novel contributions to improve the accuracy of predicting the mechanical behaviour and distinguishing between the damage mechanisms in FMLs. The focus lies on developing a computational model consisting of several material constitutive laws, failure criteria and damage evolution models. The approach includes the implementation of a physically verified criterion for identifying the fracture plane within the composite layers in FMLs. Considering the critical importance of achieving accurate results while maintaining an efficient numerical model, it is crucial to develop a numerical technique that effectively attains a solution. Furthermore, a compatible damage evolution law is essential for predicting the material's behaviour post-failure. The developed constitutive model has to be integrated into a user-defined subroutine compatible with an FE commercial software in order to apply it for testing FMLs, enabling its application across diverse mechanical tests of FMLs. The developed framework aims for an innovative and realistic prediction of the damage mechanisms in FMLs.

1.3   Scope and Objectives

The main aim: To develop novel modelling techniques that can accurately predict fibre metal laminates' mechanical response and failure mechanisms.

The Objectives:

- Review of the relevant publications on the damage modelling of FMLs.

- Implementation of physically based failure theories for accurately predicting damage initiation in FMLs.

- Selection/modification of damage evolution law to suit the selected failure criteria.

- Development of a numerical method for improving the computational efficiency of the FE model.

- Implementation of the proposed framework into an explicit FE software.

- Validation of the proposed framework by comparing FE results with experimental data.

- Development of 3D FE damage models of open hole tensile and 3-point bending tests to analyse the mechanical performance and failure mechanisms of FMLs.

- Verification of the FE models through sensitivity studies and validating the results against experimental data.

- Conducting Progressive failure analysis of GLARE specimens in open hole tensile test and CARALL specimens in flexural test, focusing on both on-axis and off-axis orientations.

1.4   Thesis Outline

Chapter-1: Introduces background information about fibre metal laminates and their applications in engineering, and discusses the motivation for this research.

Chapter-2: Presents relevant approaches for modelling the mechanical behaviour and the progressive damage of FMLs constituents. In addition, it provides an overview of analytical models of FMLs and focuses on studies that present numerical models for FMLs.

Chapter-3: The development of the current framework is presented in Chapter 3. It begins with defining the material's behaviour and presents the implementation of the failure criteria for fibre and matrix. Then it discusses the approaches for obtaining the fracture plane and proposes the current algorithm for efficiently obtaining the fracture angle. Additionally, the criteria for defining the metal sheets' behaviour, as well as the interface between the layers, are presented in this chapter.

Chapter-4: This chapter presents the construction of an FE model for a tensile test of CFRP with fibre angles oriented both at 0° and 90°. Experimental results of similar tests are also presented and a comparison is carried out to validate the proposed subroutine.

Chapter-5: This chapter introduces the development of an open-hole tensile test of GLARE, considering on-axis and off-axis fibre angles. It also provides a mesh sensitivity study and validation of the tensile strength of GLARE. A progressive damage analysis is provided, focusing on the damage mechanisms that appeared during the simulation. Finally, a comparative study is conducted to emphasise the effect of fibre angle orientations on FML's behaviour.

Chapter-6: A second case study is presented in this chapter, starting with the development of a 3-point bending test for CARALL with on-axis and off-axis specimens. Then a mesh sensitivity study and validation of the FE model are presented. The progressive damage is discussed in both specimens and the failure mechanisms are illustrated. Finally, the behaviour of the on-axis and off-axis specimens are compared.

Chapter-7: Discusses the conclusions drawn from the method developed in this research and the conclusions drawn from the results obtained from chapters 5 & 6. In addition, suggestions for future improvements and extended applications are provided in this chapter.

1.5   Scientific contributions

Journal Paper:

- N. Wirawan, I. Abuzayed, M. Akbar and J. Curiel-Sosa (2024) A robust fast fracture plane orientation angle search algorithm for Puck 3D inter-fibre failure criterion. European Journal of Computational Mechanics, 33 (3). pp. 227-254. ISSN 2642-2085. `https://doi.org/10.13052/ejcm2642-2085.3332`

Book chapter:

- Abuzayed, I.H., Wirawan, N., Curiel-Sosa, J.L. (2025). A Numerical Study on the Flexural Behavior and Failure Mechanisms of Fiber Metal Laminates. In: Gürgen, S. (eds) Failure in Aircraft Materials. Sustainable Aviation. Springer, Cham. `https://doi.org/10.1007/978-3-031-65850-1_2`

Conference paper:

- I. Abuzayed, N. Wirawan, C. Zhang, and J. Curiel-Sosa. A 3d damage model for simulating damage modes in fibre metal laminates. In 9th EC-COMAS Thematic Conference on the Mechanical Response of Composites. CIMNE, 2023. URL `https://www.scipedia.com/public/Abuzayed_et_al_2023a`

Conference contribution:

- I. Abuzayed, A. Saadi and J. Curiel-Sosa. Computational Modelling of Failure Mechanisms in Fibre Metal Laminates, in: Presentations to VIII Conference on Mechanical Response of Composites. 2021. URL `https://www.scipedia.com/public/Abuzayed_et_al_2021a`

Chapter 2

Literature review and damage modelling of FML constituents

2.1 Introduction

This chapter introduces the mechanical behaviour of fibre composites, with an overview of various approaches for modelling uni-directional composites. Then the approaches for modelling the failure types in fibre composites are addressed. This is followed by an overview of the analytical models used for studying FML's behaviour and numerical techniques used for modelling the damage of FMLs in tensile and flexural tests.

2.2   The mechanical behaviour of fibre composites

Fibre reinforced polymers (FRPs) are a family of composite materials consisting of fibres and matrix. In FRPs, fibres provide stiffness and strength to the composite structure as they are stronger and stiffer than the matrix. The most commonly used fibres are carbon, glass and aramid fibres, each with varying performance characteristics based on their grade. However, fibres alone can not sustain compressive and transverse loads, therefore a matrix material is used to provide support and obtain structural integrity to the structure. The most commonly used matrix is polymer resins such as epoxy, unsaturated polyester and vinyl esters [13].

In FRPs, fibres have two main configurations, known as long and short fibres. Long fibres are continuously aligned in the composite structure, allowing for higher fibre quantity (known as fibre volume fraction). With this type of fibre a fibre volume fraction of 60%-70% is achievable in practice [13]. These fibres are mostly common among high performance engineering applications such as aerospace and automotive, due to their Superior mechanical performance (i.e. strength and stiffness). With these fibres, a composite material is made by creating thin uni-directional plies (laminae), which are then stacked at various orientation angles to form a laminate as illustrated in Figure 2.1-b & c. The composite designer selects the fibre orientation angles, thickness and material to achieve the desired properties for a certain application.

On the other hand, short fibres can be manufactured with forming processes such as extrusion, drawing and rolling. Since the fibres are discontinuous and are randomly distributed in the composite structure. Although the mechanical per-
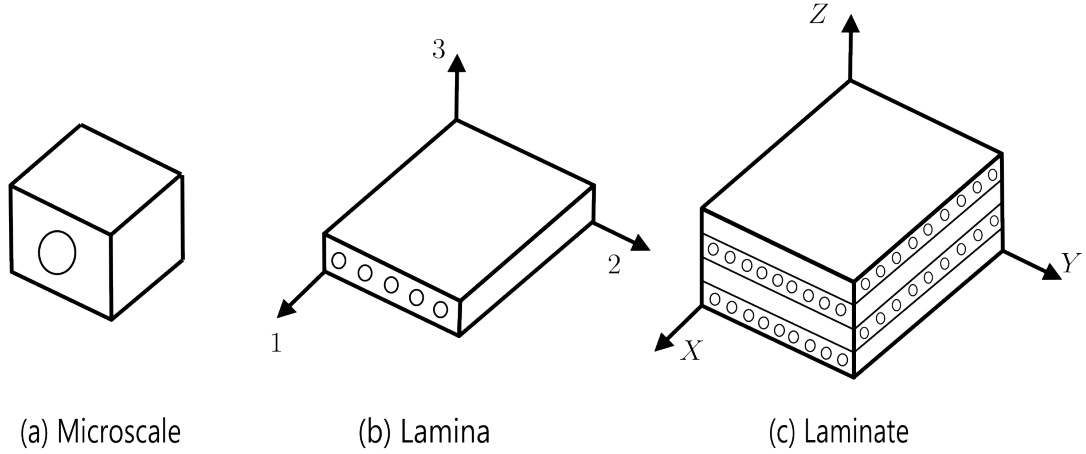
Figure 2.1: Illustration of the different levels of a unidirectional composite: (a) individual fibre, (b) thin unidirectional lamina, and (c) the final laminate formed by stacking the plies at various orientation angles

formance of these materials is lower than UD composites, they are still preferred in some applications such as automotive interiors and marine applications due to their ease of manufacture and lower cost [13,17]. The focus of this thesis is on the uni-directional long fibres as they are the type of composite commonly used with FMLs. The rest of this section will discuss the approaches utilized for predicting the mechanical behaviour of these composites.

2.2.1 Micromechanics of composites

The micromechanics of composites studies the properties of the composite materials by considering the interaction between their constituent materials [6]. This approach assumes the composite structure as an equivalent homogeneous structure, with anisotropic behaviour. Therefore, the composite lamina that contains fibres and matrix is analysed as a block of material. To account for the anisotropy of the material, the basic mechanics of materials approach considering the micromechanics of the material is utilized to predict the stiffness and strength. Anisotropic materials have different properties when measured from different directions, thus, they behave differently according to the direction of the applied load. The behaviour of the material is studied using the 3D Hooke's law, which

refers the stress to the strain in the form:

$$\sigma_{ji} = C_{jilk}\varepsilon_{lk} \tag{2.1}$$

Where (C_{jilk}) is the stiffness tensor which can be written as a 6×6 matrix. The stiffness matrix of anisotropic materials is defined by 21 independent constants [62]. These constants can be reduced to 9 constants if an orthotropic material is assumed, where 3 planes of symmetry are taken into consideration. One plane perpendicular to fibres direction and the two other planes are parallel to the fibres direction. The 3D Hooke's equation reduces to Equation 2.2 for orthotropic materials. Further reduction is possible when assuming a transversely isotropic material, where only one plane of symmetry exists parallel to the fibres. This material is described by 5 independent constants, where the components of the stiffness matrix are dependent on the engineering constants (E, G, ν), which are obtained experimentally for each composite material. More description of these models and details of the derivation of the stiffness matrix components are available in [6, 7, 23].

$$\begin{Bmatrix} \epsilon_1 \\ \epsilon_2 \\ \epsilon_3 \\ \gamma_4 \\ \gamma_5 \\ \gamma_6 \end{Bmatrix} = \begin{bmatrix} S_{11} & S_{12} & S_{13} & 0 & 0 & 0 \\ S_{12} & S_{22} & S_{23} & 0 & 0 & 0 \\ S_{13} & S_{23} & S_{33} & 0 & 0 & 0 \\ 0 & 0 & 0 & S_{44} & 0 & 0 \\ 0 & 0 & 0 & 0 & S_{55} & 0 \\ 0 & 0 & 0 & 0 & 0 & S_{66} \end{bmatrix} \begin{Bmatrix} \sigma_1 \\ \sigma_2 \\ \sigma_3 \\ \sigma_4 \\ \sigma_5 \\ \sigma_6 \end{Bmatrix} \tag{2.2}$$

2.2.2   Homogenisation approach

An alternative approach for predicting the elastic properties of FRPs involves using homogenisation techniques. In these theories, the composite material is assumed to consist of a small microstructure that is repeated throughout the structure, similar to the microstructure shown in Figure 2.1-a [26]. The small microstructure that contains all features of the material is referred to as the representative volume element (RVE), and was initially introduced by [37]. Therefore, the properties of the RVE represent the mechanical behaviour of the overall composite structure. Various homogenisation techniques are available in the literature, including empirical, analytical and numerical techniques. However, the focus will be on the numerical techniques as they are the most commonly used method for FRPs. A comprehensive description of homogenisation techniques used for composite materials, with a focus on numerical implementation and topology optimization, is presented in a three-paper review [31–33].

One of the key elements in these models is the quantification of the RVE characteristics such as the size, fibre volume fraction and shape of the fibres. Thomas et al [93] studied the microstructure of the RVE size in CFRP with high fibre volume fraction. They demonstrated a non-uniform distribution of fibres and epoxy-rich regions within the composite layers, these factors had a huge influence on the considered RVE size. Stroeven et al. [87] quantified the RVE size utilizing a statistical procedure for determining the averages and standard deviations of peak load, dissipated energy and strain concentration factor for RVEs with different fibre volume fractions. Another important element in these models is the consideration of the interface failure between the fibre and matrix. The progressive debonding between fibres and matrix in the RVE is investigated numerically with different interface models such as cohesive-zone model (CZM) [49,97], combination of CZM and extended finite element (XFEM) [67] and a linear elastic–brittle

interface model (LEBIM) [98].

Once the properties are computed from the RVE, these properties are applied to a mesoscale model, such as a test specimen, and in some cases is it applied to a macroscale model such as aerospace structures. The process of using multiple scale models is referred to as multi-scale modelling, which is commonly used for predicting mechanical behaviour and investigating the failures of composites. For instance, Mengze et al. [54] developed a multiscale modelling framework for studying the influence of void volume characteristics on the macroscopic mechanical behaviour and damage mechanisms of CFRP. Another example is the multiscale model developed by Tan et al. [91], for studying the effect of interface properties on the intralaminar and interlaminar failure behaviour of composite laminates. The advantage of this approach over experimentally finding the properties of the composite is that it could be calculated for any fibre volume fraction, given the individual properties of the fibres and matrix. However, in multiscale models, the accuracy of the results relies on the accuracy of each model i.e. microscale or macroscale models. Therefore, an inaccurate result in one model will carry over to the next level, thus propagating the error in the final results.

2.3 Composites damage modelling approaches

2.3.1 Failure criteria of FRPs

The simplest method for predicting the failure of a material is by utilizing the maximum stress (Equation 2.3) or maximum strain (Equation 2.4) criteria. Those criteria were initially developed for isotropic materials, where a failure is assumed to occur if the maximum stress or strain reaches the strength of the material. Some researchers applied these criteria to anisotropic materials, by solving the equation for each applied stress individually. This provided good prediction of the failure of composites in certain cases such as when a tensile load is applied transverse to the direction of the fibres, as the material is more likely to fail as a result of matrix cracking. However, the limitation of this approach is that it does not account for the interaction between different damage modes. For example, in the case of applied compressive load, the failure is expected to occur as a result of both compression and shear stresses. Therefore, researchers developed various criteria that account for the possible interactions of damage modes, the most common failure criteria among these will be considered in the following sections.

$$f = \max \left(\frac{\sigma_{ij}^k}{S_{ij,}^k} \right), \quad \textit{where } i,j = 1,2,3 \textit{ and } k = t,c \tag{2.3}$$

$$f = \max \left(\frac{\varepsilon_{ij}^k}{\varepsilon_{ij,}^k} \right), \quad \textit{where } i,j = 1,2,3 \textit{ and } k = t,c \tag{2.4}$$

Tsai-Hill and Tsai-Wu failure criteria

Tsai-Hill failure criterion is one of the earliest failure criteria developed for composites. Hill [38] started by deriving the Von-Mises criterion for orthotropic materials. Then Tsai [94] modified Hill's criterion by replacing the yield stress terms with strength terms suitable for composite materials, the criterion is expressed using plane stresses as defined in Equation 2.5. Where (σ, τ) are the applied directional stresses and $(S_{i,j})$ are the corresponding directional strength. The criterion assumes the first ply failure (FPF) occurs when the sum of the terms in Equation 2.5 is equal to or greater than 1.0. This criterion is simple to implement and effective for predicting the overall failure of the laminate. Although it provides a prediction of the initial failure in the laminate, it is quite limited as it can not identify the failure modes. Additionally, this criterion might underestimate the failure stress of the material as the tensile transverse strength is much lower than the compressive transverse strength.

$$f = \frac{\sigma_{11}^2}{S_{11}^2} - \left(\frac{\sigma_{11}\sigma_{22}}{S_{22}^2}\right) + \frac{\sigma_{22}^2}{S_{22}^2} + \frac{\tau_{12}^2}{S_{12}^2} \tag{2.5}$$

Tsai-Wu [48, 96] proposed a failure criterion that differentiates between tensile and compressive stresses in its equation. The criterion is expressed for 2D stress in Equation 2.6, where the terms $(F_i, F_{i,j})$ are determined experimentally from the strength of the material at a specific direction, and the subscripts (t, c) indicates tension and compression. The term (F_{12}) is measured from a biaxial test, which is difficult to obtain for each composite material. Several approximations for this term are available in the literature such as $F_{12} = -\frac{1}{2}\sqrt{F_{11}F_{22}}$, proposed by Tsai [95]. Although this criterion is more accurate in predicting the failure

stress of composites than Tsai-Hill's theory, it is still incapable of determining the failure mode in the composite.

$$f = F_1\sigma_{11} + F_2\sigma_{22} + F_{11}\sigma_{11}^2 + F_{22}\sigma_{22}^2 + F_6\sigma_{12}^2 + 2F_{12}\sigma_{11}\sigma_{22}$$

$$\text{Where,} \quad F_1 = \frac{1}{S_{11}^c} - \frac{1}{S_{11}^c}; \quad F_{11} = \frac{1}{S_{11}^c S_{11}^c}$$

$$F_2 = \frac{1}{S_{22}^t} - \frac{1}{S_{22}^c}; \quad F_{22} = \frac{1}{S_{22}^c S_{22}^c} \tag{2.6}$$

$$F_6 = \frac{1}{S_{12}^2}$$

Hashin's failure criteria

Hashin and Rotem [30] presented failure criteria for UD-FRPs, considering a 2D stress state and accounting for the tensile and compressive stresses. These criteria are derived based on logical reasoning rather than micromechanics basics [70]. The criteria consider fibre and matrix failure modes as shown in Equations 2.7 and 2.8. Where it distinguishes between four possible failure modes: fibre tensile/compressive and matrix tensile/compressive. An improvement to this criteria is proposed by Hashine in [29], where 3D stress states were considered in the derivation of the equations. In those criteria, Hahsin incorporated the shear stress parallel to the fibres in the fibre tensile equation. Moreover, he included the terms incorporating failure due to transverse shear in the matrix compressive equation. Although Hashin's criteria are commonly used in FE software, some researchers raised concerns about its reliability, as its predictions do not always align with experimental results. Most of the concern is regarding the predictions of the fibre compressive and matrix tensile/compressive damage modes. Additionally, Hashin's criteria did not predict the increase in shear strength due to applied compressive stress, as observed by experiments [66, 71]. Furthermore,

Hashin's fibre compression criterion underestimates the failure prediction, as it did not account for in-plane shear in the fibre failure equation [71].

Fibre failure

$$F_{fk} = \left(\frac{\hat{\sigma}_{11}}{X^k}\right)^2 = 1, \quad where \; k = t, c \tag{2.7}$$

Matrix failure

$$F_{mk} = \left(\frac{\hat{\sigma}_{22}}{X^k} + \frac{\hat{\tau}_{12}}{S^L}\right)^2 = 1, \quad where \; k = t, c \tag{2.8}$$

Puck's failure criteria

Puck proposed criteria based on the physical foundations of Hashin's theory [74]. Similar to Hashin, Puck based his theory on four failure mechanisms, with an equation derived for each damage mode. In addition, Puck used physical and logical reasoning for incorporating the fracture plane within the damage mechanisms, which increased the acceptability of the criteria. Although the concept of considering the fracture plane was initially proposed by Hashin, he was concerned about the potentially high computational cost [74].

Puck and Schürmann presented the criteria for a 2D stress state in [75, 76], the equations are presented in Appendix A. The equations for fibre failure are derived assuming the damage occurs as a result of applied axial stress σ_1 along the fibre direction. Furthermore, Puck included the effect of the strain caused by σ_2 and σ_3 in the fibre direction, due to Poisson's effect [47]. Puck's 2D matrix failure criterion assumes three failure modes (A, B and C), as illustrated in Figure 2.2. Mode-A is assumed to occur when a transverse tensile stress (σ_{22}) or combination

of (σ_{22}) and shear (τ_{21}) are applied. While modes B and C occur due to compressive transverse stress and shear (τ_{21}). In mode-B a moderate (σ_{22}) results in a crack parallel to the fibre's direction, with a fracture angle of 0. However, mode-C occurs if a large (σ_{22}) is applied, and the fracture plane is inclined by the fracture angle (θ_{fp}).
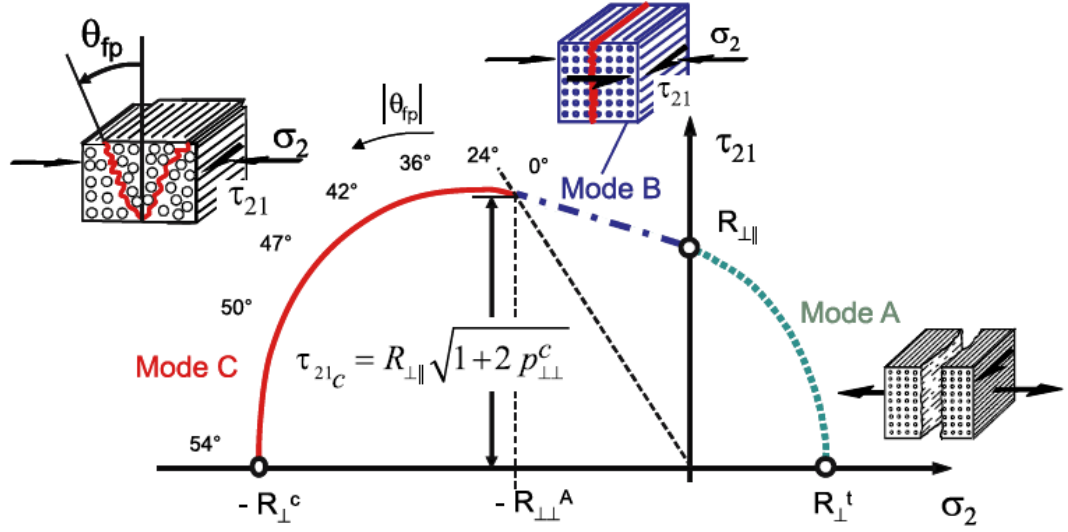
Figure 2.2: Fracture curve of plane stress states [47]

Puck proposed an extended version of his criteria in [19,20,74], which includes 3D stress states. In this criteria, the fracture plane is assumed to occur as a result of applied transverse load and shear and to be parallel to the fibre's direction. There is an infinite number of potential fracture planes between $-90°$ and $90°$. Thus, the fracture angle defining the fracture plane is determined with a numerical search [19]. However, the numerical search could increase the computational time required to find the solution. More details on Puck's 3D failure criteria and alternative solutions for finding the fracture angle will be presented in sections **??** and 3.4.1. It is worth mentioning that Puck's criteria are one of the most accurate theories in the world wide failure exercises [39]. The limitations of the theory include the requirement for specific parameters such as the inclination parameters that are obtained experimentally, in addition to the high computational cost

associated with numerical search for identifying the fracture angle.

2.3.2   Progressive damage modelling

The damage criteria presented in the previous section predict the onset of damage in the lamina or the first ply failure in the case of a laminate. However, these criteria don't predict the behaviour of the material after reaching the failure point. This is important particularly in the case of laminates with multiple orientation angles, as the lamina within the laminate are more likely to fail at different stress levels. Therefore, there is a need for a model that determines the reduction of stiffness caused by cracks and then predict the stress redistribution in the laminate. This section will present the most common methods for progressive damage modelling of Uni-directional composites.

Ply discount method

The ply discount method is the most straightforward method to implement for UD composites. It reduces the selected elastic properties such as (E, G), for a single ply that has reached the onset of failure. Then a new stiffness matrix is calculated using the classical laminate theory (CLT). The loading then continues until the next ply fails, where this cycle is continued until all plies within the laminate are failed [101]. Sun and Tao [89] used a parallel spring model in conjunction with the ply discount method in order to degrade the properties. In this method, the longitudinal modulus (E_1) is reduced to zero when fibre breakage is predicted, while the transverse modulus (E_2) and shear (G_{12}) are reduced to zero when matrix cracks are predicted. The major limitation of this approach is that it cannot model the gradual degradation of the stiffness with increasing crack density in the laminate [72].

Continuum damage mechanics approach

A more acceptable approach in the literature is utilizing the continuum damage mechanics (CDM), which reduces the coefficients of the stiffness matrix according to a damage evolution law. This approach was originally proposed by Kachanov [43] and Rabotnov [77] for isotropic materials. In this method, the stiffness matrix coefficients are degraded based on a damage variable (d) as defined in Equation 2.9, which ranges from 0 for an undamaged state to 1 for a fully damaged state. Several researchers proposed progressive damage models based on CDM for anisotropic materials e.g Matzenmiller [64], Talreja [90], Highsmith and Reifsnider [36] and Allen [2].

$$\hat{C} = (1 - d)C \tag{2.9}$$

The definition of damage variable (d) is defined by the damage evolution law, which characterises the post-damage behaviour of the material. A common approach is to define this variable based on the energy dissipation during the damage process, where a linear behaviour is assumed in some studies such as [27,50], while in others such as [81] a nonlinear behaviour is considered. One of the drawbacks of this approach is the mesh dependency of the numerical solution when using it with FEA. The energy dissipated decreases with mesh refinement when the material exhibits a strain softening behaviour. Bažant and Oh [8] have addressed this issue using a crack band model. This model is used in some studies such as Lapczyk and Hurtado [50] and Maimí et al. [60] for minimizing the mesh dependency in 2D composite models.

2.4   Overview of existing research damage modelling of FMLs

2.4.1   Analytical models for analysing damage in FMLs

This section provides an overview of the literature discussing the analytical constitutive models used to predict the response of FMLs. These models were developed based on the classical laminate theory (CLT), which comprises a set of mathematical equations that predicts the mechanical behaviour of laminated composites by providing the mechanical properties of the fibre and matrix, the fibre orientation and the laminate thickness. In addition, some models contain equations for predicting the plasticity of the metal layers within the FML and failure criteria for predicting the failure of the FML. Most of the literature focused on determining Young's modulus, the ultimate strength, and the strain at failure. However, some researchers went beyond that and developed mathematical models that predict the failure mode and first ply failure (FPF) in FMLs.

The CLT forms the basis of the mathematical formulations that predict the response of FMLs [11, 15, 80, 103]. Equation 2.10 represents the CLT, which describes the behaviour of a laminate, where the forces (N) and moments (M) are related to mid-plane strains (ε°) and curvatures (k) [61]. The terms [A], [B] and [D] are the extension, coupling and bending stiffness matrices respectively, where these matrices are defined by Equation 2.12. Q is the stiffness matrix, h_k and $h_{(k-1)}$ are distances relative to the midplane of the lamina from the reference system used for defining the thickness of each laminate. It is important to note that the coupling matrix [B] is zero for FMLs as they have symmetric laminates. Where a plane of symmetry exists at the midplane of the laminate; therefore, any bending effect will be balanced by the mirrored ply.

$$
\begin{bmatrix} N \\ M \end{bmatrix} = \begin{bmatrix} A & B \\ B & D \end{bmatrix} \begin{bmatrix} \varepsilon^o \\ k \end{bmatrix}
\tag{2.10}
$$

$$
A_{x,y} = \sum_{k=1}^{n} Q_{x,y}^{k} \left(h_k - h_{k-1} \right)
$$
$$
B_{x,y} = \frac{1}{2} \sum_{k=1}^{n} Q_{x,y}^{k} \left(h_k^2 - h_{k-1}^2 \right)
\tag{2.11}
$$
$$
D_{x,y} = \frac{1}{2} \sum_{k=1}^{n} Q_{z,y}^{k} \left(h_k^3 - h_{k-1}^3 \right)
$$

To analyse the overall behaviour of an FML, the behaviour of the metallic layers has to be accounted for in the stiffness matrix. Wu and Yang [10] adjusted the stiffness matrix of composites to incorporate the elastic properties of metals. Equation 2.12 illustrates the extension matrix [A], where n^{Al} and n^c represent the number of layers and h^{Al} and h^c are the thickness of the aluminium and composite layers respectively. Another approach [6] calculated the overall Young's modulus of the FML by the rule of mixtures shown in Equation 2.13.

$$
[A] = n^{Al} \left[Q^{Al} \right] h^{Al} + n^c \left[Q^c \right] h^c
\tag{2.12}
$$

$$
E_{al/fibre} = E_{al} V_{al} + E_c \left(1 - V_{al} \right)
\tag{2.13}
$$

As shown previously, the CLT represents the elastic behaviour of the material; therefore, the elastic behaviour of metals was easily included within the CLT. However, the challenge lies in accounting for the plasticity of metals in the CLT due to its nonlinear behaviour. Various approaches were employed for modelling the plasticity of metals in the FML. One approach involved using the flow theory of von Mises to describe the elastoplastic behaviour of aluminium layers in GLARE, thus, the Q matrix included the elastic behaviour of glass/epoxy and elastoplastic tangent modulus of aluminium [45]. Another approach employed an equivalent material approach, where the modulus and Poisson's ratio after the yield point were substituted with equivalent material properties, as illustrated in Equation 2.14 [41, 80]. The equivalent modulus E_{eq} represents the slope of the line from an origin to a point after the yield point in the stress-strain curve of aluminium. This term is calculated from the stress-strain curve of aluminium, which accounts for the elastic and plastic strain at a certain point. Equation 2.14 will be used to calculate the equivalent Poisson's ratio v_{eq}, and these values were then substituted in the CLT to determine the extensional matrix [A].

$$v_{eq} = \frac{1}{2} \left[1 - \frac{E_{eq}}{E_{al}} \left(1 - 2v_{al} \right) \right] \tag{2.14}$$

Failure criteria are incorporated in some analytical models for determining the strength and failure strain of the FML as well as for predicting the failure modes and the FPF. Researchers typically examined the failure of FMLs in two main approaches. The first approach assumes that the dominant failure mode in a static uniaxial tensile test of FMLs will be in a composite layer rather than in a metal layer. In this approach the maximum strain failure criterion (Equation 2.4) was adopted for predicting the strength of FMLs. Wu et al. [103] used this approach

to predict the strength of GLARE. The fracture of GLARE is expected to occur when the strain in the glass/epoxy layers reaches the ultimate strain. Therefore, the aluminium sheets are excluded from the assessment of GLARE failure as aluminium exhibits higher failure strain. Although this method is capable of predicting the first ply failure, it is quite limited as it cannot predict the gradual failure process and the failure modes in FMLs.

The second approach involves using two failure criteria: one for predicting the failure of the metal layers and another for predicting the failure of the composite layers. For instance, [41, 80] used Tsai-Hill to predict the failure of Glass/epoxy layers and the maximum strain theory to predict the failure of aluminium. In this approach, the final failure of the FML is assumed to occur when either criterion is met first. This approach succeeded in obtaining the first ply failure and the overall strength of the lamina. However, it is not capable of capturing the failure modes.

2.4.2   Numerical models for simulating damage in FMLs

This section provides an overview of the numerical techniques that have been used for modelling the response and failure mechanisms of FMLs in tensile and bending tests. The challenges of modelling the mechanical response of FMLs involve studying plastic deformation, delamination, crack initiation and propagation in the laminates. Therefore, those models should include the behaviour of each FML constituent and a failure criterion that could predict the failure modes. The details of the FE models along with the parameters that influence the results are reviewed and presented in the following paragraphs.

Damage models of FMLs under applied tensile load

The predominant approach for simulating FMLs involves modelling the metal layers as elastic-plastic materials by defining the elastic properties and isotropic hardening plasticity. Additionally, an elastic behaviour is considered for the composite layers with defined orthotropic material properties. However, various failure criteria have been used for predicting the damage of each constituent. Sadeghpour et al. [83] have used von Mises stress and the maximum stress failure criteria for assessing the yield of aluminium layers and the damage in composite layers respectively. A more common approach is utilizing Hashin's failure 2D criterion for predicting the damage initiation of composites [35,56,105,106]. This criterion is more precise than the maximum stress criterion as it distinguishes between four damage mechanisms: fibre tension/compression and matrix tension/compression. The progressive damage of metal layers is commonly modelled with ductile damage model available in ABAQUS (Equation 2.15), Where $\bar{\varepsilon}_D^{pl}$ is the equivalent plastic strain at the onset of damage, $\bar{\varepsilon}_D^{pl}$ is the equivalent plastic strain and η is the stress triaxiality. He et al [27] used this model for predicting the damage initiation and evolution of aluminium layers in CARALL, and Du et al. [22] used the same criterion for titanium. Some researchers expected that the

failure would occur first in the composite layers [50, 56]. As the ultimate failure strain of aluminium is higher than that of composites. Therefore, they did not apply any failure criterion to the metal layers in the FML.

$$w_D = \int \frac{d\bar{\varepsilon}^{pl}}{-\bar{\varepsilon}_D^{pl}\left(\eta, \dot{\bar{\varepsilon}}^{pl}\right)} = 1 \tag{2.15}$$

In the literature, few researchers modelled the failure mechanisms of FMLs by means of FE techniques. Specifically, studies such as [34, 35, 56] investigated the failure morphologies of different FMLs and validated their FE models with experimental results. In those studies, it is commonly observed that on-axis FMLs tend to have fracture path perpendicular to the loading direction. While fracture paths of off-axis FMLs vary depending on the fibre's orientation in the composite layers. For instance, the crack path of an FML with [±45°] is oriented towards the direction of the fibres [56]; also, tilted cracks might form at the edges of the specimen due to shear stress [34]. Nevertheless, the cracks in the metal layers are generally observed to be perpendicular to the loading direction in both on and off-axis FMLs [56].

Failure sequence in FMLs is a complex topic because each constituent in the FML has a unique failure mechanism. Consequently, monitoring the failure sequence during experiments is difficult as it might include fibre pull-out and interfacial damage. The numerical methods would better describe the failure sequence of FMLs as they can capture the details of the fracture. In the literature, the failure sequence is rarely investigated in FMLs. Lin et al. [56] and He et al. [34] investigated the failure sequence of CARALL in an open-hole tensile tensile test. In both studies, the conclusion drawn is that the failure sequence of both on-

axis and off-axis specimens started with the yield of aluminium layers, followed by matrix cracking in the 90° and ±45° layers. Subsequently, the specimens began to deform plastically due to the plasticity of the aluminium layers. The final stage involved delamination between the layers and fibre breakage in the 0° direction. This conclusion agreed well with Alderlisten's [1] observation about the delamination that occurred at the last stage just before the full fracture of an FML specimen. He et al. [34] provided detailed elaboration on the failure sequence of CARALL from their FE models. They observed more fibre tension damage in the 0° layers, but more matrix tension damage in the 90° layers. However, for the off-axis FML fibre tension, matrix tension and compression damage modes were observed in both ±45° layers. Similar failure morphologies were observed in titanium/CFRP FMLs [22].

Damage models of FMLs under applied bending load

The bending behaviour of FMLs received relatively less attention from researchers. The bending behaviour of CARALL and GLARE were investigated experimentally through a 3-point bending test by several researchers [46, 58, 69]. However, there is a limited amount of research conducted to investigate the flexural behaviour of FMLs using numerical models. This section will provide an overview of the studies that investigated the damage of FMLs under the 3-point bending test. These studies are reviewed based on the main aspects of the numerical model and their significant findings.

Hashin's failure criteria are commonly used in the flexural bending models of CARALL such as [55, 104] and GLARE [42, 79]. Another failure criterion, uncommonly used in FE models in general, is Linde criteria [57], which is a strain-based progressive damage model. Hu et al. [40] adopted this criteria for assessing the damage of composites in their 3-point bending model. Additionally, Gao et

al. [25] compared the flexural behaviour of CARALL using Hashin's and Linde's criteria. The only evident use of Puck's criteria in these models is in [55] who used the 2D version of Puck only for the assessment of matrix compressive failure. Regarding the interlaminar failure, cohesive models with zero thickness [25, 40, 104] and surface-based cohesive model [55] are used in these models.

Most researchers studied the flexural behaviour and damage of on-axis FMLs and compared the results with experimental data such as [9, 25, 40]. A common observation from these models is that the fibre breakage happened in the 0° layers while matrix cracking in the 90° layers and delamination occurred prior to the failure of the fibre [42]. Yao et al. [104] compared the flexural behaviour of on-axis and off-axis CARALL. Where they concluded that off-axis FML specimens show lower flexural load, but higher bending deformation.

Chapter 3

Development of a computational damage model for FMLs

3.1 Introduction

The current numerical framework integrates multiple criteria, including failure initiation criteria, interface model and damage evolution laws, aiming to simulate the mechanical behaviour and failure mechanisms occurring in FMLs under various mechanical tests. The current composite damage model was developed based on continuum damage mechanics assuming transversely isotropic material behaviour. Where the onset of damage in fibre and matrix was assessed based on the 3-dimensional failure criteria of Hashin and Puck respectively. The damage propagation was modelled utilizing an equivalent displacement and stress evolution law. Moreover, the current model incorporates the Johnson-cook model for analysing the plasticity in metal layers within FMLs. Additionally, a cohesive surface-based model is included for studying the delamination between the layers. This formulation is implemented on 3D elements to overcome certain limitations

associated with plane stress damage models.

3.2   Elastic behaviour of composites

The initial step in implementing the user defined subroutine involves defining the initial material behaviour. In the current model, a transversely isotropic material behaviour is assumed for the definition of the elastic behaviour of composites. This model, as described in section 2.2.1, has one axis of symmetry so it requires defining five independent constants for the definition of their stiffness matrix (Equation 3.1) [7]. The constants are: $E_{11}, E_{22}, \nu_{12}, \nu_{23}, G_{12}$, while, $E_{33}, \nu_{13}, G_{13}, G_{23}$ are dependent constants and can be calculated using the expressions 3.2 to 3.5.

$$
\begin{bmatrix} \sigma_{11} \\ \sigma_{22} \\ \sigma_{33} \\ \sigma_{12} \\ \sigma_{13} \\ \sigma_{23} \end{bmatrix} = \begin{bmatrix} \frac{1-\nu_{23}\nu_{32}}{E_{22}E_{33}\Delta} & \frac{\nu_{12}-\nu_{32}\nu_{13}}{E_{11}E_{33}\Delta} & \frac{\nu_{13}-\nu_{12}\nu_{23}}{E_{11}E_{22}\Delta} & 0 & 0 & 0 \\ \frac{\nu_{12}-\nu_{32}\nu_{13}}{E_{11}E_{33}\Delta} & \frac{1-\nu_{13}\nu_{31}}{E_{22}E_{33}\Delta} & \frac{\nu_{23}-\nu_{21}\nu_{13}}{E_{11}E_{22}\Delta} & 0 & 0 & 0 \\ \frac{\nu_{13}-\nu_{12}\nu_{23}}{E_{22}E_{33}\Delta} & \frac{\nu_{23}-\nu_{21}\nu_{13}}{E_{11}E_{33}\Delta} & \frac{1-\nu_{12}-\nu_{21}}{E_{11}E_{22}\Delta} & 0 & 0 & 0 \\ 0 & 0 & 0 & G_{12} & 0 & 0 \\ 0 & 0 & 0 & 0 & G_{13} & 0 \\ 0 & 0 & 0 & 0 & 0 & G_{23} \end{bmatrix} \begin{bmatrix} \varepsilon_{11} \\ \varepsilon_{22} \\ \varepsilon_{33} \\ \gamma_{12} \\ \gamma_{13} \\ \gamma_{23} \end{bmatrix}
\tag{3.1}
$$

$$
\text{where } \Delta = \frac{1-\nu_{12}\nu_{21}-\nu_{23}\nu_{32}-\nu_{31}\nu_{13}-2\nu_{21}\nu_{32}\nu_{13}}{E_{11}E_{22}E_{33}}
$$

$$
E_{22} = E_{33} \tag{3.2}
$$

$$
\nu_{12} = \nu_{13} \tag{3.3}
$$

$$
G_{12} = G_{13} \tag{3.4}
$$

$$G_{23} = \frac{E_2}{2(1 + \nu_{23})} \tag{3.5}$$

In the VUMAT subroutine, the stress states are computed at each material point. Initially, the material properties are read from the Abaqus/CAE, then strain values are obtained at each material point. After that, the stiffness matrix components are calculated using their definitions in Equation 3.1, which are then used to solve for the stresses.

3.3   Fibre failure criteria

The damage initiation in fibres is assessed based on Hashin's fibre failure criterion [29], which identifies two primary failure modes for fibres: fibre rupture under tension and fibre buckling under compression (kinking). In addition, the criterion suggests that these modes are most likely to occur transverse to the fibre orientation specifically at the plane (X_2, X_3). Therefore, fibre tensile failure is caused by σ_{11}, σ_{12} and σ_{13}, this is damage mode (F_{ft}) is expressed based on the strength along fibre direction and the in-plane and out-of-plane shear strengths as shown in Equation 3.6. The term α in Equation 3.6 determines the contribution of shear terms to fibre tensile failure, ranging from 0 to 1. In the early Hashin's theory (1973) [30] α was set to zero, however, in the later quadratic version of the theory [29] α was set to 1. Currently, there is insufficient evidence to justify an intermediate value of α between 0 and 1. Therefore, in the current work, a value of 1 is used to account for shear stress. The fibre compressive damage mode (F_{fc}) is expressed based on the applied compressive load on the fibre direction as defined in Equation 3.7.

Fibre tension ($\hat{\sigma}_{11} \geq 0$)

$$F_{ft} = \left(\frac{\hat{\sigma}_{11}}{X^T}\right)^2 + \alpha \left(\frac{\hat{\sigma}_{12}}{S^L}\right)^2 + \alpha \left(\frac{\hat{\sigma}_{13}}{S^L}\right)^2 = 1 \tag{3.6}$$

Fibre compression ($\hat{\sigma}_{11} < 0$)

$$F_{fc} = \left(\frac{\hat{\sigma}_{11}}{X^C}\right)^2 = 1 \tag{3.7}$$

3.4   Matrix failure criteria

Puck's inter fibre fracture (IFF) criterion was adopted in the current model to assess the damage initiation in the matrix. The criterion was developed based on the brittle behaviour of composites, assuming the material exhibits transversely isotropic characteristics [20]. IFF is based on two physical fracture hypotheses [74]: firstly the inter fibre fracture occurring at a fibre parallel plane is influenced by normal and shear stresses specifically applied at that plane. Secondly, in the presence of transverse tensile stress, the fracture is caused either by the normal stress independently or in combination with shear stresses. However, the normal stress will not cause fracture (crack opening) on its own in the presence of applied transverse compressive stress.

In the definition of stresses, Puck used the subscripts ($\perp$) and ($\parallel$) to refer to the direction perpendicular and parallel to the fibre's direction respectively, as this emphasises the transverse isotropic nature of the material [47]. Therefore, the longitudinal and transverse normal stressing and longitudinal and transverse

shear stressing are defined as ($\sigma_\parallel$, $\sigma_\perp$, $\tau_{\perp\parallel}$, $\tau_\perp$) respectively.

IFF is an action plane related criterion, therefore it is important to distinguish between the action plane and the fracture plane. The action plane is the plane where the stress is applied, while the fracture plane is the plane where brittle fracture occurs. Indeed, in certain cases, the fracture might occur at a plane different from where the stress is initially applied, as will be demonstrated later. To establish a relationship between the stresses acting on the action plane and its resistance, Puck introduced the concept of fracture resistance of the action plane R^A [19]. This fracture resistance is defined as the amount of stress required to prevent fracture on a specific action plane.

Figure 3.1 demonstrates the fracture planes that occur when applying one of the basic stressings ($\sigma_\perp$, $\tau_{\perp\parallel}$, $\tau_{\perp\perp}$). According to experimental observations [74], applying a tensile normal stressing $\sigma_\perp^t$ results in a fracture plane perpendicular to the direction of the applied stressing. In this case, the strength of the material $R_\perp^t$ and the fracture resistance of the action plane $R_\perp^{At}$ have identical values, as the fracture plane aligns with the action plane of the applied stressing [19]. Similarly, applying shear stressing $\tau_{\perp\parallel}$, leads to a shear fracture on its action plane, thus $R_{\perp\parallel}^{At}$ is equal to $R_{\perp\parallel}^t$.

In contrast, a specimen subjected to transverse shear stressing $\tau_{\perp\perp}$, fails at an angle of 45° according to experiments [74]. Therefore, the action plane and fracture plane do not coincide, thus ($R_{\perp\perp}^{At} \neq R_{\perp\perp}^t$). According to [19], $R_{\perp\perp}^t$ is unattainable experimentally as the fracture of brittle materials due to applied $\tau_{\perp\perp}$ does not occur at the action plane nor does it result in shear fracture. Moreover, a specimen subjected to transverse compression stressing $\sigma_\perp^c$ results in fracture plane inclined by ±50° [74]. From an experimental point of view $R_{\perp\perp}^t$ could be calculated from a uniaxial transverse compression test, as the applied $\sigma_\perp^c$ leads to $\tau_{\perp\perp}$-shear frac-

ture at $\pm 54°$ [19]. Therefore, Puck introduced Equation 3.8 to calculate $R_{\perp\perp}^{At}$ based on $R_{\perp}^{c}$ and the inclination parameter $p_{\perp\perp}^{c}$. It is worth mentioning that the strength parameters ($R_{\perp}^{t}$, $R_{\perp\parallel}^{t}$, $R_{\perp}^{c}$) are determined experimentally from UD-ply specimens in a composite test.

$$R_{\perp\perp}^{A} = \frac{R_{\perp}^{c}}{2(1 + p_{\perp\perp}^{c})} \tag{3.8}$$
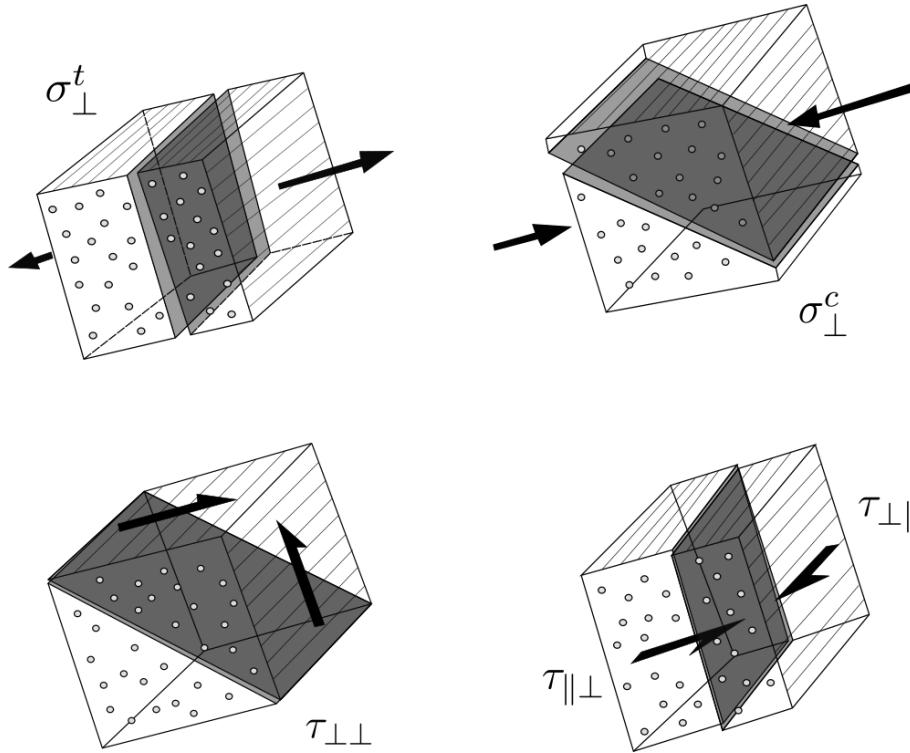
Figure 3.1: Fracture planes of UD composites under uniaxial or shear stress

As described above, IFF is based on three stress components acting on an action plane parallel to the fibres direction. Therefore, Puck proposed a new coordinate system that aligns better with this criterion. This coordinate system involves rotating the conventional coordinate system (X_1, X_2, X_3) by an angle θ, thus yielding the (X_n, X_t, X_1) coordinate system, as demonstrated in Figure 3.2. The

action plane stresses in the IFF $(\sigma_n, \tau_{nt}, \tau_{nl})$ are derived from the stresses applied along the normal directions (X_1, X_2, X_3), as illustrated in Figure 3.2. This is done using the transformation matrix outlined in Equation 3.9. The action plane stresses are described in terms of the action plane angle θ, where there is an infinite number of action planes in the range from -90° to 90°. Once fracture occurs, the action plane orientation θ is then referred to as the fracture plane orientation (θ_{fp}). The determination of (θ_{fp}) requires a numerical search, which will be discussed in the following section.

$$
\begin{bmatrix} \sigma_n(\theta) \\ \tau_{nt}(\theta) \\ \tau_{n1}(\theta) \end{bmatrix} = \begin{bmatrix} \cos^2(\theta) & \sin^2(\theta) & 2\,\cos(\theta)\,\sin(\theta) & 0 & 0 \\ -\cos(\theta)\sin(\theta) & \cos(\theta)\sin(\theta) & \cos^2(\theta)-\sin^2(\theta) & 0 & 0 \\ 0 & 0 & 0 & \sin(\theta) & \cos(\theta) \end{bmatrix} \begin{bmatrix} \sigma_{22} \\ \sigma_{33} \\ \sigma_{23} \\ \sigma_{13} \\ \sigma_{12} \end{bmatrix} \quad (3.9)
$$
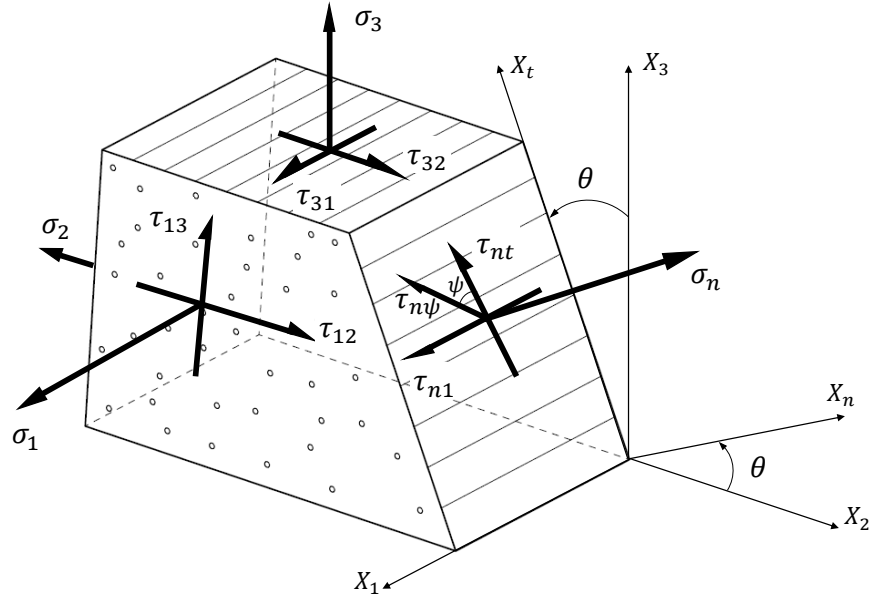
Figure 3.2: Definition of action-plane stresses $(\sigma_n, \tau_{nt}, \tau_{n1})$ on fibre parallel plane

The conditions governing the IFF are visualized through the master fracture body (MFB) in Figure 3.3. The MFB consists of two parts: an elliptical curve representing the tensile σ_n and a parabola representing the compressive σ_n. The known point on the MFB are $(R_\perp^t, \pm R_{\perp\parallel}^t, \pm R_\perp^c)$. The boundaries of the MFB are considered as the damage initiation points, indicating that any stress values within the envelope are considered to be undamaged. At $\sigma_n = 0$ both τ_{nt} and τ_{n1} are causing shear, therefore, they have a common action plane, where an elliptical criterion is assumed to find the $\tau_{n\psi}$ from the applied (τ_{nt}, τ_{n1}), as defined in Figure 3.3 and Equation 3.10. When σ_n, τ_{21} are applied and $\tau_{nt} = 0$, the resultant fracture will be in its own action plane $(\theta_{fp} = 0)$ [19], This is demonstrated as a branch of an ellipse in Figure 3.3, which cuts the σ_n axis at $R_\perp^t$ and $\tau_{n\psi}$ at $R_{\perp\psi}^A$. In the negative σ_n axis, the fracture continues to infinity with parabolic lines, this indicates that a compressive σ_n alone will not cause fracture.

$$\left(\frac{\tau_{n\Psi}}{R_{\perp\Psi}^A}\right)^2 = \left(\frac{\tau_{nt}}{R_{\perp\perp}^A}\right)^2 + \left(\frac{\tau_{n1}}{R_{\perp\parallel}^A}\right)^2 = 1 \quad \text{for } \sigma_n = 0 \qquad (3.10)$$

The following paragraphs outline the mathematical formulation of the IFF. The equations presented are sourced from references [74], [19] and [47]. Equation 3.11 represents the elliptical part of the MFB for $\sigma_n \geq 0$, While Equation 3.12 characterizes the parabolic portion of the MFB for $\sigma_n < 0$.

$$\left(\frac{\tau_{n\Psi}}{R_{\perp\Psi}^A}\right)^2 + c_1 \frac{\sigma_n}{R_\perp^{At}} + c_2 \left(\frac{\sigma_n}{R_\perp^{At}}\right)^2 = 1 \quad \text{for } \sigma_n \geq 0 \qquad (3.11)$$
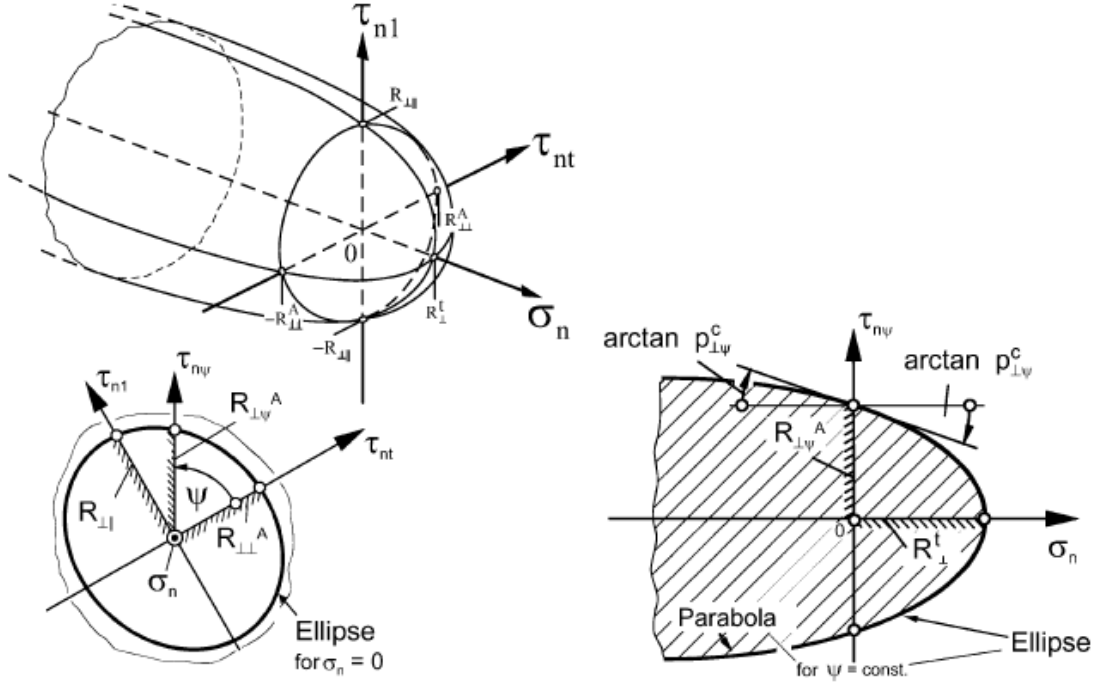
Figure 3.3: The master fracture body (MFB) in $(\sigma_n, \tau_{nt}, \tau_{n1})$-space [47]

$$\left(\frac{\tau_{n\Psi}}{R_{\perp\Psi}^A}\right)^2 + c\sigma_n = 1 \quad \text{for } \sigma_n < 0 \tag{3.12}$$

The ellipse includes 3 known points, which are:

$$(\sigma_n, \tau_{n\psi}) = \left(R_\perp^{At}, 0\right) \quad \text{for } \sigma_n \ axis \tag{3.13}$$

$$and \quad (\sigma_n, \tau_{n\psi}) = \left(0, \pm R_{\perp\psi}^A\right) \quad \text{for } \tau_{n\Psi} \ axis \tag{3.14}$$

Considering the resultant shear stress $\tau_{n\psi} = \sqrt{\tau_{nt}^2 + \tau_{n1}^2}$ at the cross-section where $(\sigma_n = 0)$, along with the geometric relationships $(\tau_{nt} = \tau_{n\Psi}\cos\psi)$ and $(\tau_{n1} = \tau_{n\Psi}\sin\psi)$. By substituting these relations into Equation 3.10 leads to the derivation of Equation 3.15.

$$R_{\perp\Psi}^A = \left[\left(\frac{\cos\Psi}{R_{\perp\perp}^A} \right)^2 + \left(\frac{\sin\Psi}{R_{\perp\|}^A} \right)^2 \right]^{-\frac{1}{2}} \tag{3.15}$$

The ellipse intersects the $\tau_{n\Psi}$-axis with a certain inclination, as shown in Figure 3.3. Although the ellipse and the parabola intersect at $(\sigma_n = 0, \pm R_{\perp\Psi}^A)$, there is a slight variation in the inclination of the parabola. The parameters defining the inclination are defined at the $\sigma_n = 0$ for the ellipse in Equation 3.16 and for the parabola in Equation 3.17.

$$\left(\frac{\delta\tau_{n\Psi}}{\delta\sigma_n} \right)_{\sigma_n=0}^{\text{ellipse}} = \begin{cases} -p_{\perp\Psi}^t & \text{for } \tau_{n\Psi} > 0 \\ p_{\perp\Psi}^t & \text{for } \tau_{n\Psi} < 0 \end{cases} \tag{3.16}$$

$$\left(\frac{\delta\tau_{n\Psi}}{\delta\sigma_n} \right)_{\sigma_n=0}^{\text{parabola}} = \begin{cases} -p_{\perp\Psi}^c & \text{for } \tau_{n\Psi} > 0 \\ p_{\perp\Psi}^c & \text{for } \tau_{n\Psi} < 0 \end{cases} \tag{3.17}$$

Using the conditions in the above equations, the constants (c_1, c_2, c_3) in Equations 3.11 and 3.12 become as shown in the Equations below.

$$c_1 = 2\frac{p_{\perp\Psi}^t R_\perp^{At}}{R_{\perp\Psi}^A}$$

$$c_2 = 1 - 2\frac{p_{\perp\Psi}^t R_\perp^{At}}{R_{\perp\Psi}^A} \tag{3.18}$$

$$c = 2\frac{p_{\perp\Psi}^c}{R_{\perp\Psi}^A}$$

The inclination parameters are defined under two conditions, at $\psi = 0$ and $\psi = 90$, as it is easier to find the values experimentally under these conditions. At $\psi = 0$, where there are values for σ_n and τ_{n1} while $\tau_{nt} = 0$, $p_{\perp\|}^t$ defines the inclination for the ellipse, and $p_{\perp\|}^c$ for the parabola. At $\psi = 90$, where values for σ_n and τ_{nt} exist, $p_{\perp\perp}^t$ defines the inclination for the ellipse, and $p_{\perp\perp}^c$ for the parabola. These inclination parameters are determined experimentally. In the current study, the values listed in Table 3.1 were considered for the GFRP and CFRP as recommended by [19]. For combined shear stresses τ_{nt} and τ_{n1}, the interpolation procedure in Equation 3.19 is utilized.

Table 3.1: Inclination parameters [19]

	$p_{\perp\|}^t$	$p_{\perp\|}^c$	$p_{\perp\perp}^t, p_{\perp\perp}^c$
GFRP	0.30	0.25	0.20 to 0.25
CFRP	0.35	0.30	0.25 to 0.30

$$\frac{p_{\perp\Psi}^{t,c}}{R_{\perp\Psi}^{A}} = \frac{p_{\perp\perp}^{t,c}}{R_{\perp\perp}^{A}} \cos^2 \Psi + \frac{p_{\perp\parallel}^{t,c}}{R_{\perp\parallel}^{A}} \sin^2 \Psi \tag{3.19}$$

$$\text{with,} \quad \cos^2 \Psi = \frac{\tau_{nt}^2}{\tau_{nt}^2 + \tau_{n1}^2}$$

$$\text{with,} \quad \sin^2 \Psi = \frac{\tau_{n1}^2}{\tau_{nt}^2 + \tau_{n1}^2}$$

The second order polynomials outlined in Equations 3.11 and 3.12 define the MFB used for the IFF. Where σ_n and $\tau_{n\psi}$ are the stresses at IFF, with the right side of the equations equal to 1.0 at fracture. Equations 3.11 and 3.12 are rearranged to create a homogeneous function in the first degree of stresses, as expressed in [19]. Therefore, the final formulation of IFF criterion equations are 3.20 for $\sigma_n \geq 0$ and 3.21 for $\sigma_n < 0$.

For $\sigma_n \geq 0$

$$f_{E,IFF+}(\theta) = \sqrt{\left[\left(\frac{1}{R_{\perp}^{At}} - \frac{p_{\perp\psi}^{t}}{R_{\perp\psi}^{A}}\right)\bar{\sigma}_n(\theta)\right]^2 + \left(\frac{\bar{\tau}_{nt}(\theta)}{R_{\perp\perp}^{A}}\right)^2 + \left(\frac{\bar{\tau}_{n1}(\theta)}{R_{\perp\parallel}^{A}}\right)^2}$$

$$+ \frac{p_{\perp\psi}^{t}}{R_{\perp\psi}^{A}}\bar{\sigma}_n(\theta) \tag{3.20}$$

For $\sigma_n < 0$

$$f_{E,IFF-}(\theta) = \sqrt{\left(\frac{p_{\perp\psi}^{c}}{R_{\perp\psi}^{A}}\bar{\sigma}_n(\theta)\right)^2 + \left(\frac{\bar{\tau}_{nt}(\theta)}{R_{\perp\perp}^{A}}\right)^2 + \left(\frac{\bar{\tau}_{n1}(\theta)}{R_{\perp\parallel}^{A}}\right)^2} + \frac{p_{\perp\psi}^{t}}{R_{\perp\psi}^{A}}\bar{\sigma}_n(\theta) \tag{3.21}$$

3.4.1   Fracture angle search algorithm

Although Puck's IFF criterion is considered one of the most reasonable and accurate criteria for the assessment of failure in fibre composites, many researchers are hesitant to use it due to its high consumption of computational power. The IFF Equations 3.20 and 3.21 are formulated in terms of the action-plane orientation θ, which is ranging from $-90°$ to $90°$. Therefore, solving the failure exposure values $f_{E,IFF+}$ and $f_{E,IFF-}$, requires identifying the fracture plane orientation. Puck utilised the Stepwise Search Method (SSM) to compute these values. In this approach, the failure exposure value is calculated for each action-plane angle θ from $-90° \leq \theta < 90°$ with a 1° increment [47]. Then, the results are compared to identify the maximum failure exposure value and its corresponding fracture plane angle θ_{fp}.

To clearly visualize the inclination angles (θ) and their corresponding solution of the failure exposure values (IFF), a plot of (θ vs IFF) is created for a composite material (AS4/PEEK) whose properties and stress states are given in Table 3.2. The plot of (θ vs IFF) using the SSM is illustrated in Figure 3.4, where the red points represent IFF values for $\sigma_n \geq 0$, while the blue points indicate IFF values for $\sigma_n < 0$. Applying the SSM procedure to the current example yields 180 solution points within the range of $-90° \leq \theta < 90°$ for each material point, as illustrated in Figure 3.4. Where the maximum point, marked with a green asterisk (*), is the fracture angle θ_{fp}. Although this method is easy to implement within a subroutine, it presents certain limitations such as consuming a significant amount of computational power and potential accuracy issues due to neglecting the decimal values of the angle θ.

The literature showed several attempts to determine the fracture angle with nu-

Table 3.2: Material properties and stress state applied on AS4/PEEK [59, 82, 88]

Strength (MPa)			Stress states (MPa)				
$R_\perp^t$	$R_{\perp\parallel}$	$R_\perp^c$	σ_{22}	σ_{33}	σ_{12}	σ_{23}	σ_{13}
92.7	82.6	176	43	-18	-8	-52	-8

merical methods; some of these models are presented in the following paragraphs. The EGSS (Extended Golden Section Search) algorithm, developed by Weigand et al. [102], combines the Golden Section Search (GSS) algorithm with the Inverse Parabolic Interpolation method [73]. The algorithm starts with a numerical search for the function's maximum using the GSS, which is done by searching for the maximum value in the range of $\theta_1 = -90°$ to $\theta_2 = 90°$. Then finding two values within the boundary (θ_2 and θ_3) according to the golden ratio. Finally comparing the $f_{E,IFF}$ of the mid θs and eliminating the values to the left or right of the theta with the lower $f_{E,IFF}$ value.

Weigand et al. [102] found that the GSS is accurate in finding the maximum but it requires a large number of iterations for finding the accurate value of the fracture angle (θ_{fp}). Therefore, they proposed the Extended Golden Section Search (EGGS) algorithm, at which they applied the parabolic interpolation in Equation 3.22, to find the (θ_{fp}) which is assumed to be a maximum of a parabola bracketed by upper and lower bounds of the last Golden Section Search (θ_1 and θ_2), as indicated by Equation 3.22.

$$\theta_{fp} = \theta_2 - \frac{1}{2}\frac{(\theta_2-\theta_1)^2\left(f_{E,IFF(2)}-f_{E,IFF(3)}\right)-(\theta_2-\theta_3)^2\left(f_{E,IFF(2)}-f_{E,IFF(1)}\right)}{(\theta_2-\theta_1)\left(f_{E,IFF(2)}-f_{E,IFF(3)}\right)-(\theta_2-\theta_3)\left(f_{E,IFF(2)}-f_{E,IFF(1)}\right)}$$

$$(3.22)$$
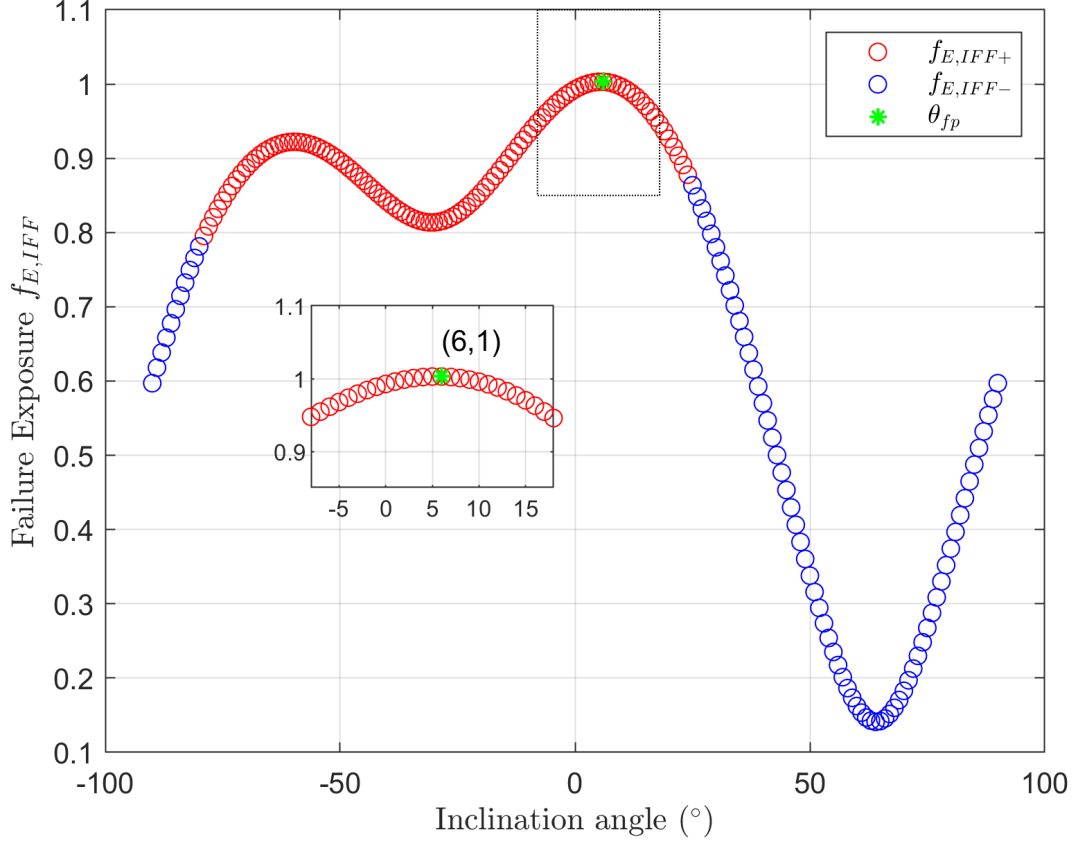
Figure 3.4: Failure exposure vs. inclination angle using the Stepwise Search Method (SSM)

Schirmaier et al. [84] discovered that the EGGS is inaccurate in fining the θ_{fp} in curves with multiple peaks. The GSS actually excludes the global maximum value when it is located near the initial boundaries $\pm 90°$. Schirmaier et al. conducted a comparative study between EGGS and SSM considering 10^5 stress states and found that the fracture angle is $5°$ more in 20% of the stress states.

Schirmaier et al. [84] proposed a new approach for determining the fracture angle θ_{fp}, called the Range Golden Section Search algorithm (SRGSS). Unlike the EGSS, SRGSS does not require the implementation of an interpolation procedure. Instead, it calculates 18 supporting points at intervals of $10°$, then locates the maximum values along with their two smaller neighbours. Subsequently, the method applies the GSS within each selected range to search for the local maximum value. Finally, it compares the local maximum values to determine

the global maximum which corresponds to the fracture angle θ_{fp}. Although this method does not require parabolic interpolation, it requires multiple iterations to achieve an accurate value of the fracture angle, making it computationally inefficient.

Rezasefat et al. [82] presented a new algorithm that does not require an iterative procedure, named Simple parabolic interpolation search (SPIS). Similar to the SRGSS, the algorithm starts with determining 19 supporting points and isolating the ranges containing maximum. Then finding the global maximum by comparing the middle point of the ranges in the previous step. Finally, applying parabolic interpolation within the range including the global maximum for achieving an accurate value for the fracture angle. And then comparing the global maximum with failure exposure at the boundaries ($\pm 90°$).

In the current subroutine, a more efficient approach has been utilized. Through this approach, the improvement in computational power is demonstrated by solving the example of (AS4/PEEK), which was introduced at the beginning of this section. Where the new curve of (θ vs $f_{E,IFF}$) has been illustrated in Figure 3.6. The first step in the current approach involves solving the failure exposure factors Equations 3.20 and 3.21 19 times in order to construct the (θ vs $f_{E,IFF}$) curve. Here a 10° interval is used, as investigations conducted by Schirmaier et al. [84] suggest that the minimum distance containing two maxima is 25°; therefore a 20° range should include only one maximum. These points are illustrated as blue and red circles in the (θ vs $f_{E,IFF}$) curve in Figure 3.6. The next step is to locate the peaks by comparing the IFF values of each 3 supporting points (a maximum and two neighbouring points), and then saving the 3 points that shape a peak.

The next step involves employing Brent's method to find the exact maximum point. Brent's method, as outlined in [73], is a numerical method that combines
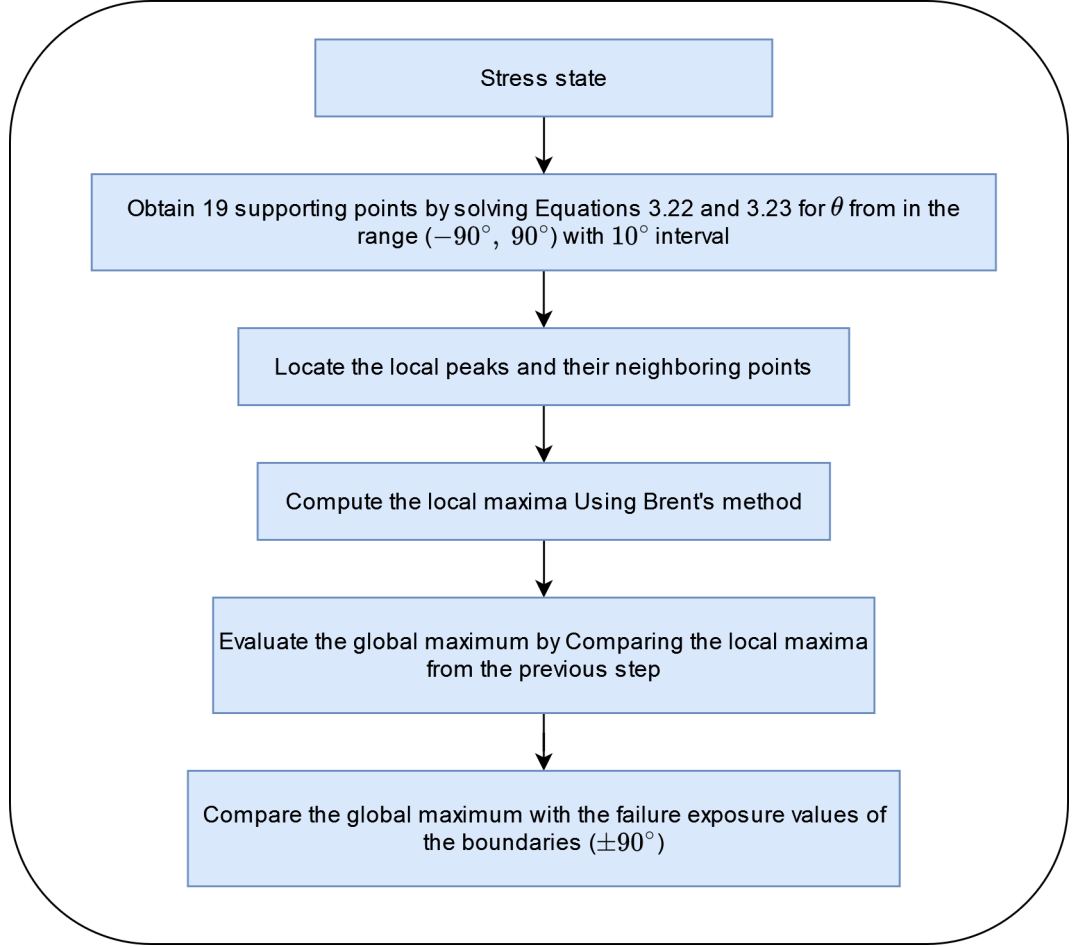
Figure 3.5: Steps for implementing the fast search algorithm

the GSS and the parabolic interpolation. In the current context, Brent's method is adopted to identify the global maximum in the (θ vs $f_{E,IFF}$) curve. Brent's method starts by applying the parabolic interpolation (Equation 3.22) to find the maximum between two points. However, it switches to the GSS when Equation 3.22 diverges i.e. (denominator = 0). This step saves the maxima of all peaks within the curve. Then the global maximum value is evaluated by comparing these values, this is identified by a green asterisk in Figure 3.6. The final step involves comparing the maximum value with the $f_{E,IFF}$ of the boundaries as they might include a higher value. The flow chart illustrated in Figure 3.5 summarises the steps used in the subroutine for finding the fracture angle.
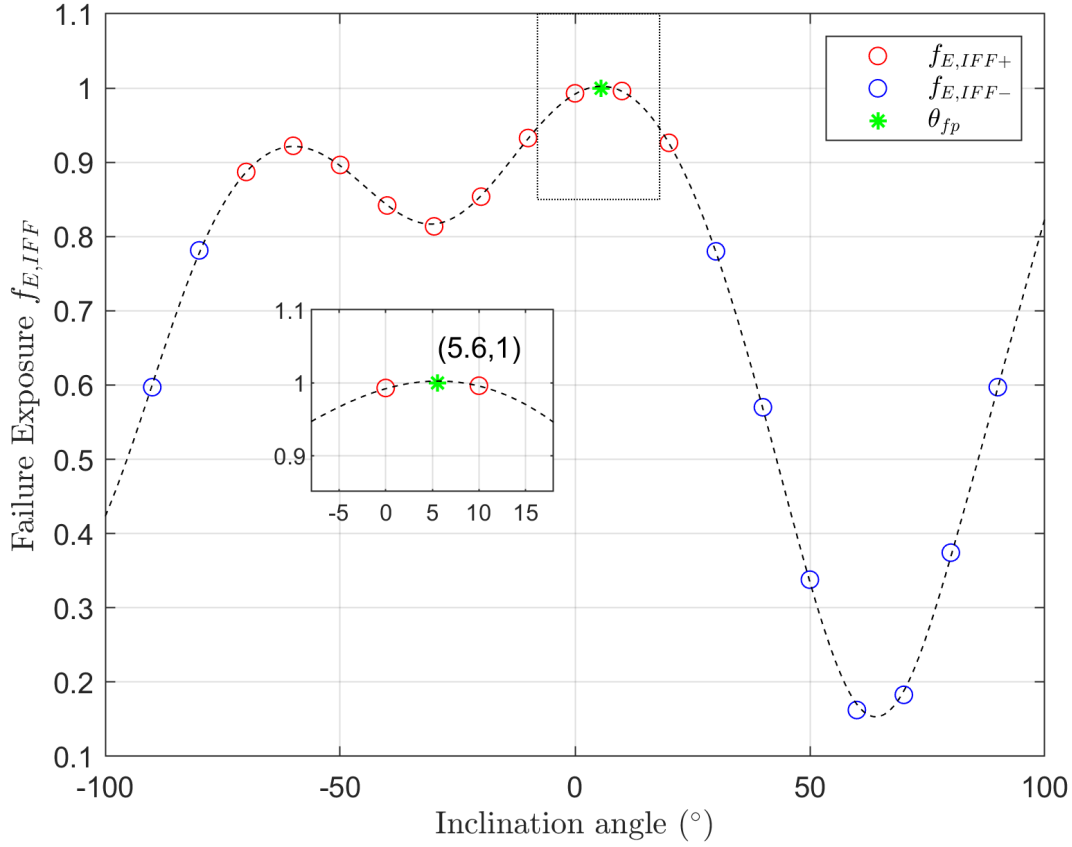
Figure 3.6: Failure exposure vs. inclination angle using the current approach

3.5   Damage evolution model

Once the damage is initiated at a material point, the stiffness matrix coefficients are degraded according to the damage evolution law. In the present subroutine, the evolution law is based on the energy dissipated during damage, which is governed by the equivalent displacements and stresses. This formulation was originally proposed by I. Lapczyk and J. Hurtado [50] for 2D fibre composites and implemented in an implicit solver. In this study, Lapcyk's evolution law was extended to account for 3D stresses in order to ensure compatibility with the initiation criteria presented in the previous sections.

The concept involves implementing a degradation model that maintains the orthographic nature of the material, thus aligning with the assumption of treating the material as a homogenized continuum within a 3D space. The basic idea of

the current model is to degrade the stiffness matrix coefficients based on defined damage variables that are compatible with the material's characteristics, as proposed by Matzenmiller et al. [64]. This approach relates the effective stresses to nominal stresses using the form $\hat{\sigma} = M\sigma$, where M is the damage operator, which has the form:

$$
M = \begin{bmatrix}
\frac{1}{1-d_f} & 0 & 0 & 0 & 0 & 0 \\
0 & \frac{1}{1-d_{m2}} & 0 & 0 & 0 & 0 \\
0 & 0 & \frac{1}{1-d_{m3}} & 0 & 0 & 0 \\
0 & 0 & 0 & \frac{1}{1-d_{s1}} & 0 & 0 \\
0 & 0 & 0 & 0 & \frac{1}{1-d_{s2}} & 0 \\
0 & 0 & 0 & 0 & 0 & \frac{1}{1-d_{s3}}
\end{bmatrix} \tag{3.23}
$$

With the equation above, each component in the stiffness matrix is degraded with a unique damage variable. The fibre damage variable d_f degrades the material in the fibre direction only, therefore it is applied to component C_{11} of the stiffness matrix. Similarly, the material is degraded with the matrix damage variables d_{m2} and d_{m3} at directions 2 and 3 respectively, which corresponds to fibre parallel directions as defined in Equation 3.24. The damage variables have different values for tension and compression denoted as subscripts t, c respectively. However, the maximum between the tension and compression is considered in stiffness degradation. Shear stress damage variables are related to the main variables as recommended by [50] and [12]. The damage operator is applied to the compliance matrix as illustrated in Equation 3.24. While the corresponding stiffness matrix components are listed in 3.25.

$$[S_{ij}] = \begin{bmatrix} \frac{1}{(1-d_f)E_{11}} & -\frac{\nu_{12}}{E_{11}} & -\frac{\nu_{13}}{E_{11}} & 0 & 0 & 0 \\ -\frac{\nu_{21}}{E_{22}} & \frac{1}{(1-d_{m2})E_{22}} & -\frac{\nu_{23}}{E_{22}} & 0 & 0 & 0 \\ -\frac{\nu{31}}{E_{33}} & -\frac{\nu_{32}}{E_{33}} & \frac{1}{(1-d_{m3})E_{33}} & 0 & 0 & 0 \\ 0 & 0 & 0 & \frac{1}{(1-d_{s1})G_{12}} & 0 & 0 \\ 0 & 0 & 0 & 0 & \frac{1}{(1-d_{s2})G_{13}} & 0 \\ 0 & 0 & 0 & 0 & 0 & \frac{1}{(1-d_{s3})G_{23}} \end{bmatrix}$$

$$(3.24)$$

Where, $d_{s1} = 1 - (1 - d_{ft})(1 - d_{fc})(1 - d_{mt2})(1 - d_{mc2})$;

$d_{s2} = 1 - (1 - d_{ft})(1 - d_{fc})(1 - d_{mt3})(1 - d_{mc3})$

$d_{s3} = 1 - (1 - d_{mt2})(1 - d_{mc2})(1 - d_{mt3})(1 - d_{mc3})$

$d_f = \max\{d_{ft}, d_{fc}\}$; $d_{m2} = \max\{d_{mt2}, d_{mc2}\}$; $d_{m3} = \max\{d_{mt3}, d_{mc3}\}$

Resultant stiffness matrix component:

$$C_{11} = E_{11}(1 - d_f)\left[1 - (1 - d_{m2})(1 - d_{m3})\nu_{23}^2\right]/A$$

$$C_{12} = E_{22}(1 - d_f)(1 - d_{m2})\left[(1 - d_{m3})\nu_{13}\nu_{23} + \nu_{12}\right]/A$$

$$C_{22} = E_{22}(1 - d_{m2})\left[1 - (1 - d_f)(1 - d_{m3})\nu_{13}\nu_{13}\right]/A$$

$$C_{13} = E_{33}(1 - d_f)(1 - d_{m3})\left[(1 - d_{m2})\nu_{12}\nu_{23} + \nu_{13}\right]/A$$

$$C_{33} = E_{33}(1 - d_{m3})\left[1 - (1 - d_f)(1 - d_{m2})\nu_{12}\nu_{21}\right]/A \qquad (3.25)$$

$$C_{23} = E_{33}(1 - d_{m2})(1 - d_{m3})\left[(1 - d_f)\nu_{12}\nu_{31} + \nu_{23}\right]/A$$

$$C_{44} = G_{12}(1 - d_f)(1 - d_{m2})$$

$$C_{55} = G_{13}(1 - d_f)(1 - d_{m3})$$

$$C_{66} = G_{23}(1 - d_{m2})(1 - d_{m3})$$

With,

$$A = 1 - (1 - d_f)(1 - d_{m2})\nu_{12}\nu_{21} - (1 - d_{m2})(1 - d_{m3})\nu_{23}^2 - (1 - d_f)(1 - d_{m3})\nu_{13}\nu_{31}$$
$$- 2(1 - d_f)(1 - d_{m2})(1 - d_{m3})\nu_{12}\nu_{31}\nu_{23}$$

It is assumed that the constitutive law is linear between the stress and strain both in the initial material response and during damage degradation. The calculation of damage variables is dependent on the energy dissipated during the damage process (G_c), the area under the stress-strain curve. The damage variables have a value between 0 and 1, where 0 is an undamaged state, while 1 is fully damaged.

The calculation of the damage variables for each damage mode is based on the equivalent displacement as defined in Equation 3.26, where $\delta_{I,eq}^0$ and $\delta_{I,eq}^f$ are the equivalent displacements at damage initiation and at full failure respectively. In equation 3.26, the final equivalent displacement is unknown, which is calculated using Equation 3.28, assuming a given fracture energy and a linear softening behaviour as shown in Figure 3.7. The initial equivalent displacement and stress in Equations 3.26 and 3.28 are solved using Equations 3.27 and 3.29, which are dependent on damage initiation variables (F_I) for each failure mode (f_t, f_c, m_t, m_c). While $\delta_{I,eq}$ and $\sigma_{I,eq}$ indicate the current equivalent displacement and stress, which were calculated using the equations listed in Table 3.3, where (L_c) is the characteristic length, as suggested by [50] and [12]. It is worth mentioning that the damage variable values taken into account in the stiffness matrix are equal to the maximum between the current and the previous value computed by Equation 3.26, since the damage evolution is an irreversible process [50].

$$d_I = \frac{\delta_{I,eq}^f(\delta_{I,eq} - \delta_{I,eq}^0)}{\delta_{I,eq}(\delta_{I,eq}^f - \delta_{I,eq}^0)}; \qquad I \in \{f_t, f_c, m_t, m_c\} \tag{3.26}$$
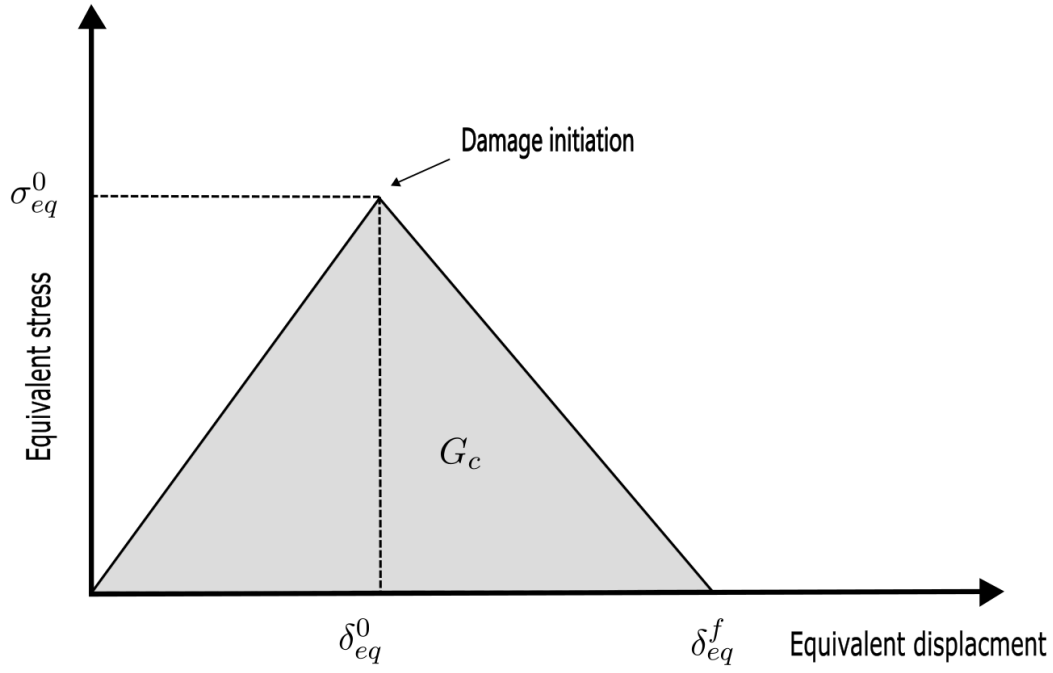
Figure 3.7: Linear softening in Equivalent stress vs displacement plot

$$\delta^0_{I,eq} = \frac{\delta_{I,eq}}{\sqrt{F_I}} \tag{3.27}$$

$$\delta^f_{I,eq} = \frac{2G_{I,c}}{\sigma_{I,eq}} \tag{3.28}$$

$$\sigma^0_{I,eq} = \frac{\sigma_{I,eq}}{\sqrt{F_I}} \tag{3.29}$$

Table 3.3: Equivalent displacements and stresses

Damage mode	$\delta_{I,eq}$	$\sigma_{I,eq}$
Fibre traction ($\sigma_{11} \geq 0$)	$L_c\sqrt{\langle\varepsilon_{11}\rangle^2 + \varepsilon_{12}^2 + \varepsilon_{13}^2}$	$\frac{L_c(\langle\sigma_{11}\rangle\langle\varepsilon_{11}\rangle+\sigma_{12}\varepsilon_{12}+\sigma_{13}\varepsilon_{13})}{\delta_{eq,ft}}$
Fibre compression ($\sigma_{11} < 0$)	$L_c\langle-\varepsilon_{11}\rangle$	$\frac{L_c(\langle-\sigma_{11}\rangle\langle-\varepsilon_{11}\rangle)}{\delta_{eq,fc}}$
Matrix traction ($\sigma_{22} \geq 0$)	$L_c\sqrt{\langle\varepsilon_{22}\rangle^2 + \varepsilon_{12}^2 + \varepsilon_{23}^2}$	$\frac{L_c(\langle\sigma_{22}\rangle\langle\varepsilon_{22}\rangle+\sigma_{12}\varepsilon_{12}+\sigma_{23}\varepsilon_{23})}{\delta_{eq,mt2}}$
Matrix compression ($\sigma_{22} < 0$)	$L_c\sqrt{\langle-\varepsilon_{22}\rangle^2 + \varepsilon_{12}^2 + \varepsilon_{23}^2}$	$\frac{L_c(\langle-\sigma_{22}\rangle\langle-\varepsilon_{22}\rangle+\sigma_{12}\varepsilon_{12}+\sigma_{23}\varepsilon_{23})}{\delta_{eq,mc2}}$
Matrix traction ($\sigma_{33} \geq 0$)	$L_c\sqrt{\langle\varepsilon_{33}\rangle^2 + \varepsilon_{13}^2 + \varepsilon_{23}^2}$	$\frac{L_c(\langle\sigma_{33}\rangle\langle\varepsilon_{33}\rangle+\sigma_{13}\varepsilon_{13}+\sigma_{23}\varepsilon_{23})}{\delta_{eq,mt3}}$
Matrix compression ($\sigma_{33} < 0$)	$L_c\sqrt{\langle-\varepsilon_{33}\rangle^2 + \varepsilon_{13}^2 + \varepsilon_{23}^2}$	$\frac{L_c(\langle-\sigma_{33}\rangle\langle-\varepsilon_{33}\rangle+\sigma_{13}\varepsilon_{13}+\sigma_{23}\varepsilon_{23})}{\delta_{eq,mc3}}$

3.5.1   Element deletion

The final step of the current subroutine involves deleting the fully damaged elements in order to simulate the crack propagation phenomena. The element deletion criterion used in this model is based on the damage threshold and the change of volume in a certain element. This was accomplished by computing the determinant of the deformation gradient ($det(F)$). The deformation gradient (F) is defined as the derivative of the position vector (x) in the current configuration with respect to the position vector (X) in reference configuration, as defined in Equation 3.30 [68]. The determinant of the deformation gradient ($det(F)$) is then the ratio of the deformed volume to the undeformed volume ($\frac{V}{V_0}$) [92].

$$F = \frac{\partial x}{\partial X} \tag{3.30}$$

According to the definition of ($det(F)$), a value of $det(F) < 1$ indicates compression, while $det(F) > 1$ denotes tension. The ($det(F)$) limits depend on the model characteristics, values ranging from 0.6 to 1.6 were suggested by [92], with a value of 1.2 for tension and 0.8 for compression being appropriate for the current

models. An element is deleted if one of the conditions in 3.31 is satisfied. It is worth mentioning that the current criteria for element deletion are not expected to affect the simulation results, as elements are only deleted after reaching the defined damage threshold. However, the limits of $det(F)$ were appropriate in the current simulation for static mechanical tests and they might not apply to other loading conditions i.e. dynamic loads.

$$
\begin{cases}
d_{ft} \geq 0.99 \ and \ det(F) \geq 1.2 \\
d_{fc} \geq 0.99 \ and \ 0.8 < det(F) > 0.8 \\
d_{mt} \geq 0.99 \ and \ det(F) \geq 1.2 \\
d_{mc} \geq 0.99 \ and \ 0.8 < det(F) > 0.8
\end{cases}
\tag{3.31}
$$

A comprehensive VUMAT user-defined subroutine is developed in Fortran and linked with Abaqus/Explicit to implement the theories discussed in this chapter. A flowchart summarising the entire subroutine is illustrated in 3.8. The subroutine begins with reading the material properties and updating the strain from Abaqus CAE, then the stresses are calculated from the material model presented in section 3.2. The stresses are then used to solve Hashin and Puck failure criteria. Where the search algorithm is used in conjunction with Puck's criterion as shown in 3.8. If the failure criteria are satisfied, the damage evolution law is calculated and the distorted elements are deleted.
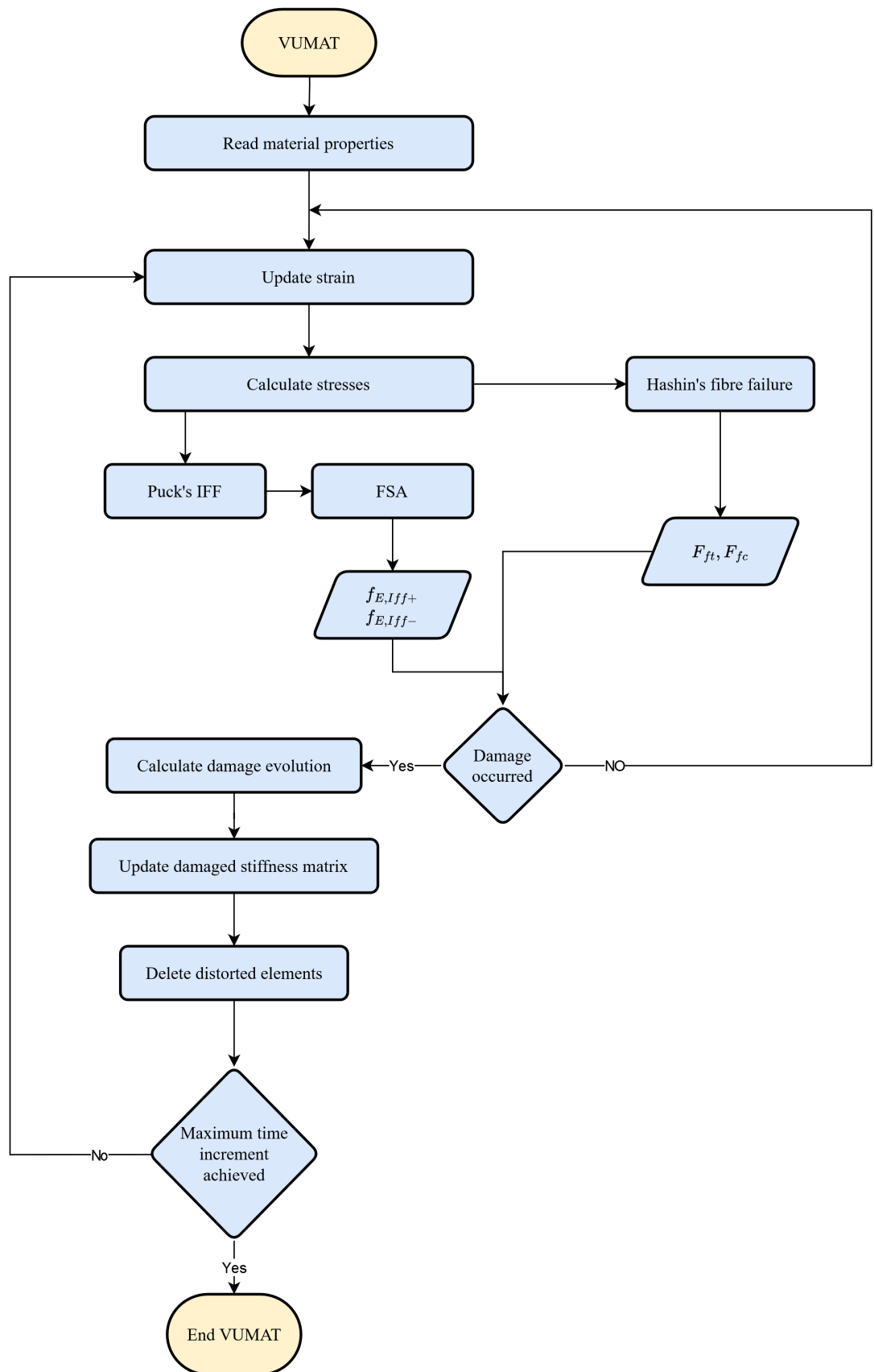
Figure 3.8: Subroutine flowchart

3.6   Metal sheets failure criterion

This section presents the material models utilized to define the mechanical be-
haviour of the metal layers integrated within FMLs. The overall behaviour of
metals is illustrated in Figure 3.9, which demonstrates an elastic-plastic response
with isotropic hardening. Initially, the material behaves linearly until reaching
the yield point (σ_0), in this stage the material is defined by its Young's modu-
lus (E) and poisons ratio (ν). Following the yield point, the materials exhibit a
non-linearly response until reaching the ultimate tensile strength denoted by the
ultimate stress (σ_{y0}) and equivalent plastic strain $(\bar{\varepsilon}_0^{pl})$. This point is used for
defining the onset of damage or the damage initiation point, marked as (point-D)
in Figure 3.9. If a failure criterion is not specified the behaviour will continue
following the dashed curve in Figure 3.9. However, if a failure criterion is met
the degradation of stiffness starts until reaching the full failure at $\bar{\varepsilon}_f^{pl}$.
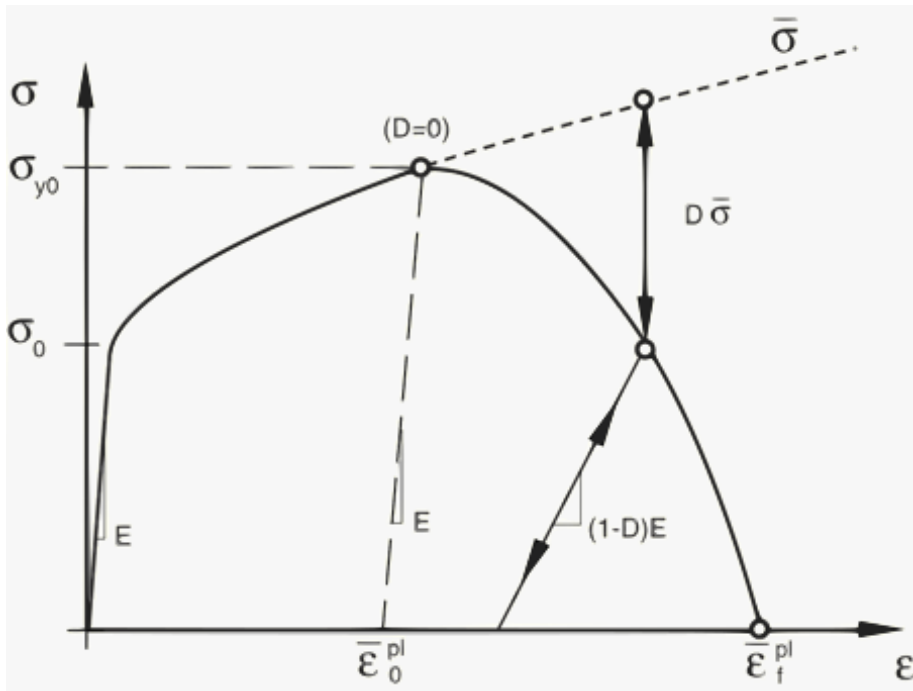
Figure 3.9: A typical stress-strain curve for elastic-plastic material [86]

The onset of damage in the aluminium layers integrated within the FMLs is
assessed utilizing the Johnson-cook damage model available in Abaqus/explicit

[86]. In this model, the damage initiation is assessed based on the equivalent plastic strain increment at the onset of damage $\Delta\bar{\varepsilon}^{pl}$ and the equivalent plastic strain at failure $\bar{\varepsilon}_f^{pl}$, as defined in equation 3.32. Where the failure is assumed to occur when the damage variable ω exceeds 1. $\bar{\varepsilon}_f^{pl}$ is defined by Johnson-Cook failure model (Equation 3.33), where d_1 to d_5 are failure parameters, d_5 is assumed to be 0 as the temperature dependence is ignored in the current simulation. The ratio $\left(\frac{p}{q}\right)$ in Equation 3.33 is the stress triaxiality which is a material property. And the $\left(\frac{\dot{\bar{\varepsilon}}^{pl}}{\dot{\varepsilon}_0}\right)$ is the non-dimensional plastic strain rate. The strain rate for quasi-static tests has typical values between 10^{-1} and 10^{-3} (s^{-1}) [10, 52, 107]. In the current study, the strain rate effect was neglected, and a constant reference strain rate of $10^{-2}s^{-1}$ was applied for the aluminium layers.

$$\omega = \sum \left(\frac{\Delta\bar{\varepsilon}^{pl}}{\bar{\varepsilon}_f^{pl}} \right) \tag{3.32}$$

$$\bar{\varepsilon}_f^{pl} = \left[d_1 + d_2 \exp\left(d_3 \frac{p}{q} \right) \right] \left[1 + d_4 \ln\left(\frac{\dot{\bar{\varepsilon}}^{pl}}{\dot{\varepsilon}_0} \right) \right] \left(1 + d_5 \hat{\theta} \right) \tag{3.33}$$

Once the damage accumulates at a material point and reaches the onset of damage, the element stiffness degrades based on a linear damage evolution law. The damage variable $(\dot{d})$ increases according to Equation 3.34, where the equivalent plastic displacement at failure is defined by the fracture energy (G_f) dissipated during the damage process [86].

$$\dot{d} = \frac{L\dot{\varepsilon}^{pl}}{\bar{u}_f^{pl}} = \frac{\dot{u}^{pl}}{\bar{u}_f^{pl}} \tag{3.34}$$
$$where, \ \bar{u}_f^{pl} = \frac{2G_f}{\sigma_{y0}}$$

3.7   Interface failure criterion

The interface between metal sheets and composite laminates demonstrates resin-rich areas, as illustrated in the scanning electron microscope image in Figure 3.10. Indeed several researchers documented the occurrence of delamination at such interfaces [16, 44]. Therefore, in the current simulation, a cohesive model is implemented to simulate the mechanical behaviour and damage at the interface.
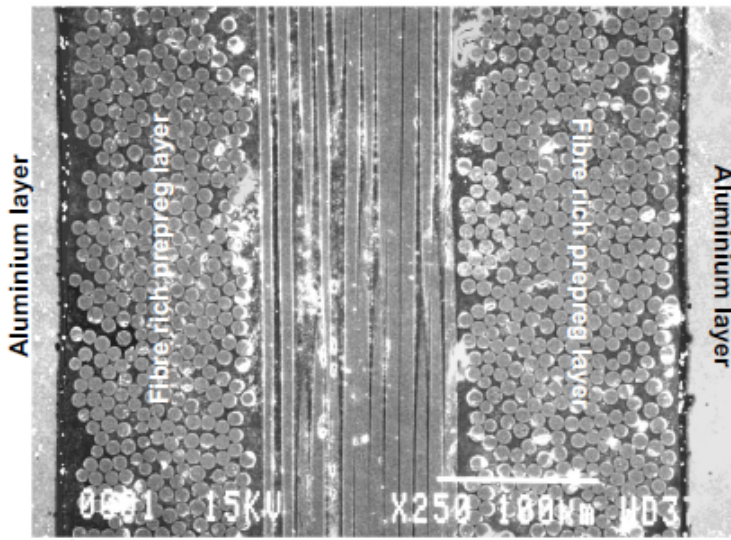
Figure 3.10: Microscope scan of GLARE 4 cross-section [18]

A surface-based cohesive behaviour was implemented in the current model to simulate the behaviour of the resin-rich areas between metal and composite layers. This provides an efficient approach to model cohesive connections based on a traction-separation constitutive model [86]. The surface-based cohesive behaviour in ABAQUS/Explicit uses a linear elastic traction-separation along with damage initiation criteria and damage evolution law. A linear elastic behaviour is assumed at the beginning of the analysis which is described by the stiffness matrix in Equation 3.35. Where the normal (t_n) and shear (t_s, t_t) stresses in the nominal traction stress vector $(\mathbf{t})$ are related to the normal and shear separations. And (K_{nn}, K_{ns}, K_{nt}) are the stiffness components of the adhesive material.

The damage initiation between two cohesive surfaces is defined with a traction separation model shown in Figure 3.11. In the current model, it relies on the maximum stress criterion, as demonstrated in equation 3.36. The initiation criterion is satisfied once the maximum contact stress ratio reaches a value equal to or greater than 1.0. This defines the ratio of the current stresses to the peak stresses (t_n^o, t_s^o, t_t^o), as shown in Figure 3.11.

$$\mathbf{t} = \left\{ \begin{array}{c} t_n \\ t_s \\ t_t \end{array} \right\} = \left[\begin{array}{ccc} K_{nn} & K_{ns} & K_{nt} \\ K_{ns} & K_{ss} & K_{st} \\ K_{nt} & K_{st} & K_{tt} \end{array} \right] \left\{ \begin{array}{c} \delta_n \\ \delta_s \\ \delta_t \end{array} \right\} = \mathbf{K} \cdot \boldsymbol{\delta} \tag{3.35}$$

$$\max \left\{ \frac{\langle t_n \rangle}{t_n^o}, \frac{t_s}{t_s^o}, \frac{t_t}{t_t^o} \right\} = 1 \tag{3.36}$$

$$G^C = G_n^C + \left(G_s^C - G_n^C \right) \left\{ \frac{G_S}{G_T} \right\}^\eta \tag{3.37}$$

Damage degradation begins once the criterion for damage initiation has been met. An energy-based damage degradation model is utilized in the current model, where the energy dissipated due to failure (G^c) defines the area under the mixed mode traction-separation curves shown in Figure 3.11 in yellow. The (G^c) is calculated from the Benzeggagah-Kenane (BK) damage model, illustrated in Equation 3.37. Where the energy dissipation in the normal direction (G_n^c) and transverse direction (G_s^c) are material properties. The BK exponent (η) was set to 1.45.
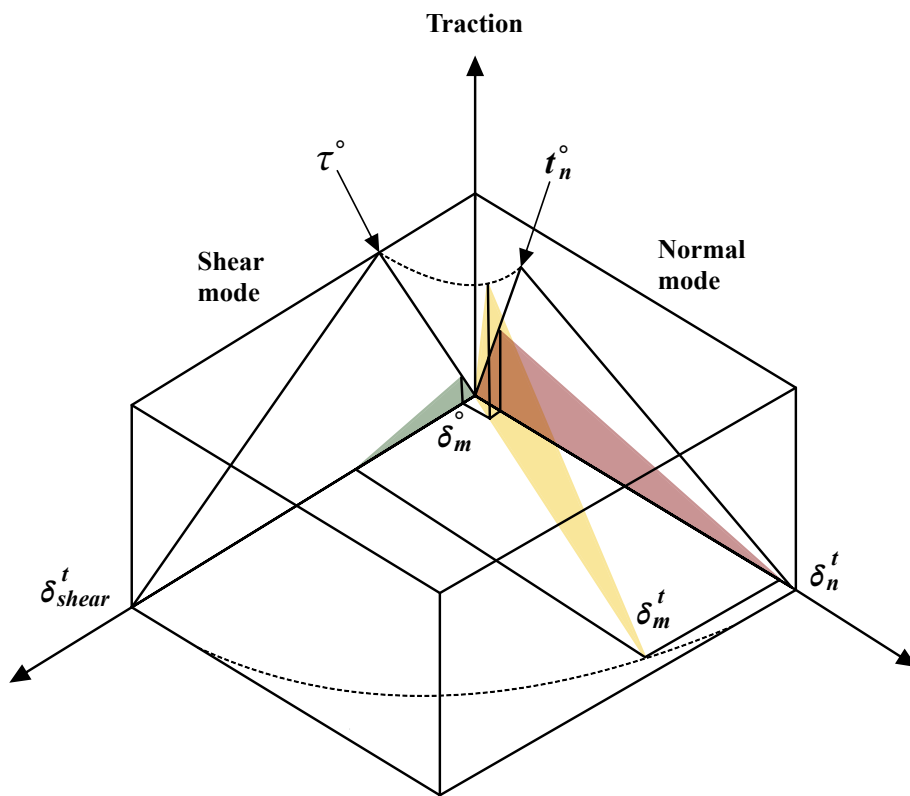
Figure 3.11: Mixed-mode traction-separation

Chapter 4

Validation of composites damage models

4.1   Introduction

This chapter aims to validate the VUMAT subroutine introduced in the previous chapter in order to ensure the model's accuracy before constructing the comprehensive FML model, considering the high complexity of the FML model. The validation involves comparing the tensile strength of a composite material obtained from the current subroutine with experimental data for the same material. The validation is carried out on two models: one with fibres oriented at loading direction (0°), and a second model with fibres oriented transverse to loading direction (90°). This is done to verify the capability of the subroutine on predicting the damage modes accurately. Where fibre tensile damage is expected to be dominant in the 0° specimen and matrix tensile damage is dominant in the 90° specimen.

4.1.1   Overview of composites tensile test experiment

The tensile test experiment employed for validation in this chapter is sourced from [12]. The experiment followed the ASTM standard (D3039), which outlines the procedure for determining the tensile properties of polymer matrix composite materials experimentally [4]. The experiments were conducted using an Instron 8501 with a load cell of 100 kN as illustrated in Figure 4.1-a. The specimens were made with carbon fibre (T700) and epoxy resin using the resin transfer infusion (RTI) system, where the fibre volume fraction is 50%. Both specimens were constructed with four laminae with a total thickness of 1.2mm. The 0° specimen has in-plane dimensions of $250mm \times 15mm$, while the 90° specimen has dimensions of $175mm \times 25mm$. Both experiments were repeated three times and the average was considered. During the experiment, the 0° specimen showed multiple abrupt cracks at failure as shown in Figure 4.1-b, indicating fibre breakage and matrix cracking along the loading direction. However in the case of 90° specimen, a single clean crack is observed at failure as demonstrated in Figure 4.1-c.
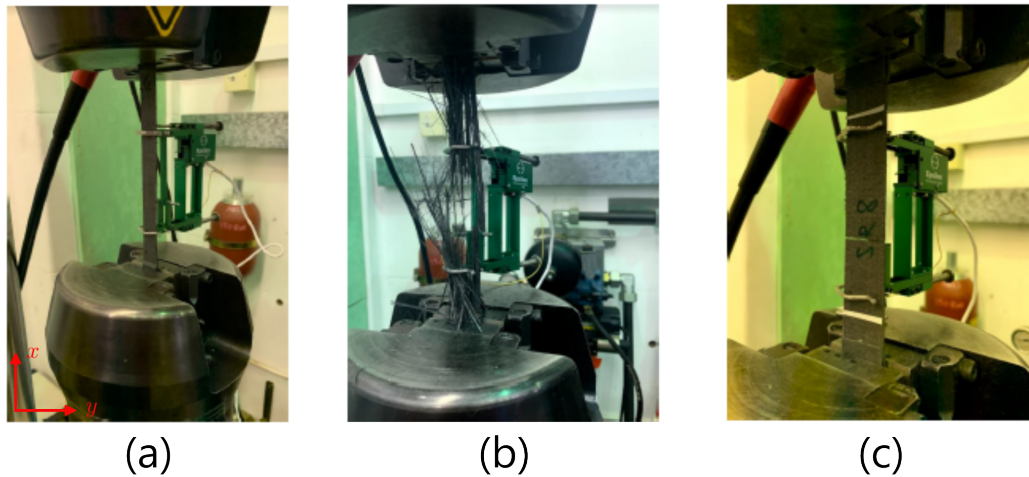
Figure 4.1: Tensile test specimens of CFRP: (a) specimen before damage, (b) 0° specimens after damage and (c) 90° specimens after damage [12]

4.1.2   FE model of composites tensile test

The current section presents the development of FE models that aim to replicate the experimental results of the tensile test presented in the previous section. Both models consider the full depth and the width of the tested specimens, however, only the length outside the grippers is considered, for the 0° specimen the length is 138mm and 125mm for the 90° specimen. The specimens are fixed in all degrees of freedom at the clamping end, whereas the loading end is allowed to deform only in the load direction, with a displacement applied to the loading end at the x-direction. The material properties in Tables 4.1, 4.2 and 4.3 are applied to the specimens.

Table 4.1: Elastic properties of CFRP T(700)/epoxy [12]

E_1(GPa)	E_2, E_3(GPa)	G_{12}, G_{13}(GPa)	G_{23}(MPa)	ν_{12}, ν_{13}
118	6.7	5.39	3.2	0.33

Table 4.2: Strength of CFRP T(700)/epoxy [12]

X^T(MPa)	X^C(MPa)	Y^T(MPa)	Y^C(MPa)	S^L(MPa)
1837.5	900	29	199.8	192.3

Table 4.3: Fracture energies of CFRP [81]

G_{ft}(N/mm)	G_{fc}(N/mm)	G_{mt}(N/mm)	G_{mc}(N/mm)
81.5	106.3	0.2774	1.3092

4.1.3   Validation of the 0° and 90° CFRP tensile tests

The FE models were constructed with element sizes (2mm, 1mm and 0.5mm) to ensure convergence. Specimens were assigned the 3D 8-node linear brick elements with reduced integration (C3D8R) available in Abaqus and the mesh was

consistent throughout the specimen. The stress-strain diagrams were obtained for each mesh size and the results are plotted along with the experimental data for the 0° and 90° specimens in Figures 4.2 and 4.4 respectively.

In the case of the 0° specimen, the failure stress and strain values slightly increased with mesh refinement, and the 0.5mm mesh size resulted the closest values to the experimental data. The strength of the specimen is recorded as 1845.7 MPa and Young's modulus is 119.8 GPa. Two failure modes were observed in this specimen: Fibre tensile and matrix tensile damage, as shown in Figure 4.3. Matrix cracks were formed along the loading direction parallel to the fibres, as illustrated in Figure 4.3-a. This simulates the debonding between the fibres and matrix, similar to the experimental observations in Figure 4.1-b. Fibres mainly failed transverse to the load direction, as indicated by the vertical cracks in Figure 4.3-b. The fibre damage was concentrated near the supports as they bear the highest load.
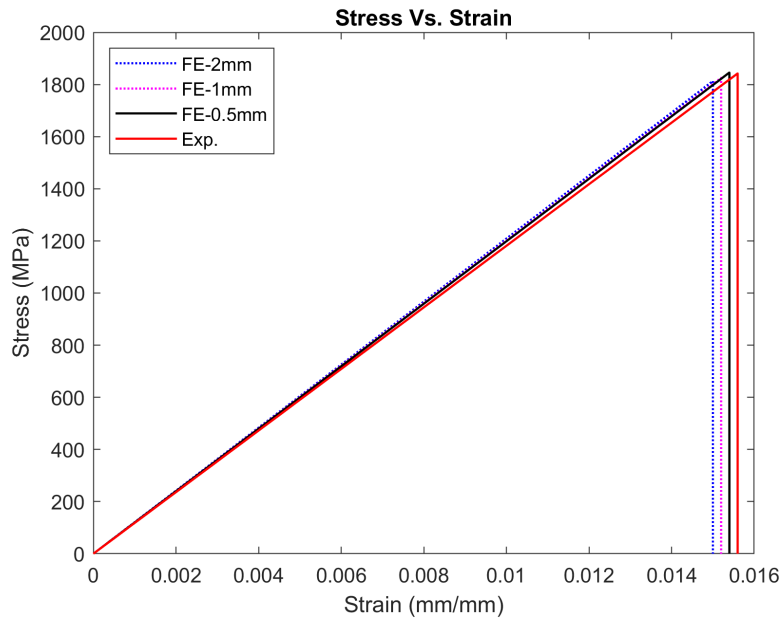
Figure 4.2: Stress vs Strain curve of the 0° specimen

(a) Matrix tensile damage (d_{mt})

(b) Fibre tensile damage (d_{ft})
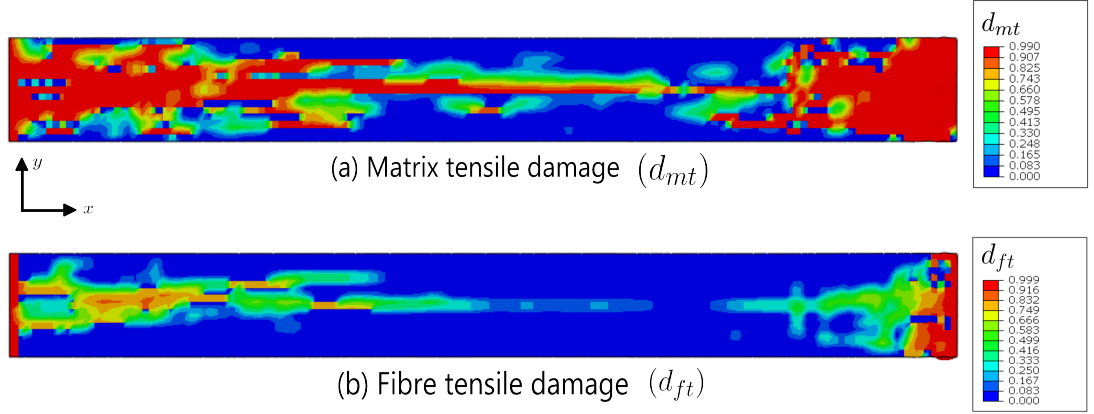
Figure 4.3: Fibre tensile damage (a) and matrix tensile damage (b) in the 0°
specimen

For the 90° specimen, the stress values slightly increased with mesh refinement, as
shown in Figure 4.4. Where the stress-stain diagram shows good agreement with
the experimental data. The strength is determined as 29.41 MPa and Young's
modulus is 6.68 GPa. During the simulation, the only failure mode observed in
this specimen is matrix tensile damage. This damage mode initiates first near
the supports as they bear the highest load, then an additional crack appeared in
the central area closer to fixed end of the specimen, as illustrated in Figure 4.5.
Matrix tensile damage in this case indicates matrix cracking perpendicular to the
loading direction, which is similar to the experimental observations in Figure 4.1-
c. The strength of this specimen is much lower than the strength of the specimen
with 0° fibres, as most of the load was carried by the matrix. This indicates the
importance of fibre directions in engineering applications.
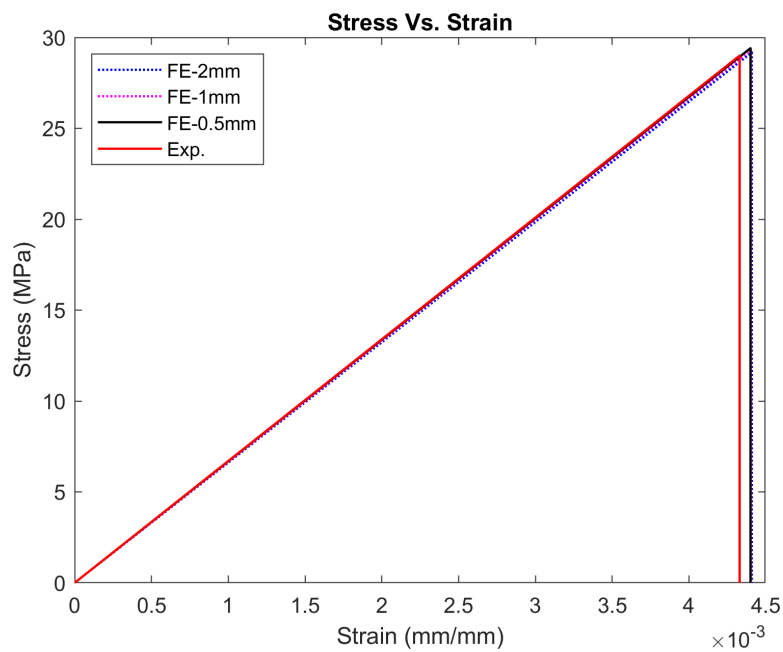
Figure 4.4: Stress vs Strain curve of the 90° specimen

Figure 4.5: Matrix tensile damage in the 90° specimen

Chapter 5

Investigating tensile loading-induced damage in GLARE

5.1 Introduction

This chapter investigates the failure process of GLARE in an open-hole tensile test under uniaxial tensile load. The open-hole or blunt notch strength is defined as the strength of a structure containing a hole, an important design parameter for aircraft parts subjected to high tensile and bending stresses [99]. Aircraft structures contain unavoidable holes in areas where connections are necessary such as windows, doors and hatches [99]. Notably, the inclusion of such holes in FML layers creates weakened regions where stress concentrates. Furthermore, drilling a hole in an FML structure will disrupt the continuity of fibres resulting in a significant reduction in its properties. This will also influence the damage process as will be shown in the following sections.

5.2   The FE model of OHT test of GLARE

The open hole tensile test of GLARE is simulated based on the specifications of experimental testing done by De Vries [18]. A coupon specimen with a single central hole is used in the experimental test, the length, width and hole diameter of the specimen are set to 300mm, 50mm and 4.8mm respectively as illustrated in 5.1. These dimensions were suggested by De Vries [18] and will be constants in the simulations presented in this chapter. The specimen consists of GLARE variant (GLARE 3 3/2-0.3), which is typically used for fuselage skin. The ratio (3/2) indicates the amount of aluminium layers (3) to fibre prepreg layers (2) and the number 0.3 is the thickness of a single aluminium sheet in mm. Each prepreg layer combines two unidirectional S2 glass fibre layers, where the fibres are oriented in two directions, with one direction perpendicular to the other, a [0°,90°] and [+45°,-45°] layups were considered for this study. The thickness of a prepreg layer between two aluminium sheets is 0.25mm as shown in Figure 5.2. It is worth mentioning that the time step was set to 0.007 seconds, and the simulation was performed on a computer equipped with 8 cores, 16 threads and 2.90 GHz processor.
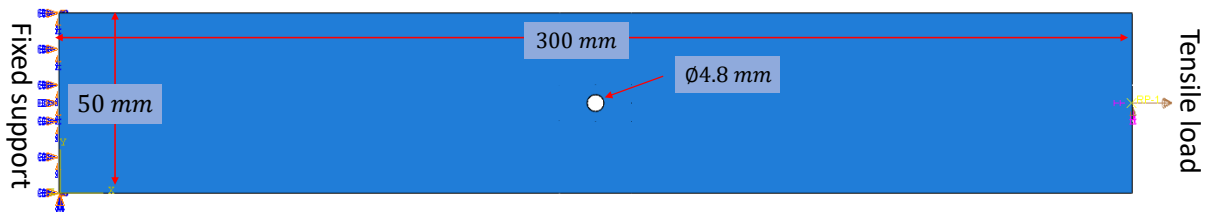
Figure 5.1: GLARE-3 specimen geometry

In the FE model, the specimen is fixed in all degrees of freedom at the clamping end, while the loading end is allowed to deform only in the load direction as shown in Figure 5.1. A displacement of 5mm is applied at a reference point located at the middle of the loading edge, where all nodes at the loading edge are coupled to a reference point, this simplifies data collection in the post-processing stage.
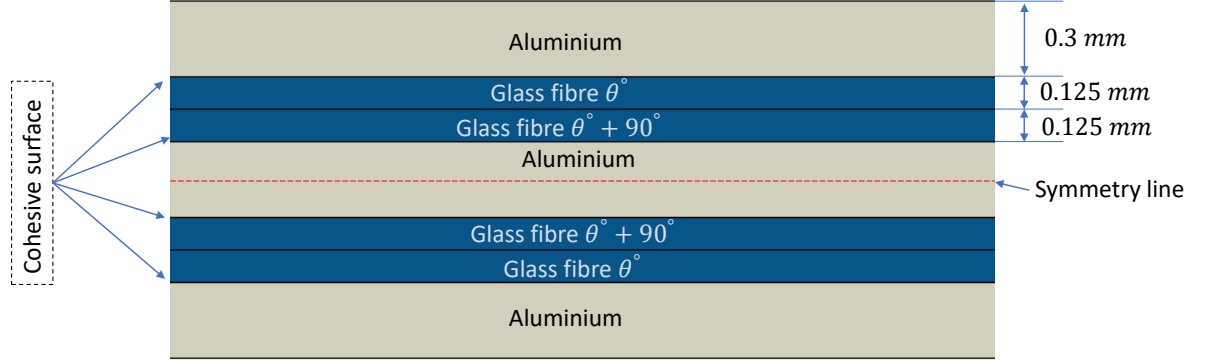
Figure 5.2: Cross-sectional view of GLARE 3 specimen

As this research is aimed at studying the fracture of FMLs, a full model of the specimen should be modelled to predict the failure mechanisms and cracks at failure. The full specimen is considered in this study, therefore all the layers were modelled with the actual dimensions of the test specimen. The layers were combined together as shown in Figure 5.2, where a cohesive interaction was defined at the interface of the layers.

A surface-based cohesive behaviour was implemented in the current model to simulate the behaviour between metal and composite layers, where the cohesive model parameters are listed in Table 5.1. The interface between two prepreg layers with different orientations is assumed to be perfectly bonded. Therefore, surface-to-surface tie constraint is applied at those interfaces. In this approach, all displacement and rotation degrees of freedom are tied between two surfaces known as slave and master surfaces. This ensures equal translational and rotational

motion for the two surfaces. In the current simulation, the choice of slave and master surfaces does not affect the accuracy of the results as both surfaces are deformable and have the same mesh density.

Table 5.1: Cohesive model parameters

E(GPa)			(MPa)			G_c(N/mm)		
K_{nn}	K_{ss}	K_{tt}	t_n^0	t_t^0	t_t^0	$G_{|c}$	$G_{||c}$	$G_{|||c}$
2	0.75	0.75	65	38	38	2	3	3

5.3   Material properties of GLARE

The aluminium layers in GLARE were assigned the elastic properties of aluminium 2024-T3 listed in Tables 5.2 and 5.3. The plasticity of aluminium was considered with isotropic hardening data available in [50]. Whereas the behaviour of Glass fibre layers is assumed to be transversely isotropic; the elastic material properties and strength values of glass fibre are listed in Tables 5.4 and 5.5 respectively. The damage model implemented for glass fibre layers depends on fracture energies defined in Table 5.6.

Table 5.2: Mechanical properties of aluminium 2024-T3 [50, 108]

$\rho(Kg/m^3)$	ν	E(GPa)	Yield strength (MPa)	Fracture energy (J/m^2)
2770	0.33	72.2	300	10.2

Table 5.3: Johnson-Cook parameters for aluminium 2024-T3 [55]

d_1	d_2	d_3	d_4
0.13	0.13	1.5	0.011

Table 5.4: Orthotropic elastic properties of glass fibre prepreg [50]

E_1(GPa)	E_2, E_3(GPa)	G_{12}, G_{13}(GPa)	G_{23}(MPa)	ν_{12}, ν_{13}
55.0	9.5	5.5	3.0	0.33

Table 5.5: Orthotropic strength of glass fibre prepreg [50]

X^T(MPa)	X^C(MPa)	Y^T(MPa)	Y^C(MPa)	S^L(MPa)
2500	2000	50	150	50

Table 5.6: Fracture energies of glass fibre prepreg [78]

G_{ft}(N/mm)	G_{fc}(N/mm)	G_{mt}(N/mm)	G_{mc}(N/mm)
32	20	4.5	4.5

5.4   Mesh sensitivity analysis

All layers contained in the FML FE models were assigned the 3D 8-node linear brick elements with reduced integration (C3D8R) available in Abaqus. FML layers were partitioned as shown in Figure 5.3, in order to ensure a consistent re-meshing strategy in the mesh sensitivity study. The re-meshing was done in the central section of the layers and across the aluminium layers (in some cases), as shown in Figure 5.3 and Table 5.7. This approach was adopted as cracks were expected to initiate at the notch edges and propagate in the regions above and below the notch. Mesh sensitivity and error calculation were conducted for the on-axis model and were plotted against the total number of elements in the model as illustrated in Figure 5.4. The error in Ultimate Tensile Strength (UTS) was obtained by comparing the FE model results with experimental results for similar specimens, using Equation 5.1. The dimensions of the refined elements are listed in Table 5.7 for each refinement increment, where (a & b) are in-plane and (c & c1) are the through-thickness dimensions for glass fibre and aluminium layers respectively. The aspect ratio, in Table 5.7, refers to the ratio between the longest and shortest edge of an element. Ideally, a perfect value would be 1.0; however, achieving this value is challenging in the current model due to the small thickness of the glass fibre layers, which is 0.125mm. Nevertheless, in the present investigation, the aspect ratio is considered in the mesh refinement strategy, with

a value of 2.0 achieved in the most refined model.

$$error = \frac{\mid S_{numerical} - S_{experimental} \mid}{S_{experimental}} \qquad (5.1)$$
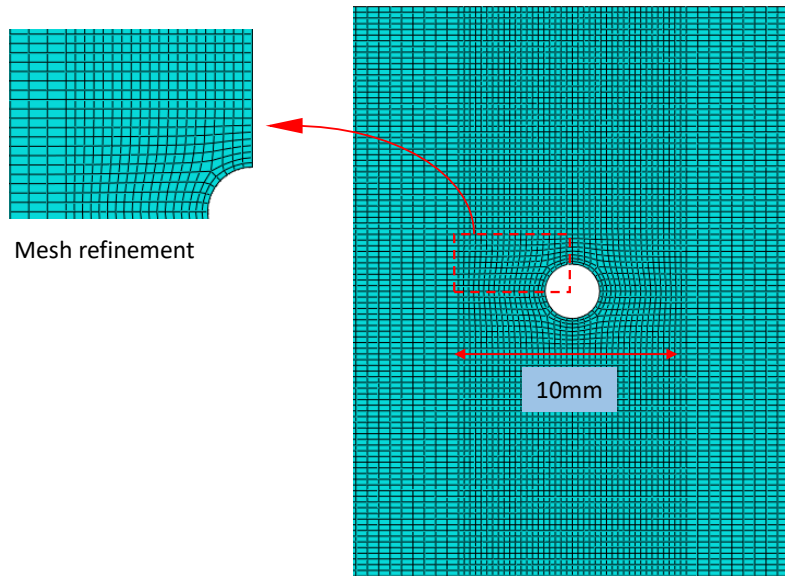
Figure 5.3: Mesh refinement strategy

Table 5.7: Element Sizes for each model (Number of elements): In-plane (a, b) and through-thickness (c, c1) dimensions for glass fiber and aluminum layers

Number of elements	Element size (mm)				Aspect ratio
	a	b	c	c1	
55972	1	1	0.125	0.3	8
71666	0.8	0.8	0.125	0.3	6.4
125580	0.5	0.5	0.125	0.3	4
209272	0.35	0.35	0.125	0.3	2.8
249657	0.3	0.3	0.125	0.3	2.4
298720	0.3	0.3	0.125	0.15	2.4
350432	0.25	0.25	0.125	0.15	2
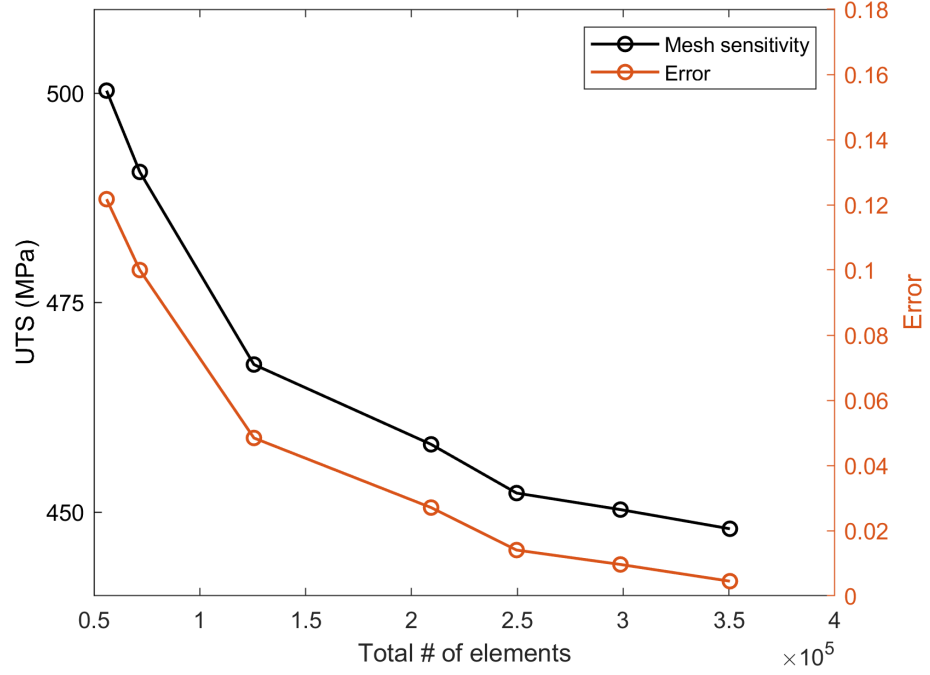
Figure 5.4: Ultimate tensile strength and corresponding error vs. number of elements for on-axis GLARE

As illustrated in Figure 5.4, the initial mesh size is $(1mm \times 1mm)$, which resulted in more than 10% error, and the simulation for this mesh required approximately 2.2 hours. Four mesh refinements were conducted on dimensions (a & b), which resulted in an aspect ratio of 2.4 and reduced the error to approximately 1.5%. Further mesh refinement in (c & c1) decreased the error to less than 1%, but increased the total number of elements to (3.5×10^5), which significantly increased the computational time to approximately 25.8 hours. The mesh convergence is accomplished with the model containing (2.0×10^5) elements, This model comprises elements with $(0.3mm \times 0.3mm)$ in-plane and one element through the thickness direction of each layer, for this mesh the aspect ratio is calculated as 2.4. The error associated with this model is approximately 2%, as shown in Figure 5.4. Therefore, it is considered as the most cost-efficient model.

5.5   Results and discussion of on-axis GLARE

5.5.1   The mechanical behaviour of notched on-axis GLARE

The stress-strain curve of the on-axis open-hole tensile test specimen of GLARE is illustrated in Figure 5.5. The stress was calculated using the net blunt notch strength (S_{BN}) using equation 5.2, where F_{max} is the maximum force, W is the total width, D is the diameter and t is the thickness of the specimen.

$$S_{BN} = \frac{F_{max}}{(W - D)t} \tag{5.2}$$

The curve consists of three stages, starting with a linear elastic zone where the stress is proportional to strain, at which the Young's modulus is calculated as (65.8 GPa). The second stage is a non-linear transition zone representing the yield of the aluminium layer in the FML. After yielding the specimen continued to deform in a linear behaviour in the third stage until reaching the full failure. The curve shows a sudden drop in stress at the failure point, indicating a brittle failure for on-axis FMLs. The UTS was calculated as (450 MPa) which correlated well with experimental values.

Three points are pointed in Figure 5.5 at the three stages of the stress-strain curve. Point-A is located in the elastic region, Point-B at the transition and point-C at the post-yield regions respectively. The Von-Mises stress distribution for each layer at the three stages is illustrated in Figure 5.6. As evident from Figure 5.6, the FE simulation indicated a higher degree of stress concentration in the aluminium layers compared to the 0° and 90° glass fibre layers from the beginning of the test until point-A. At point-A, however, the stress reached the
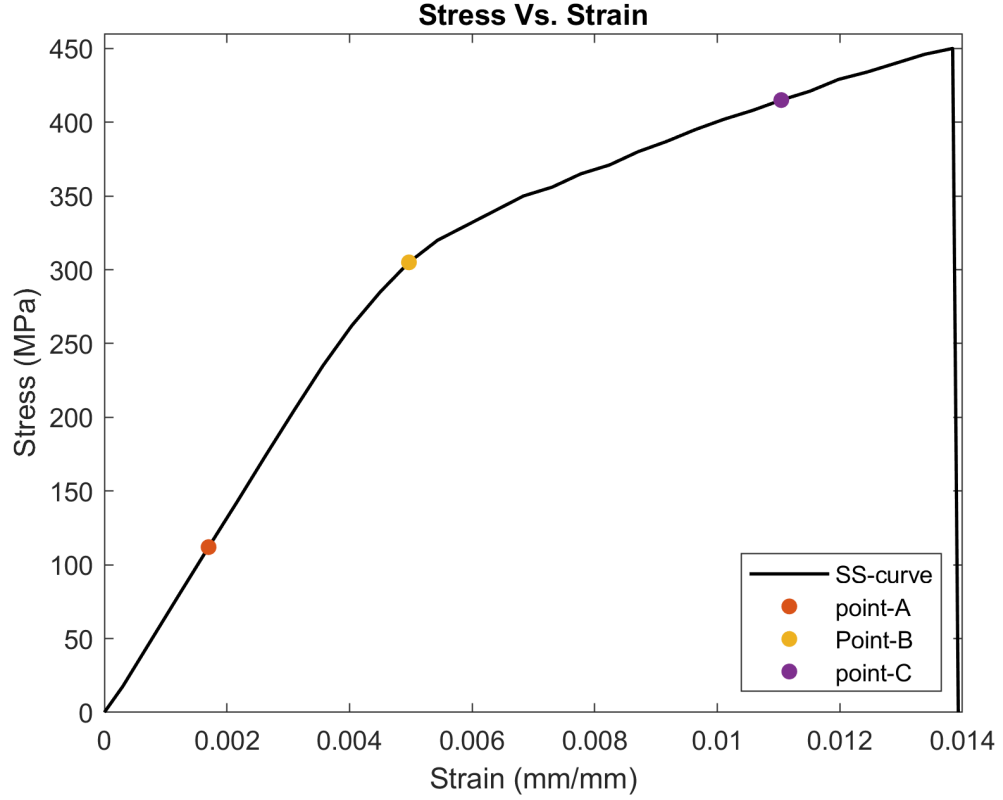
Figure 5.5: Stress-strain curve for on-axis GLARE

yield limit of aluminium at the notch root of aluminium layers. Therefore, after this stage, the stress concentration had transferred to the 0° glass fibre layers, as shown in stage-B of Figure 5.6, the 90° glass fibre layers are still not showing any serious concentration of stress at this stage. At the final stage before failure (Point-C) the maximum stress value was recorded as (1.2 GPa) at the 0° glass fibre layers. However, the stress concentrated above and below the notch, as the elements were very close to full failure states. In oppose to the first and second stages, the third stage showed some stress concentration at the notch of the 90° glass fibre layers prior to failure. Overall less stress is noticed in the 90° glass fibre layers as these layers are pulled transverse to the fibre's direction. Whilst the strength across fibre direction corresponds to the strength of the matrix material as the fibres are not carrying a considerable amount of load.
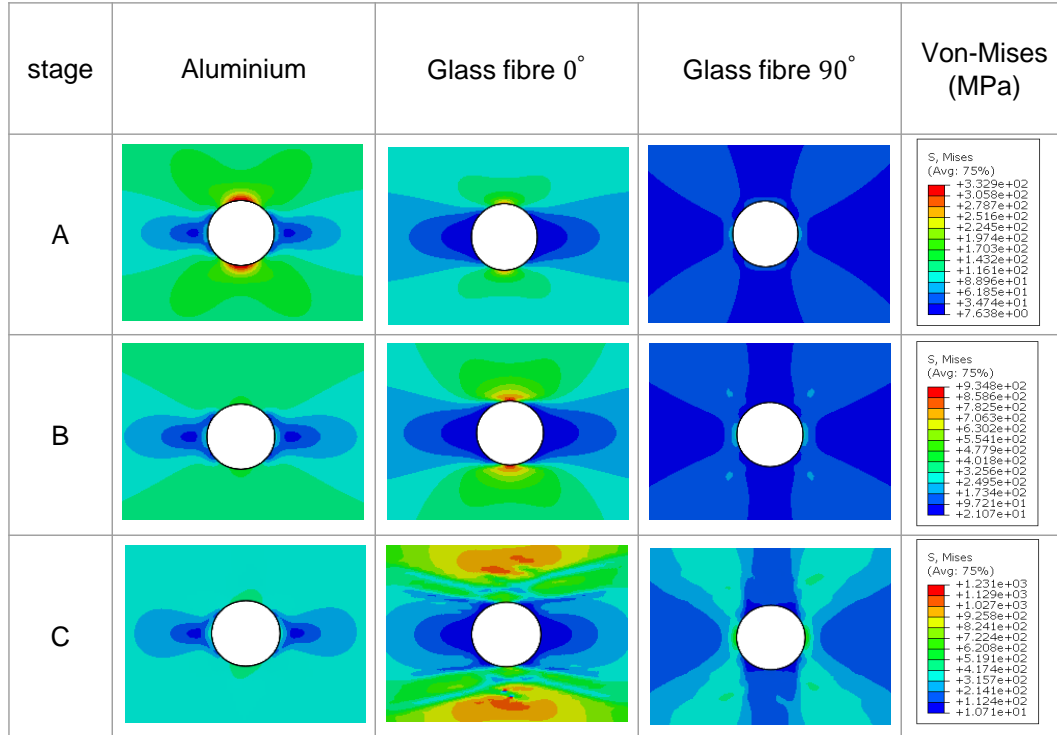
Figure 5.6: Stress concentration in on-axis GLARE layers at different stages

5.5.2   Damage modes and failure sequence in on-axis GLARE

The damage mechanisms captured during the open hole tensile test of GLARE involved fibre breakage, matrix cracking, delamination and plastic damage of aluminium layers. In the following sections, the critical failure modes will be analysed in each constituent of GLARE.

Progressive damage in glass fibre layers

The progressive damage in glass fibre layers is analysed for both the 0° and 90° layers at three critical UTS stages. For the 0° glass fibre layers, the damage initiation started at (320 MPa), as shown in Figure 5.7, where four cracks appeared at the notch edge parallel to the loading direction. As the load increases, additional cracks begin to initiate and propagate in the regions located above and below the notch, as illustrated in Figure 5.7 at (407.1 MPa) and (439.8 MPa). Prior to full failure of the specimen, at (439.8 MPa), some elements were deleted in the 0°

glass fibre layers, indicating fibre breakage at the notch root. At this stress level, the maximum fibre tensile damage reached ($d_{ft} = 0.98$) at the red regions. The 0° glass fibre layers also showed matrix cracking as illustrated in the bottom row of Figure 5.7. Matrix cracks formed along the direction of the fibres, indicating debonding between glass fibres and the epoxy surrounding them.
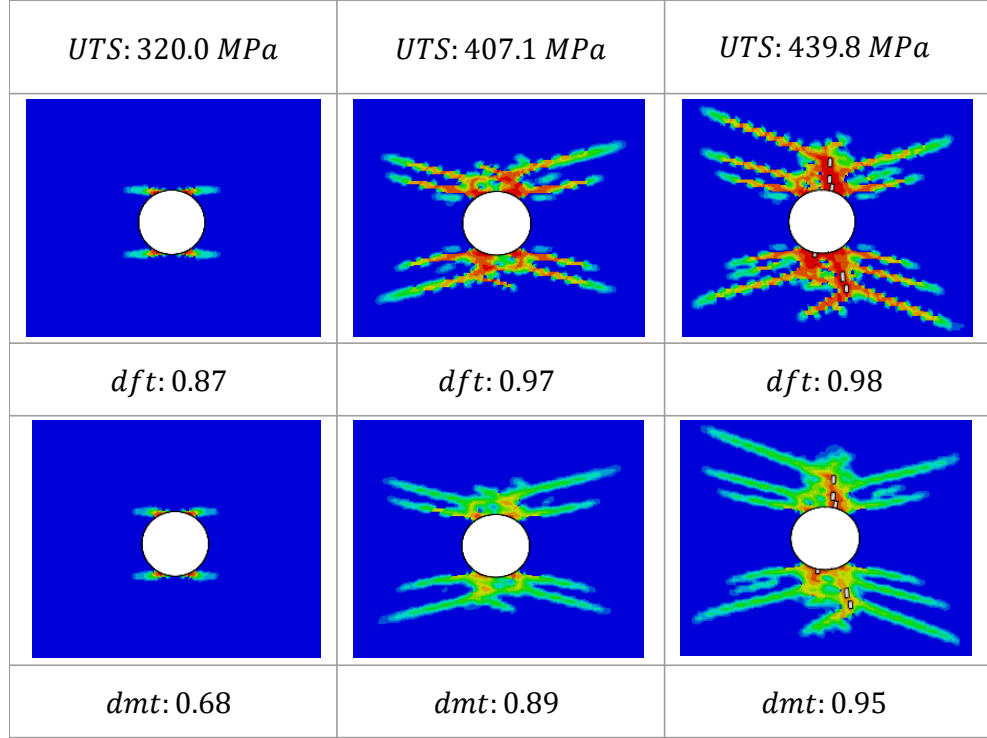
Figure 5.7: Fibre (d_{ft}) and matrix (d_{mt}) tensile damage propagation in the 0° glass fibre layers

Figure 5.8 displays the final cracks in the 0° glass fibre layers, revealing a long crack transverse to the loading direction almost at the centre line of the specimen. The final crack was formed in this direction as the matrix cracks propagated in same path, which contributed to a weakened region at the centre line. Furthermore, crack branching longitudinal to the loading direction was evident at the end of the simulation, as shown in Figure 5.8. Those cracks appeared on the outer layers of the specimen, showing critical values for fibre tensile damage ($d_{ft} = 0.94$) and matrix tensile damage ($d_{ft} = 0.94$). In addition, the cracks were slightly inclined as a result of varying stress levels in Glare layers, where shear

stress developed within the layers

<div align="center">

d_{ft}: 0.94 d_{mt}: 0.99

</div>
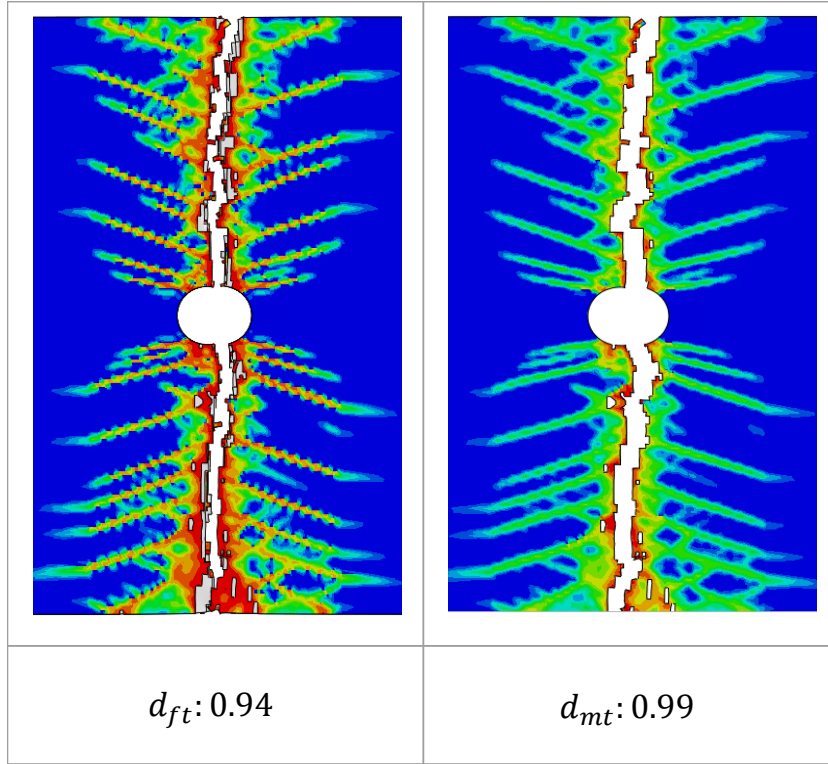
Figure 5.8: Final cracks in the 0° glass fibre layers

In the OHT simulation of GLARE, the only failure mechanism evident in the 90° glass fibre layers is matrix cracking. Figure 5.9 illustrates matrix cracking at various UTS and matrix tensile damage variable levels. Matrix tensile damage initiated initially at the upper and lower sides of the notch as shown in Figure 5.9, the cracks then propagate transverse to the loading direction and some elements are deleted at (439.8 MPa), while the (d_{mt}) increases to 0.99. These layers are considered the weakest in bearing tensile loads due to the transverse orientation of the fibres with respect to the loading direction. Therefore, the matrix will bear most of the load in these layers, despite being weakest in tensile strength as indicated in Table 6.2 ($Y^T = 50MPa$). The final crack in these layers is a sudden crack occurring at ($UTS = 450.3MPa$), indicating a brittle failure.
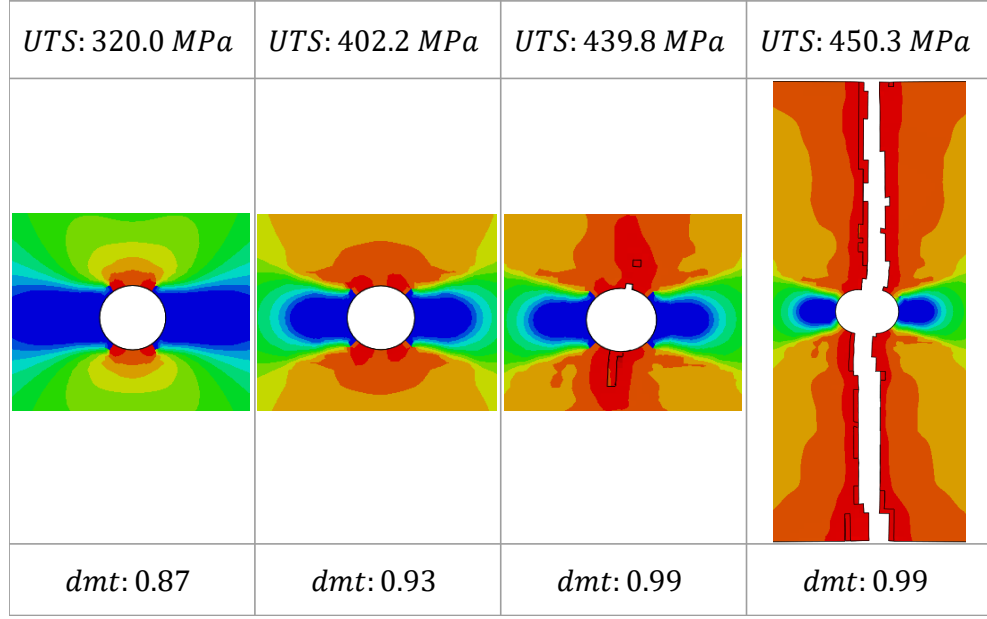
Figure 5.9: Damage propagation in the 90° glass fibre layers

Progressive damage in aluminium layers

Similar to glass fibre, the damage in aluminium layers is analysed at various UTS and Johnson-Cook damage initiation criterion (JCCRT) as illustrated in Figure 5.10. The first contour plot was captured at $(320MPa)$, where the elements at the notch reached the yield limit due to stress concentration. The plastic damage was initiated at $(320MPa)$ as the JCCRT indicates, but it is still far beyond full failure. As the tensile loading continues, the JCCRT grow at a localized area near the notch root. However, no evident cracks were formed in the aluminium layers prior to the full fracture of the specimen, this is clearly shown in Figure 5.10 at $(UTS = 439.5MPa)$. The JCCRT approached a full failure state (1.0) upon the moment of the final crack propagation in the specimen.

Progressive damage at Al/glass fibre interface

Delamination usually occurs at the interface of Al/glass fibre due to the differences in material behaviours between the layers which result in different stress states at

UTS: 320 MPa	UTS: 402.2 MPa	UTS: 439.8 MPa	UTS: 450.3 MPa
JCCRT: 0.22	JCCRT: 0.511	JCCRT: 0.99	JCCRT: 1.0
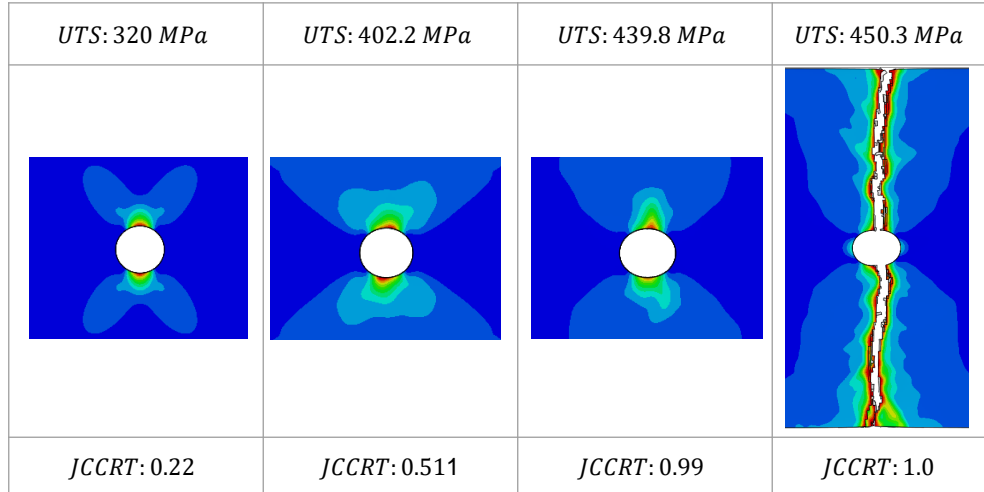
Figure 5.10: Damage propagation in aluminium layers in on-axis GLARE

each layer as was shown earlier in Figure 5.6. Thus, debonding of Al/glass fibre is expected to occur at the notch edges. Figure 5.11 illustrates the maximum contact stress damage initiation (CSMAXSCRT) under various UTS values. The CSMAXSCRT in the first two plots indicates the possibility of initiation of delamination at the notch edges, and propagation along the loading direction. At the moment of element deletion in glass fibre layers at $(439.8 MPa)$, the contact stress at the interface exceeded the interlaminar bond strength of epoxy. Resulting in delamination around the notch and along the final crack, with the CSMAXSCRT approaching 1.0.

UTS: 320.0 MPa	UTS: 402.2 MPa	UTS: 439.8 MPa	UTS: 450.3 MPa
CSMAXSCRT: 0.26	CSMAXSCRT: 0.47	CSMAXSCRT: 1.0	CSMAXSCRT: 1.0
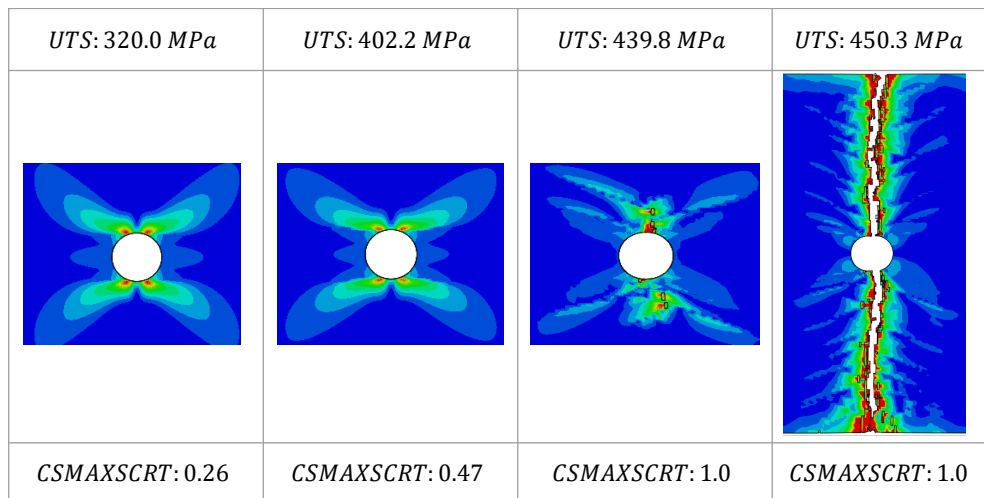
Figure 5.11: Damage initiation at Al/glass fibre interface in on-axis GLARE

5.6   Results and discussion of off-axis specimen

This section presents an FE simulation for an off-axis FML with the aim of investigating the effect of off-axis fibre angles on the mechanical behaviour and failure mechanisms of FMLs. Similar to the previous case, this simulation is performed on an open hole tensile test replicating the experimental test of the OHT test of GLARE 3 conducted by De Vries [18]. The specimen dimensions, boundary conditions and loading are similar to the ones presented in the previous section, illustrated in Figures 5.1 and 5.2. The only difference between the two models lies in the fibre orientation, in the current model it is set at $[\pm 45°]$ from the loading direction.

5.6.1   The mechanical behaviour of notched off-axis GLARE

The stress-strain relationship of the off-axis GLARE specimen is illustrated in Figure 5.12. The curve shows three regions, each indicated with a coloured dot in Figure 5.12, starting with a linear elastic region (Point-A), where the Young's modulus is calculated as ($59.6\ GPa$). Followed by a non-linear curve indicating the ductility in the material (Point-B) and concluding with a post-yield region (Point-C). After yielding, the specimen continued to deform in an approximately linear behaviour until reaching the ultimate tensile strength ($300 MPa$). The failure of the specimen was gradual as illustrated in Figure 5.12, where it experienced around 0.003 strain from the ultimate tensile strength until complete failure.

The contour plot of Von-Mises stress is presented in Figure 5.13 for each individual layer of GLARE across the three stages of the stress-strain curve, indicated with (A, B, C). Point-A is located within the elastic region, Point-B marks the yield zone and point-C denotes the post-yield region. For aluminium layers, the stress concentrated uniformly at the notch edges transverse to the loading direction from the beginning of the simulation until approaching the yield point of aluminium

(stage-A). As the load continues to rise, the stress increases in the aluminium layers at an angle approximately equal to the orientation of the fibre angles [±45°], as seen in stages B & C in Figure 5.13. This is attributed to the shear stress developed in these layers as a result of the opposing stress directions in the [±45°] glass fibre layers. For the glass fibre layers, the stress distribution in the +45° mirrored that of the −45°. Overall the stress concentrated at the fibre orientation in the glass fibre layers as indicated in stage-A of Figure 5.13. For each glass fibre layer, the stress rises mainly along the orientation angles within that layer as shown in stages B & C. Finally, the stress distribution in the off-axis specimen is affected by the angle directions, with higher Von-Mises stress magnitude noticed in the aluminium layers compared to glass fibre layers.
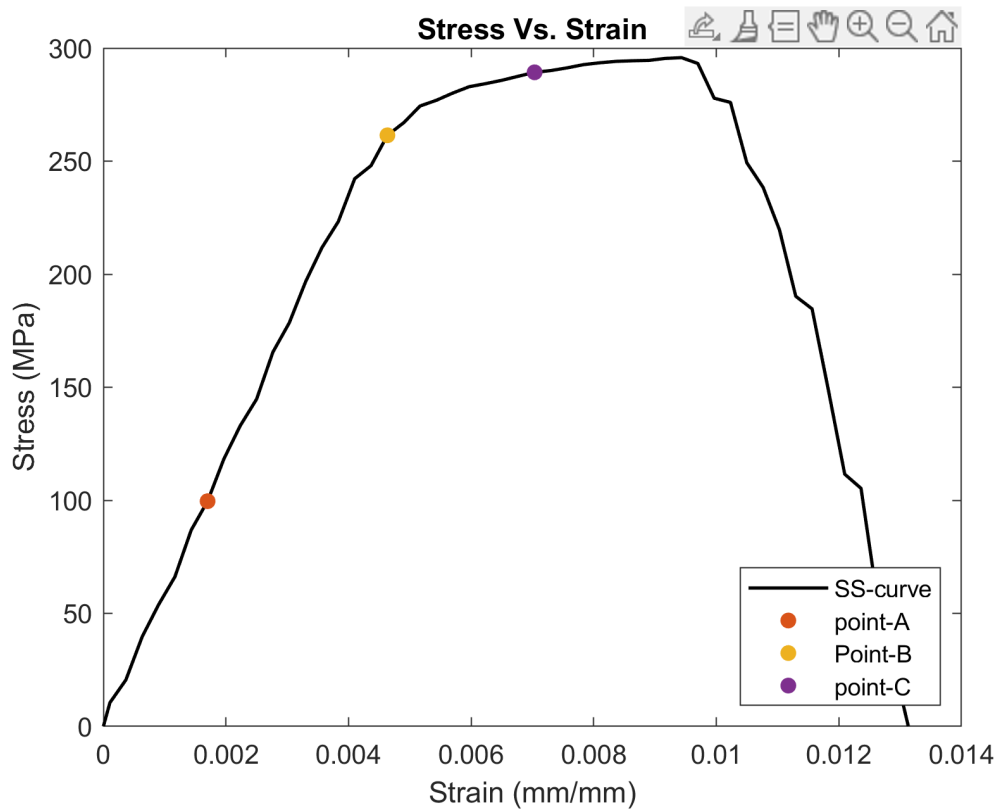
Figure 5.12: Stress-strain curve for off-axis GLARE
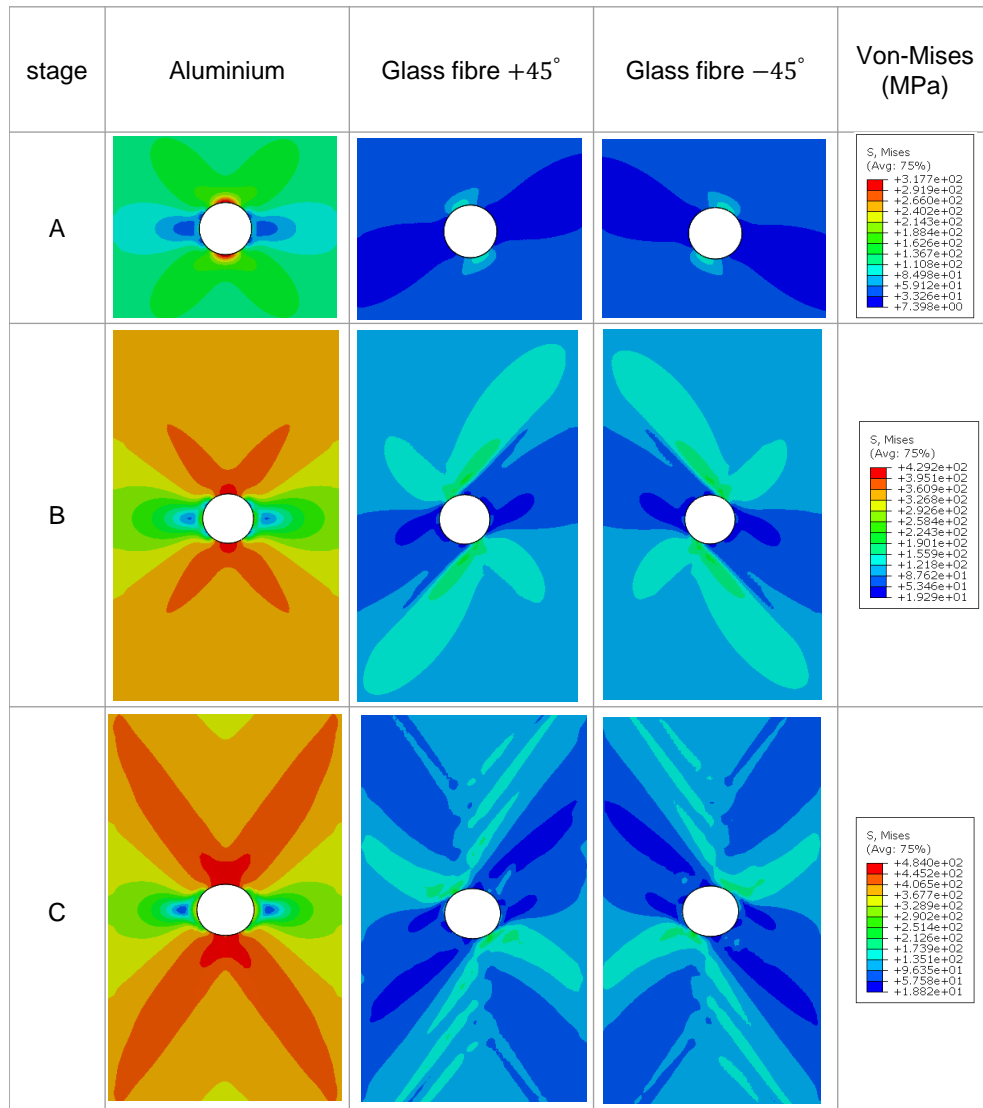
Figure 5.13: Stress concentration in off-axis GLARE layers at different stages

5.6.2   Damage modes and failure sequence in off-axis GLARE

Progressive damage in glass fibre layers

Fibre tensile damage began to concentrate near the notch edges during the elastic region, the damage initiation started at the hole tips transverse to the loading direction as illustrated in Figure 5.14. Fibre tensile damage (d_{ft}) subsequently propagated along the [$\pm 45°$] direction, with multiple cracks increasingly appearing at the notch root and propagating along the direction of the fibres. This phenomenon occurred at UTS=274.4 MPa as shown in Figure 5.14, where d_{ft} equals 0.92. The cracks continued to propagate until reaching a UTS of 290.1 MPa, where the elements began to lose their bearing capacity and were subsequently deleted. The matrix tensile damage initiated in a similar manner, at the elastic stage the matrix tensile damage (d_{mt}) started approximately at UTS=223.3 MPa as shown in Figure 5.14. Then matrix cracks extended at the fibres direction until approaching the critical value of ($d_{mt} = 0.99$), where elements are deleted around the notch. It is worth mentioning that similar crack propagation paths where observed in an experimental OHT test of an off-axis composite conducted by [28]. In the experiments, matrix cracks were evident along [$\pm 45°$] direction, which resulted in fibre breakage at the end of the test.

The ultimate crack in the off-axis GLARE is illustrated in Figure 5.15. Although crack propagation occurred along the direction of the fibre orientation angles before complete failure, as shown in Figure 5.14, the initial crack initiation took place at the notch tip, where stress concentration is most evident. Therefore, the elements in these regions, above and below the notch, are deleted first due to the high stress levels. Subsequently, the stress concentration shifts towards the crack tip, until it covers the entire specimen.

$UTS: 223.3\,MPa$	$UTS: 274.4\,MPa$	$UTS: 290.1\,MPa$
$dft: 0.77$	$dft: 0.92$	$dft: 0.98$
$dmt: 0.56$	$dmt: 0.76$	$dmt: 0.99$
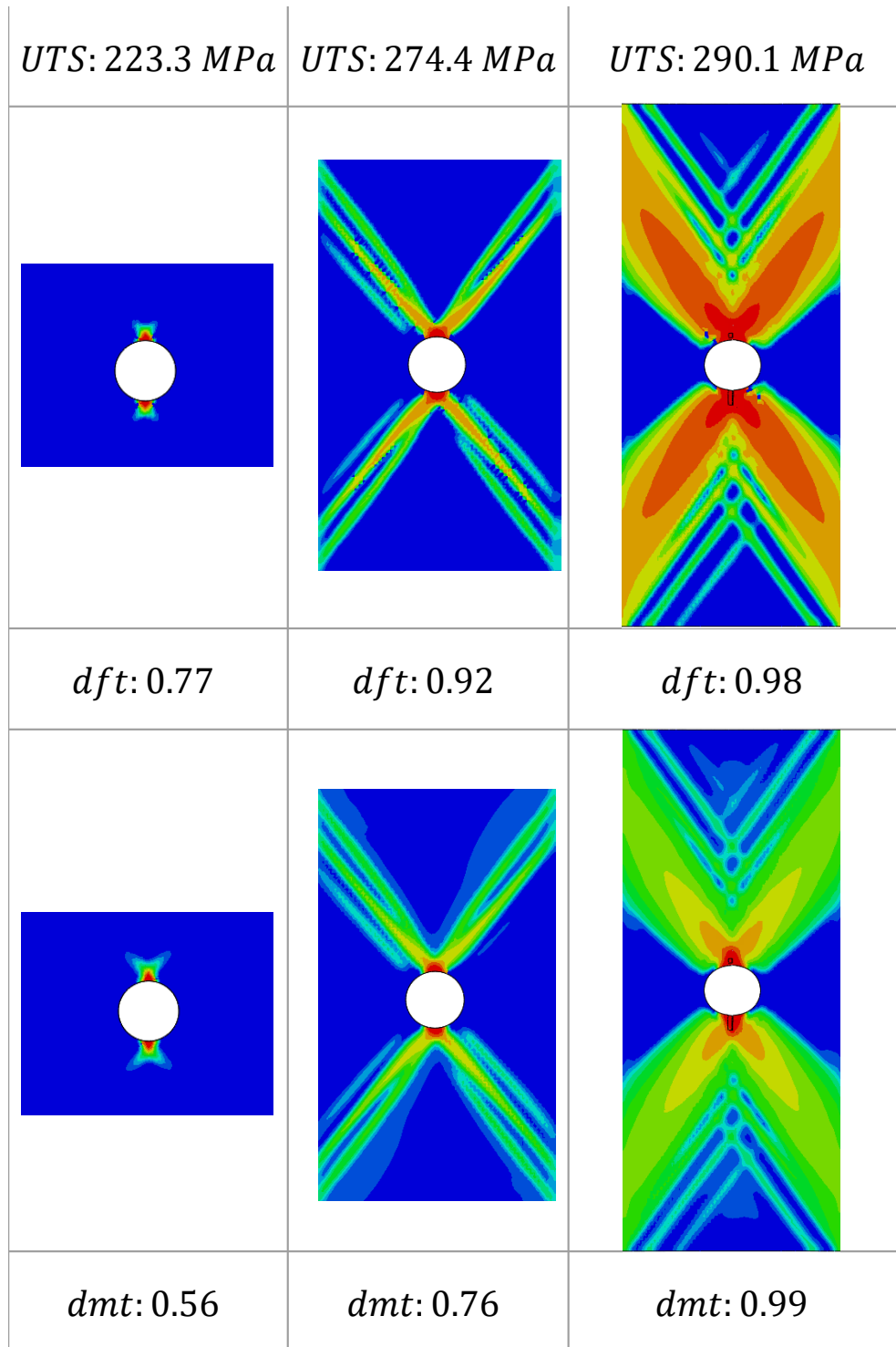
Figure 5.14: Damage propagation in the 45° glass fibre layers

dft: 0.98	dfm: 0.99
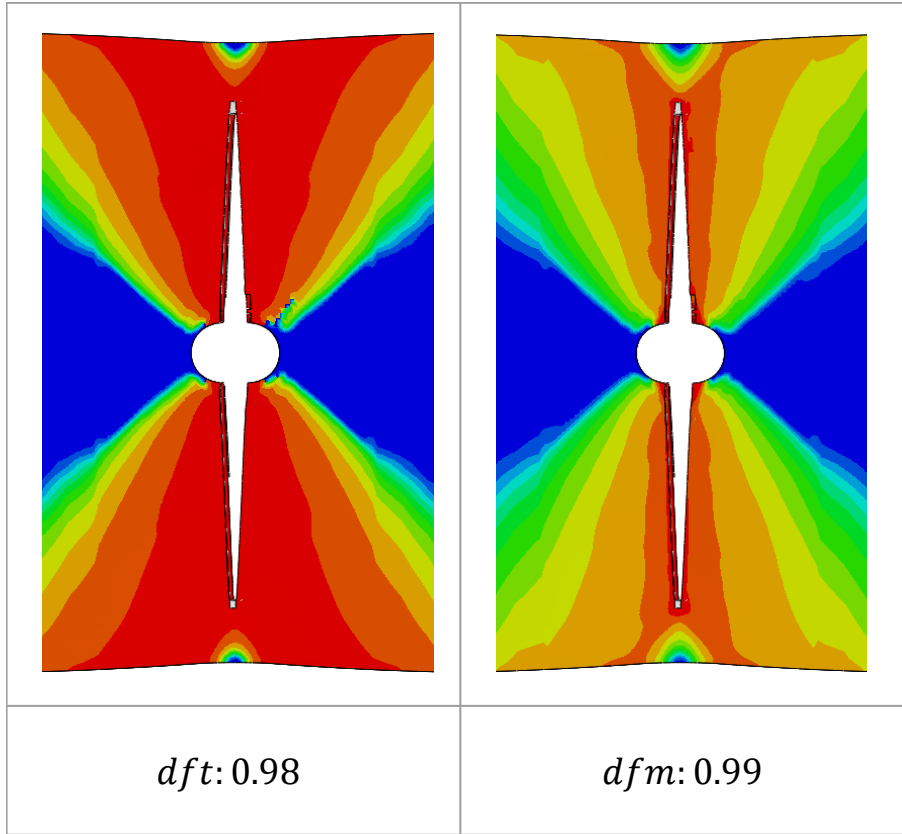
Figure 5.15: Final cracks in the 45° glass fibre layers

Progressive damage in aluminium layers

Damage initiation occurred within the aluminium layers during the elastic region prior to reaching the yield point of the specimen. The propagation of JCCRT was influenced by the orientation of the fiber angles, resulting in crack expansion at [±45°] as illustrated in Figure 5.16. When a UTS of 290.1 MPa is reached, the JCCRT is satisfied indicating full failure status in aluminium layers. Additionally, some elements were deleted at the notch of these layers at this stage.

Progressive damage at Al/glass fibre interface

The interface between the [±45°] glass fibre and aluminium layers exhibits signs of delamination, as depicted in Figure 5.17. During the elastic zone, the majority of debonding occurred around the notch, as observed in Figure 5.17 at UTS=222.3 MPa. With increasing load, stress rises along the direction of the fibres in the glass

$UTS: 223.3\ MPa$	$UTS: 274.4\ MPa$	$UTS: 290.1\ MPa$
$JCCRT: 0.071$	$JCCRT: 0.275$	$JCCRT: 1.0$
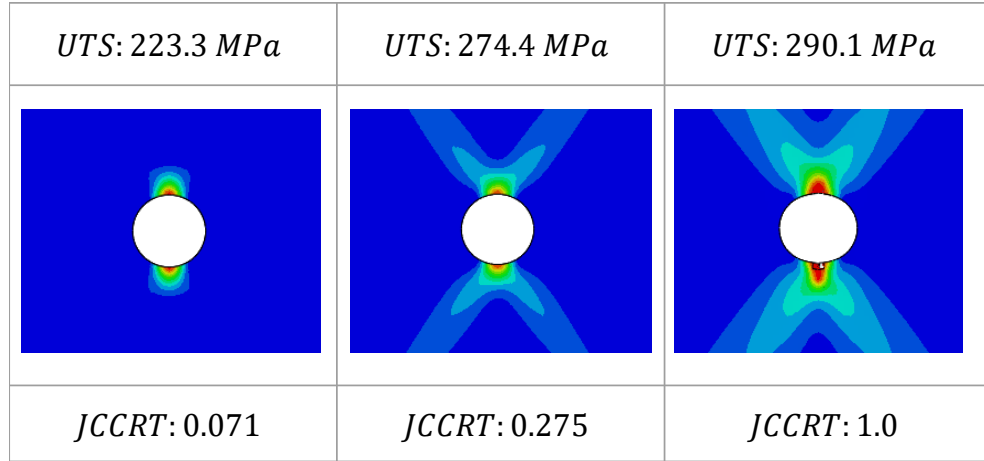
Figure 5.16: Damage propagation in aluminium layers in off-axis GLARE

fibre layers, as previously discussed. This discrepancy in stress levels between the glass fibre and aluminium layers leads to noticeable delamination along the fibres' direction, as clearly demonstrated in Figure 5.17 at UTS=274.4 MPa. The CSMAXSCRT attains its peak value once the first element is deleted near the notch, as illustrated at UTS=290.1 MPa.

$UTS: 223.3\ MPa$	$UTS: 274.4\ MPa$	$UTS: 290.1\ MPa$
$CSMAXSCRT: 0.08$	$CSMAXSCRT: 0.15$	$CSMAXSCRT: 0.57$
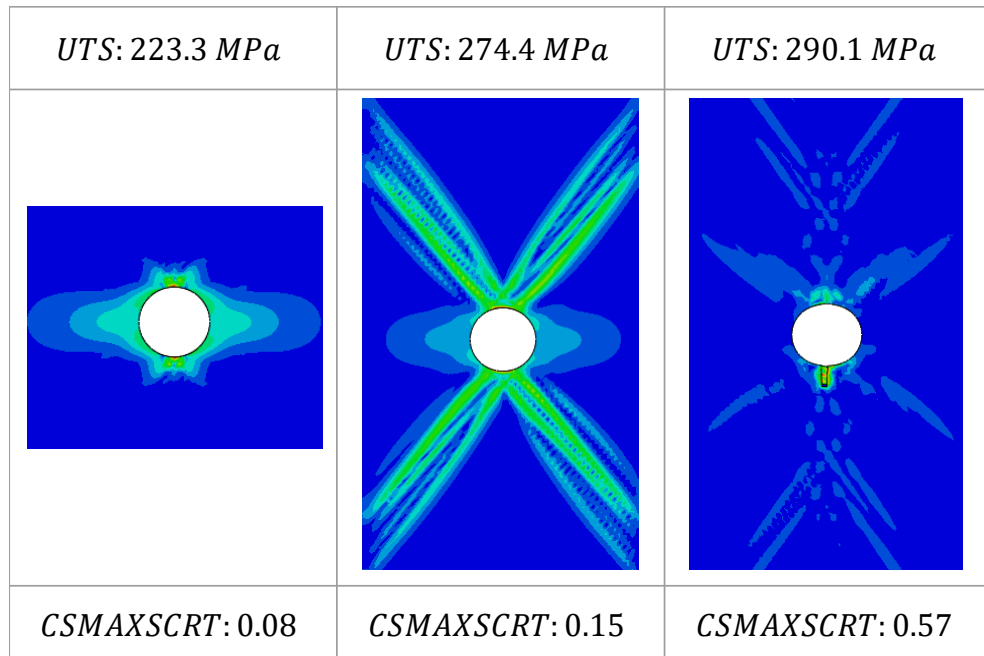
Figure 5.17: Damage initiation at Al/glass fibre interface in off-axis GLARE

5.7 Comparative analysis of the mechanical behaviour and failure Characteristics of on- and off-axis GLARE

As demonstrated in the previous sections, the fibre orientation angles have a significant influence on the mechanical response and failure mechanisms of GLARE. Beginning with the stress-strain curve, it was observed that the on-axis specimen exhibited a steeper elastic curve, with Young's modulus approximately 10% higher compared to the off-axis specimen. Additionally, the UTS was higher in the on-axis specimen, approximately 41% greater than in the off-axis specimen.

The stress concentration around the hole was influenced by the fibre angles in both specimens. Stress concentration is evident along fibre direction in the $(0°, +45°, -45°)$ layers as observed in Figures 5.6 and 5.13. In the case of aluminium layers, stress concentration in the on-axis case is less influenced by fibre angles as it still shows butterfly stress distribution in the contour plot. Conversely, the off-axis specimen shows specifically stress concentration at the off-axis fibre angles $[\pm45°]$.

Fibre and matrix tensile damage mechanisms were observed in glass fibre layers of both cases, as illustrated in Figures 5.7 and 5.9. The initiation of fibre breakage in the $0°$ glass fibre layers began at four points along the notch edge, while it started at two points (on top and bottom of the notch) for the $(\pm45°)$ layers. Fibre breakage propagated perpendicular to the loading direction in the $0°$ glass fibre layer, while it propagated along the $(\pm45°)$ direction for the respective layers. Regarding matrix tensile damage, in the on-axis specimen, matrix cracks initiated at the notch edge and propagated transversely to the loading direction in the $90°$ layers, and longitudinally in the $0°$ layers. Whereas in the off-axis case, the

propagation occurred along the fibre's direction. A common observation among all cases was that matrix cracks followed the direction of the fibre orientation angles, indicating the occurrence of micro-cracks between the fibre and matrix when subjected to loading.

In general, the mechanical behaviour of aluminium is characterised by its ductile nature, where aluminium exhibits significant plastic deformation prior to failure. In the on-axis specimen, the fracture of aluminium layers occurred suddenly, contrasting with its typical fracture behaviour. This abrupt fracture was attributed to the initiation of matrix cracks in the 90° glass fibre layer, resulting in weakened regions between the layers and shifting more stress onto the remaining intact layers On the other hand, in the off-axis specimen, the aluminium layers did not fracture despite the occurrence of matrix cracking and fibre breakage in the glass fibre layers. This is attributed to the fact that the tensile stress did not approach the tensile strength of aluminium T3-2024. Consequently, the layers continued to deform until the strain limit was reached, leading to gradual failure.

The failure behaviour of the on-axis specimen occurred suddenly, characterized by a rapid failure in a single increment. The final crack was clean and exhibited a perpendicular orientation to the loading direction across all layers within the FML, which indicates a brittle failure. On the other hand, the failure of the off-axis specimen occurred gradually over multiple increments. In the glass fibre layers, the crack exhibited a tilt towards the off-axis angles (±45°), which significantly influenced the final crack pattern of the specimen. Additionally, noticeable necking was observed at the edges of the off-axis specimen. These observations suggest a higher level of ductility in the off-axis specimen, highlighting the influence of fibre orientation on the mechanical properties and failure characteristics of FMLs.

In summary, this current chapter analysed the mechanical behaviour of FMLs in a notched structure and discussed the failure mechanisms that occurred during the tensile test. The combination of Hashin's and Puck's criteria in the currently developed VUMAT, along with the Johnson-cook and cohesive models, provided reliable and reasonable failure predictions for FML layers under applied tensile loading compared with approaches presented in the literature, while maintaining accurate results in comparison with experiments. Although this chapter focused on a tensile load case study for GLARE, the approach is applicable to a wide range of FML configurations and various mechanical tests.

Chapter 6

Investigating flexural loading-induced damage in CARALL

6.1 Introduction

This section aims to investigate the mechanical behaviour and failure mechanisms of FMLs under a three-point bending test. The selected FML referred to as CAR-ALL, consists of layers of carbon fibre and aluminium. During the three-point bending test, the FML experiences additional damage modes such as fibre and matrix compression, which were not observed in the tensile test. Similar to the preceding chapter, this chapter will introduce both on and off-axis FE models and the analysis will include mesh convergence and error analysis. Additionally, a comprehensive description and explanation of the mechanical behaviour, including the initiation and propagation of damage within the constituents of the FMLs, will be provided.

6.2   The FE model of 3-point bending test of CARALL

The 3-point bending is a mechanical test used for characterizing the flexural properties of materials i.e. flexural modulus and strength. According to the ASTM standard of the 3-point bending of polymer matrix composite materials (D7264) [5], the test is performed on a rectangular cross-sectional specimen resting on two supporting points while the load is applied at the centre of the specimen. A similar setup was utilized in the current simulation as illustrated in Figure 6.1.

In this investigation, a CARALL specimen consisting of three aluminium layers and two CFRP unidirectional laminates is considered. The thickness of each aluminium sheet and CFRP layer is 0.5mm. CFRP layers consist of laminates oriented at $[0°, 90°]s$ for the on-axis case and $[45°, -45°]s$ for the off-axis case as illustrated in Figure 6.1. The total length of the specimen is 80mm, with a width of 10mm and a total thickness of 2.5mm. The loading and support noses have a 10mm diameter, while the distance between the two supports is 50 mm as shown in Figure 6.1.

In the FE model all degrees of freedom are fixed for the supports and a vertical displacement of 20mm is applied at the loading nose. A general contact behaviour was defined between the noses and specimen with a friction coefficient equal to 1.0 [21]. In addition, a cohesive interaction was defined at the interface between the CFRP and Aluminium. While a fully bonded interface is assumed between the CFRP layers. The time step for the simulation was set to 0.02 seconds, and it was run on a computer equipped with processor having 8 cores, 16 threads and 2.90 GHz.
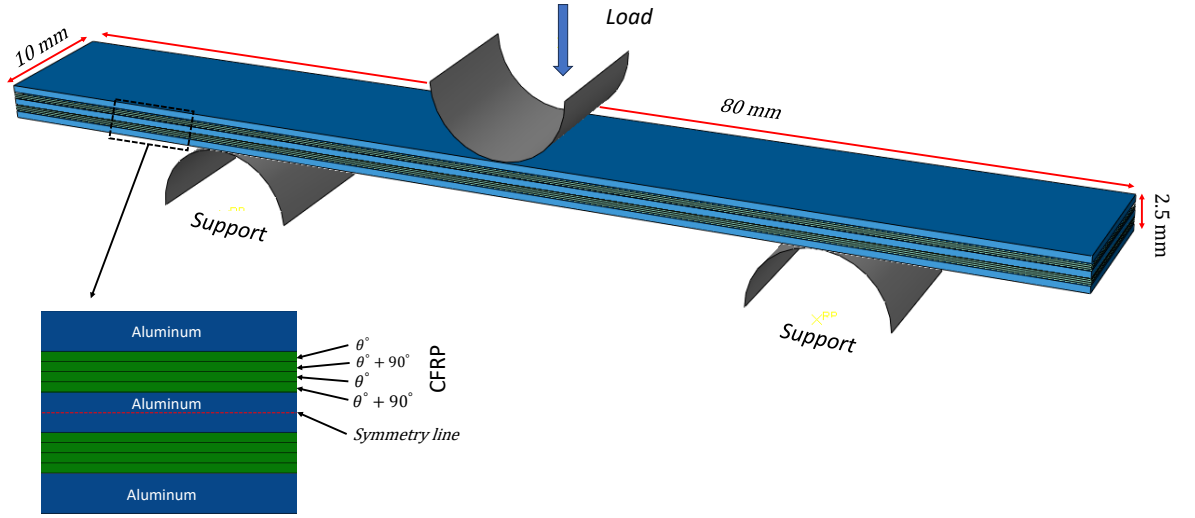
Figure 6.1: Geometry of 3-Point bending specimen and cross-sectional view

The FML includes 3 aluminium sheets and 8 carbon fibre plies, this might propose complexity in defining the layers for the progressive damage analysis. Therefore, a new system has been proposed to define a unique number for each individual layer. The names of the layers are defined in Figure 6.2 for both the on and off axis cases. The aluminium layers are named as (Al_n), where the subscript (n) indicates the location of the layer in the laminate, with number 1 in the top (under the loading nose), 2 in the middle and 3 at the bottom of the FML. Whereas for carbon fibre laminates the layer name will be in the form $(CF_{xy}, \theta°)$, where $(\theta°)$ is the orientation of the fibre angles. Whereas the subscript (x) represents the location of laminate, with $x = 1$ denoting the top laminate and $x = 2$ for the bottom laminate. The subscript (y) indicates the individual ply order within the laminate, ranging from 1 for top ply to 4 for bottom ply.

(a) On-axis CARALL   (b) Off-axis CARALL

Figure 6.2: Unique layer labelling in (a) on-axis and (b) off-axis CARALL specimens

6.3   Material properties

The aluminium sheets were assumed to exhibit elastic-plastic behaviour of 2024-T3, and the properties listed in Tables 5.2 were assigned to these layers. While it was assumed that the behaviour of CFRP layers was transversely isotropic with the elastic and strength values listed in Tables 6.1 and 6.2 respectively. Additionally, Table 6.3 outlines the fracture energies of CFRP in four modes.

The failure of aluminium layers was defined with the Johnson-Cook failure criterion, with parameters outlined in Table 5.3. While the failure of the carbon fibre layers relied on the VUMAT code developed within the current study. The interface between the aluminium and carbon fibre layers was characterized using a cohesive-surface model, incorporating a traction-separation model for the definition of its behaviour. The failure assessment of the cohesive model was conducted based on the maximum stress criterion, where the parameters of these models are provided in Table 5.1.

Table 6.1: Orthotropic elastic properties of carbon fibre [104]

E_1(GPa)	E_2, E_3(GPa)	G_{12}, G_{13}(GPa)	G_{23}(GPa)	ν_{12}, ν_{13}
108	8.0	4.0	3.0	0.32

Table 6.2: Orthotropic strength of carbon fibre [104]

X^T(MPa)	X^C(MPa)	Y^T(MPa)	Y^C(MPa)	S^L(MPa)
2100	800	25	120	80

Table 6.3: Fracture energies of carbon fibre prepreg [81]

G_{ft}(N/mm)	G_{fc}(N/mm)	G_{mt}(N/mm)	G_{mc}(N/mm)
81.5	106.3	0.2774	1.3092

6.4   Mesh sensitivity analysis

CARALL layers were assigned the 3D 8-node continuum linear hexahedral elements with reduced integration (C3D8R). This element type comprises 8 nodes located at the corners of the element and a single integration point at the middle of the element. It's worth mentioning that these elements significantly reduce the computational cost of the model compared to full integration elements, primarily because they utilize fewer integration points. However, when linear elements are used with reduced integration, they may encounter accuracy issues due to a phenomenon known as "hourglassing" [86]. Hourglassing occur in these elements when they are subjected to bending load as they include only one integration point at the middle of the element. This results in zero stress at the integration point, making the element unable to resist such deformation. This could result in producing meaningless results if a coarse mesh is used [86]. In order to overcome this issue, a reasonably refined mesh strategy is used in the simulation. In addition, the pure stiffness form of hourglass control is enabled in order to minimize hourglassing effect, as recommended by Abaqus for quasi-static problems in the Explicit solver [86].

Table 6.4: Element sizes for each model (Number of elements): In-plane (a, b) and through-thickness (c, c1) dimensions for CARALL layers

Number of elements	Element size (mm)				Aspect
	a	b	c	c1	ratio
11680	1	1	0.125	0.25	8
31280	0.5	0.5	0.125	0.25	4
59280	0.33	0.33	0.125	0.25	2.64
71880	0.33	0.33	0.125	0.1667	2.64
116080	0.25	0.25	0.125	0.1667	2
170480	0.2	0.2	0.125	0.1667	1.6

The mesh refinement is implemented in the central region where failure is expected to occur. The mesh sensitivity study and error measurement are conducted on the on-axis specimen and were plotted against the total number of elements in the model as shown in Figure 6.3. The error was calculated by comparing the force at failure with experimental values for a similar test [104], using Equation 5.1. The dimensions of the elements in the mesh sensitivity study are listed in Table 6.4 for each refinement increment. The in-plane dimensions are denoted by (a & b), while the through-thickness dimensions for carbon fibre and aluminium layers are represented by (c & c1) respectively. Additionally, the table includes the aspect ratios for the smallest element in the model, aiming to achieve 1.0. However, due to the small thickness of carbon fibre layers achieving this value was challenging. Nevertheless, a value of 1.6 was reached for the most refined model.

The mesh refinement strategy began with ($1mm \times 1mm$) for the in-plane dimensions, with one element allocated for carbon fibre layers and two elements for the aluminium layers through their thicknesses. This resulted in an approximately 0.22 error when compared to experimental data, and a relatively high aspect ra-

tio, reaching 8.0. The simulation of this model required 2.8 hours to complete. Further refinement was then implemented by reducing the in-plane dimensions to 0.5mm and then 0.33mm, which decreased the error to 0.13. The next refinement was achieved by increasing the thickness of the aluminium layers to 3, resulting in an error of 0.12. To further enhance the accuracy, a final refinement was made on the in-plane direction, reducing the size to 0.2mm. This reduced the error to 0.11 and resulted in an aspect ratio of 1.6mm, as highlighted in Table 6.4 and Figure 6.3. This model, which contains the largest number of elements (170480), required the highest computational time of approximately 41 hours. The mesh convergence was achieved at the model containing (116080) elements, demonstrating an approximate error of 0.11. The elements in this model have an in-plane element size of $(0.25mm)$, while the carbon fibre and aluminium layers have element thicknesses of 0.125mm and 0.1667mm respectively. Therefore, this model is used for both models.
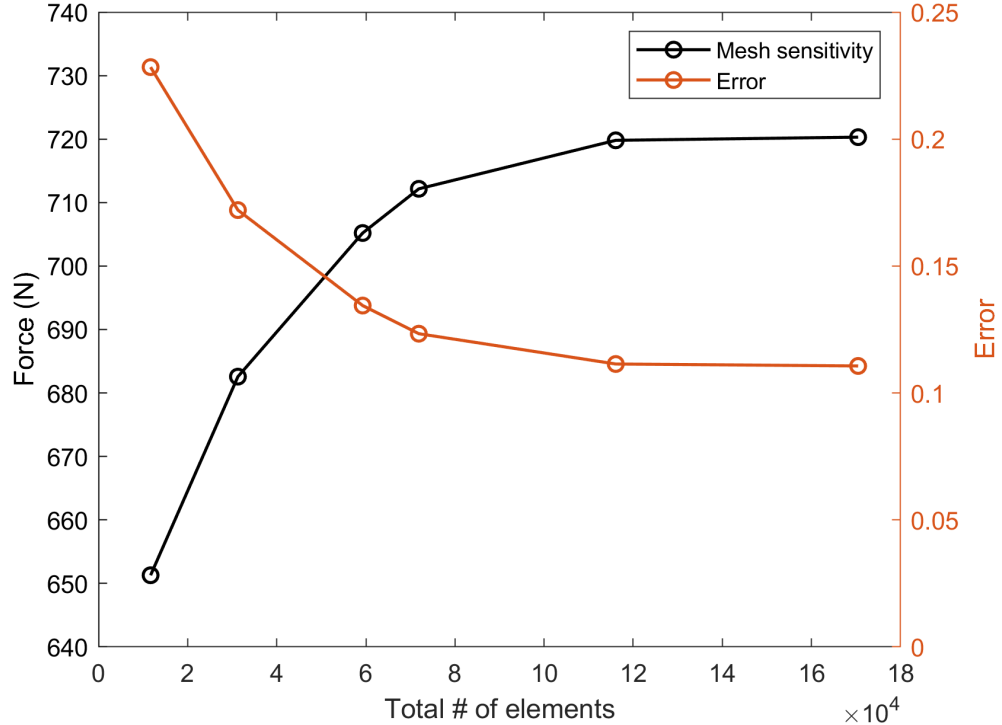
Figure 6.3: Ultimate tensile strength and corresponding error vs. number of elements for on-axis CARALL

6.5   Results and discussion of on-axis CARALL

6.5.1   The mechanical behaviour of on-axis CARALL under flexural loading

The mechanical behaviour of CARALL under 3-point bending is examined by analysing the Force vs. Displacement curve illustrated in Figure 6.4. This curve illustrates a linear elastic region denoted by (point-A), followed by a non-linear curve that initiates at (point-B) and progresses to failure at (point-C), which shows a sudden drop in force. Subsequently, two points (D and E) were defined at two descending stages, representing the damage propagation in the specimen. It is worth mentioning that similar descending stages were noted in the experimental observations conducted by [55].

The flexural modulus (E_f) is determined as 49.1 GPa using Equation 6.1 and the maximum flexural stress (σ_f) was calculated as 841.2 MPa using equation 6.2. In these equations, P represents the maximum applied force, b and h denote the width and thickness of the specimen, L represents the support span, and m indicates the slope of the secant of the initial force-deflection curve [5].

$$E_f = \frac{L^3 m}{4bh^3} \tag{6.1}$$

$$\sigma_f = \frac{3PL}{2bh^2} \tag{6.2}$$
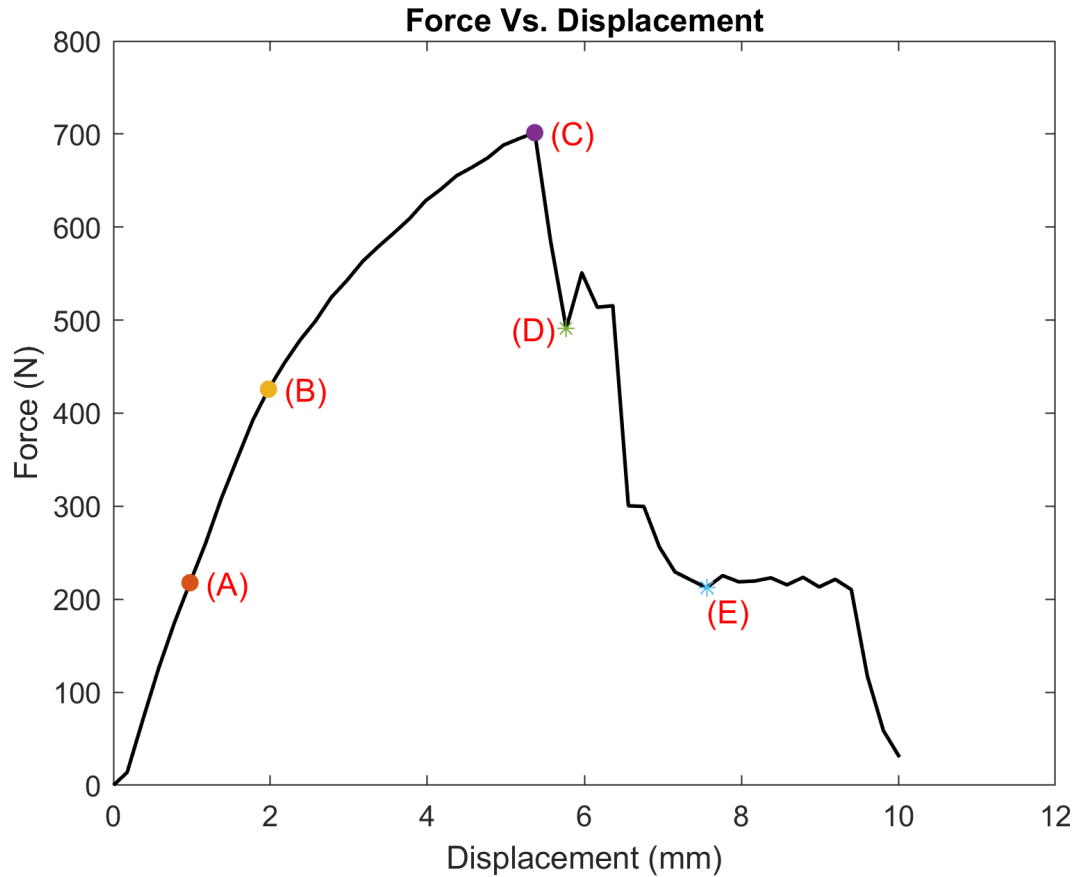
Figure 6.4: flexural loading response: Force vs. Displacement curve of on-axis CARALL specimen

The contour plot of Von-Mises stress is illustrated in Figure 6.5 displaying the five stages highlighted in the Force-Displacement curve. Initially, at point-A, the stress is concentrated at the top and bottom aluminium layers, representing the highest compressive and tensile stress, respectively. At this stage the Von-Mises stress measures 310 MPa at the top and bottom layers. Notably, the middle aluminium layer (Al_2), shows the least amount of stress as it is positioned at the neutral axis.

Once the load exceeds the yield point of aluminium, denoted as stage-A, the aluminium layers undergo plastic deformation. In this state, aluminium becomes less sensitive to load, indicating that as deformation progresses, stress does not increase as it did within the elastic region. In contrast, carbon fibre exhibits a

linear elastic behaviour, maintaining a constant sensitivity to load. Thus, the stress-bearing capacity of aluminium decreases in comparison to carbon fibre. This is clearly shown in Stage-B of Figure 6.5, where stress concentration mainly occurs at the topmost and bottommost carbon fibre layers, identified as $(CF_{11}, 0°)$ and $(CF_{24}, 0°)$, respectively. Here, the Von-Mises stress approximates 750 MPa.

Following stage-B, the specimen exhibits a non-linear behaviour until reaching the ultimate flexural strength. Therefore, at point-C the maximum stress is recorded as $1.9 * 10^3 MPa$ in the bottommost carbon fibre layer $(CF_{24}, 0°)$. This layer bears the majority of the load, as indicated in Figure 6.5 at stage-C, because its fibres are oriented at $(0°)$ from the horizontal and its position being the farthest from the neutral axis, indicating tension loading. It is worth mentioning that the $(CF_{11}, 0°)$ layer, which initially carried nearly an equal load to the $(CF_{24}, 0°)$, only shows a stress of 750 MPa at stage-C. This is attributed to the compressive forces exerted on this layer. Indeed, carbon fibre demonstrates more than double the strength in tension compared to compression.

After stage-C, the specimen starts to lose its load-bearing capacity, and a sudden drop in force is observed in the force vs displacement curve (Figure 6.4). Stages (D and E) illustrate the stress levels following this drop. In reality, the end of stage-C represents the initiation of failure propagation and the onset of some failure modes, which will be discussed in the following sections. In addition, element deletion was observed in the $(90°)$ carbon fibre layers in stage-D, this was the starting point for crack propagation in the adjacent layers as shown in stage-E. During stage-E, cracks developed in the bottom aluminium and carbon fibre layers, transferring stress to the remaining intact layers.
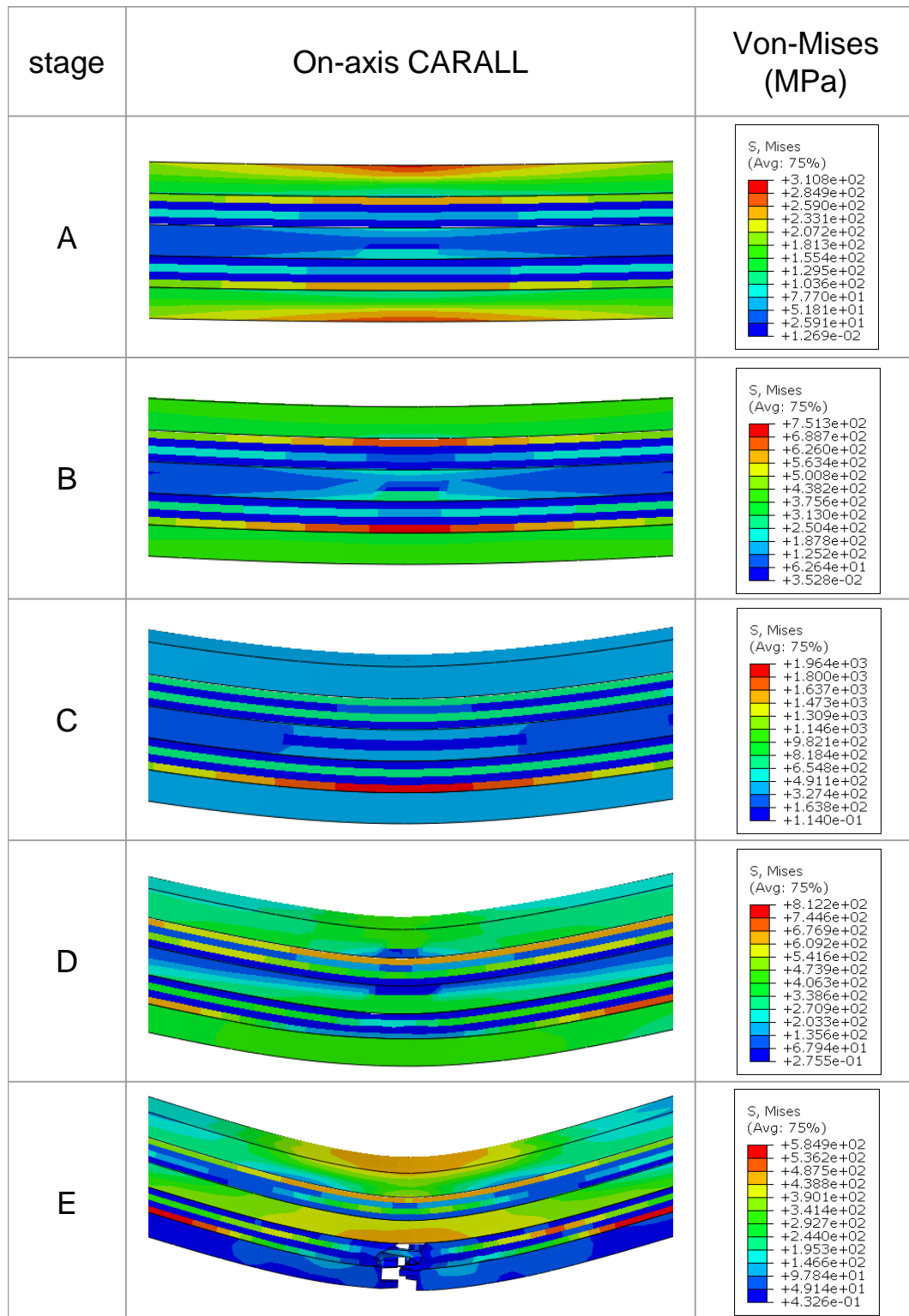
Figure 6.5: Von Mises stress in CARALL specimen: Side view across five stages

6.5.2   Damage modes and failure sequence in on-axis CAR-ALL

Progressive damage in carbon fibre layers

The initial failure mode observed in the 3-point bending test of on-axis CARALL involves matrix tensile damage within the carbon fibre laminate located under the neutral axis, specifically in $(CF_{23}, 90°)$ as shown in Figure 6.6. Matrix tensile damage started approximately when the force-displacement curve changed from linear to non-linear behaviour. This was evident at the edges of the specimen as illustrated in Figure 6.6 at 425.7 N. Matrix cracks then propagated across this layer, reaching a value of 0.66 prior to full failure. At the instant of passing the maximum load in the F vs D curve (point-D), matrix cracks propagated to the full width of the layer, with the value of (d_{mt}) approaching 0.99. At this point, some elements were deleted from the middle of the layer.

	load: 425.7 N	load: 687.9 N	load: 491.0 N
Side view			
d_{mt} at $(CF_{23}, 90°)$	$d_{mt} = 0.13$	$d_{mt} = 0.66$	$d_{mt} = 0.99$
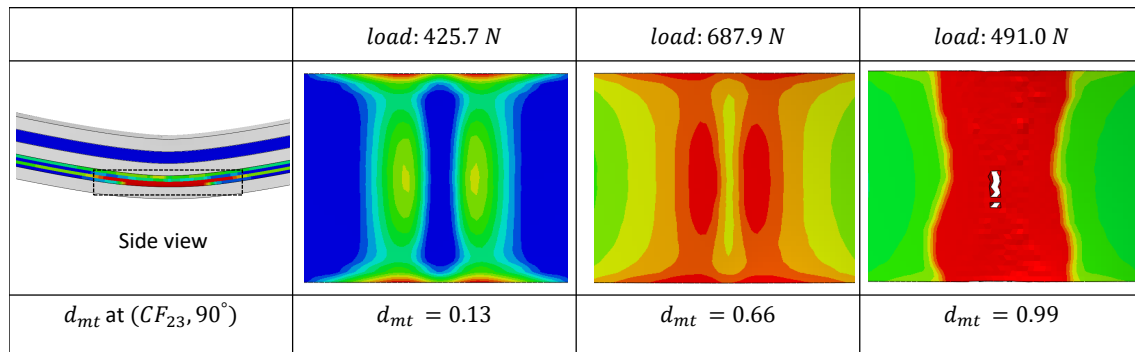
Figure 6.6: Matrix tensile damage (d_{mt}) at bottom carbon fibre layer across various load levels

The second observed failure mode was fibre tensile damage (d_{ft}) illustrated in Figure 6.7. This failure mode is initiated in the lowest carbon fibre layer oriented at $(0°)$, specifically $(CF_{24}, 0°)$. This can be attributed to the high tensile stress experienced in this layer, as it is located at the bottom of the specimen. The initiation of (d_{ft}) occurred as a vertical crack in the middle of the layer almost at a load of 687.3N. The crack then propagated across the layer, reaching a value of

0.65 prior to full failure. Fibre breakage was achieved once (d_{ft}) approached 0.99 at the moment of full failure, at this point evident element deletion was observed as shown in Figure 6.7 at 515.5N.

	load: 687.3 N	*load: 701.5 N*	*load: 515.5 N*
Side view			
d_{ft} at $(CF_{24}, 0°)$	$d_{ft} = 0.198$	$d_{ft} = 0.650$	$d_{ft} = 0.985$
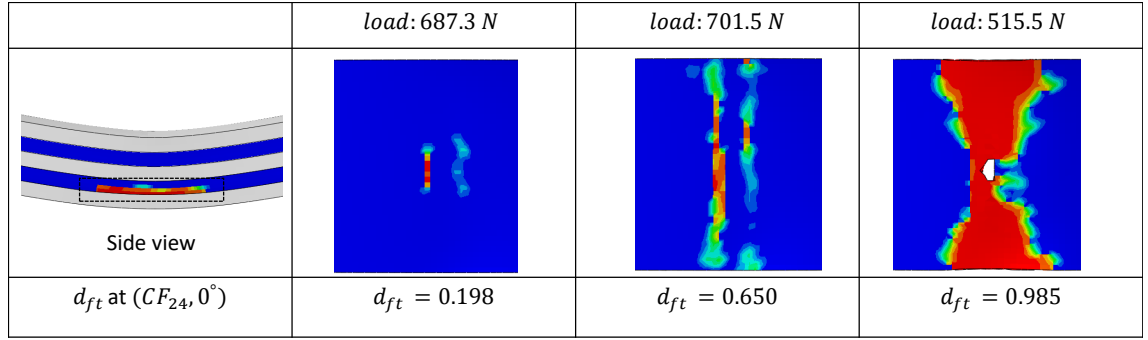
Figure 6.7: Fibre tensile damage (d_{ft}) at bottom carbon fibre layer across various load levels

Two primary failure modes were observed in the carbon fibre layers located above the neutral axis, namely fibre compression damage (d_{fc}) and matrix compression damage (d_{mc}). This was expected since the laminate was exposed to compressive stress. The two failure modes are shown in Figures 6.8 and 6.9 respectively. Fibre compression damage caused fibre kinking in the $(CF_{11}, 0°)$ layer, resulting in a single crack shown in Figure 6.8 at 687.3N. As the load increases, multiple cracks propagate across the layer's width, until (d_{fc}) reaches a maximum value of 0.97. Matrix compression damage caused matrix cracking in the $(CF_{12}, 0°)$ layer as an elliptical pattern shown in Figure 6.9 at 688N. As the load increases, a vertical crack appears with (d_{mc}) reaching 0.99. This is attributed to the buckling that occurred in this layer.

	load: 687.3 N	load: 628.1 N	load: 515.5 N
Side view			
d_{fc} at $(CF_{11}, 0°)$	$d_{fc} = 0.51$	$d_{fc} = 0.83$	$d_{fc} = 0.97$
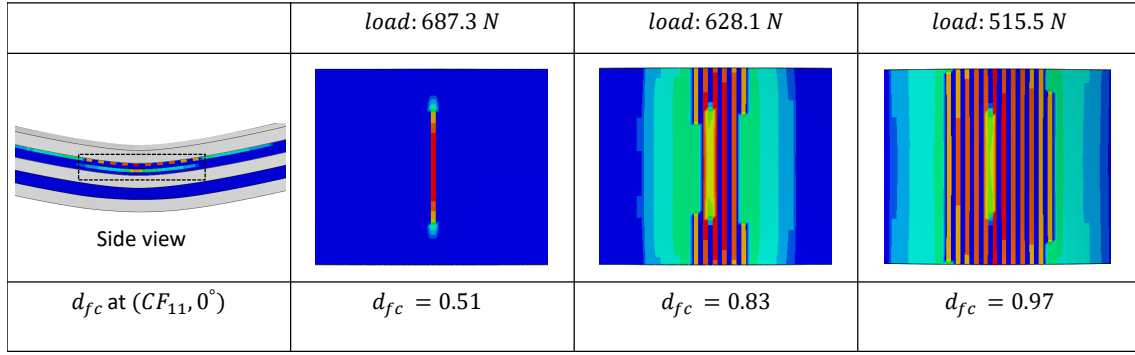
Figure 6.8: Fibre compressive damage (d_{fc}) at upper carbon fibre layer across various load levels

	load: 688 N	load: 701.5 N	load: 585.3 N
Side view			
d_{mc} at $(CF_{12}, 90°)$	$d_{mc} = 0.13$	$d_{mc} = 0.24$	$d_{mc} = 0.99$
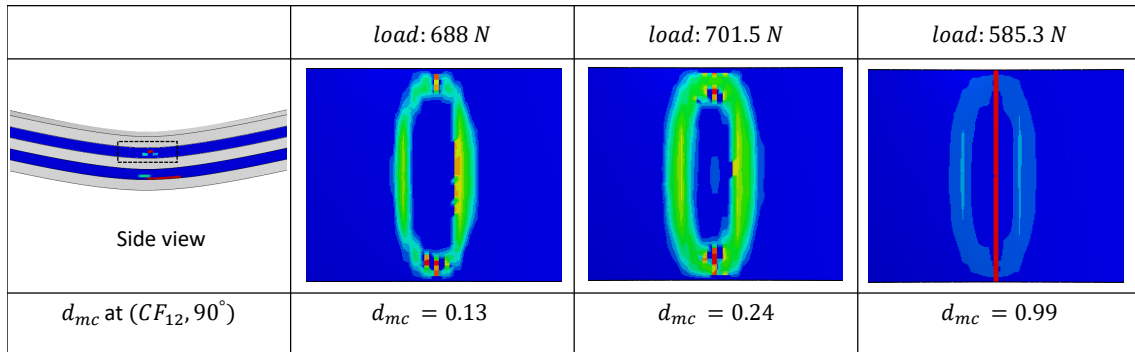
Figure 6.9: Matrix compressive damage (d_{mc}) at top carbon fibre layer across various load levels

Progressive damage in aluminium layers

The aluminium layers in the CRALL specimen experienced plastic damage due to the applied bending load. The plastic damage is analysed using the JCCRT criteria on the three aluminium layers, as shown in Figure 6.10. As the test progressed and the elastic behaviour transitioned to non-linear behaviour, evident plastic damage occurred in the top and bottom aluminium layers, Al_1 and Al_3 respectively, as illustrated in Figure 6.10. This can be attributed to the tensile stress in Al_3 and compressive stress Al_1. Meanwhile, the middle aluminium layer, Al_2, did not show any plastic damage until the specimen transitioned beyond the elastic region (point-B). This was expected since this layer is located at the neutral axis, resulting in a lower stress level compared to other layers.

Upon approaching 640.8 N, noticeable plastic damage became evident in Al_3, with $JCCRT$ being 0.17. Notably, Al_1 still shows a higher level of damage compared to Al_2 at this stage, as illustrated in Figure 6.10. Further loading increased the plastic damage in all layers, with Al_3 experiencing the most significant plastic damage, approaching 1.0. Al_3 reached a fully failed state at the centre of the layer following the initial drop in force observed in the force-displacement curve, which occurred at approximately at 515.5 N. At this stage, the plastic damage in Al_2 exceeded that in Al_1, This can be attributed to the displacement of Al_2 from the neutral axis, leading to increased exposure to deformation. Moreover, Al_2 is the most bottom intact layer at this stage, bearing most of the tensile load.

At a load of 117.4 N, the elements positioned at the centre of Al_3 were deleted, resulting in the formation of a crack across this layer, as illustrated in Figure 6.10 at 117.4 N. Indeed, this crack gradually propagated within Al_3 following the appearance of a similar crack within the carbon fibre laminate. At this stage, plastic damage attained a value of 1.0 in Al_2, as it was the only intact layer situated at the bottom of the specimen.

	Load: 640.8 *N*	*Load*: 515.5 *N*	*Load*: 117.4 *N*
Al-1	max: 0.09	max: 0.23	max: 0.34
Al-2	max: 0.049	max: 0.29	max: 1.0
Al-3	max: 0.17	max: 1.0	max: 1.0
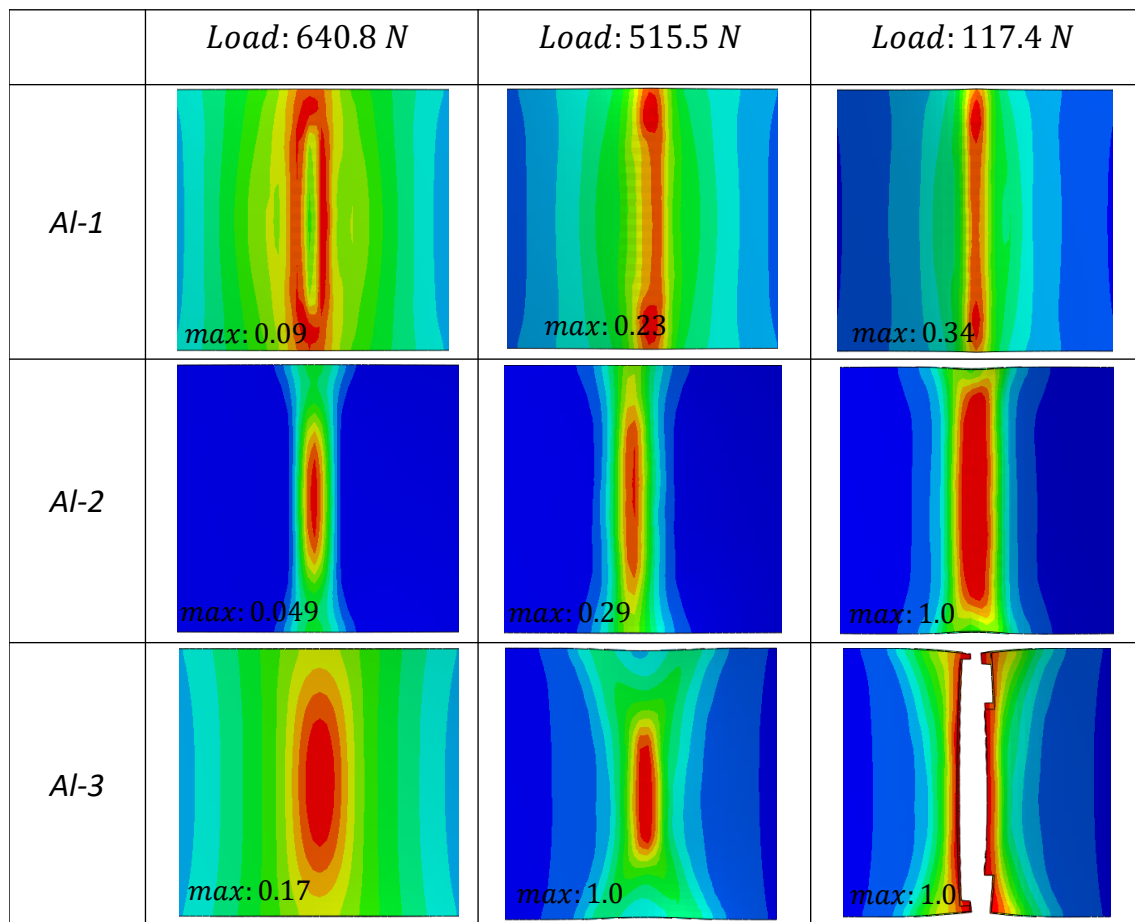
Figure 6.10: Johnson-cook damage (JCCRT) across three aluminium layers at various load levels

Progressive damage of Al/carbon fibre interface

The separation of layers was mostly noticeable at the interface between the intermediate aluminium (Al-2) and the lower CFRP laminate. The contact stress damage initiation variable (CSMAXSCRT) is plotted in Figure 6.11 at the Al-2 and $(CF_{21}, 90°)$ interface both before and after failure. This plot represents the distribution of delamination across the interface. On the left side of Figure 6.11, the delamination is shown prior to the initial drop in force observed in the force-displacement curve. This indicates a maximum value of 0.78 at the edges of the specimen, whereas a considerably lower value is observed in the central area of the specimen. At the moment of crack propagation in the lower CFRP laminate, a significant increase in delamination occurred at the centre of the specimen as shown on the right side of Figure 6.11. These predictions were consistent with experimental observation conducted by [55]
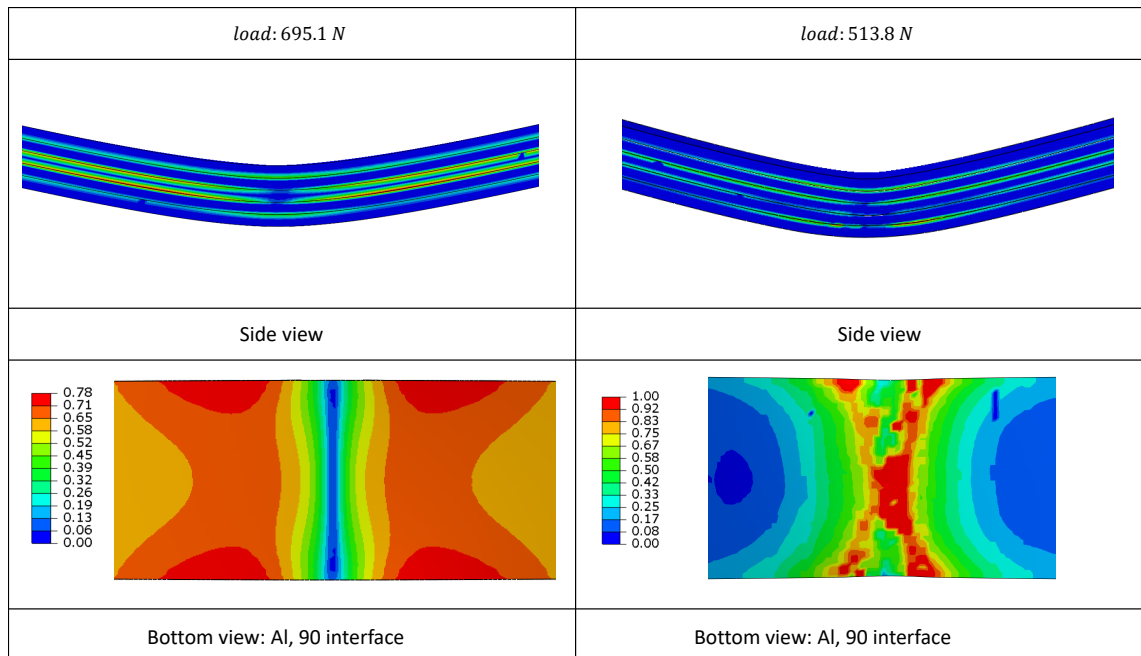
Figure 6.11: Damage initiation at Al/carbon fibre interfaces in on-axis CARALL

6.6   Results and discussion of off-axis specimen

6.6.1   The mechanical behaviour of off-axis CARALL under flexural loading

The flexural loading response of off-axis CARALL is categorized by the force vs. displacement curve illustrated in Figure 6.12. The curve can be divided into several regions, starting with a linear elastic region denoted with point-A, following a nonlinear curve at point-B which progresses until the maximum point, C, where the force drops due to failure. The force then gradually decreases until it reaches a sharp drop denoted by point-D. The flexural modulus (E_f) is determined as 36.7 GPa using Equation 6.1 and the maximum flexural stress (σ_f) was calculated as 640.44 MPa using equation 6.2.
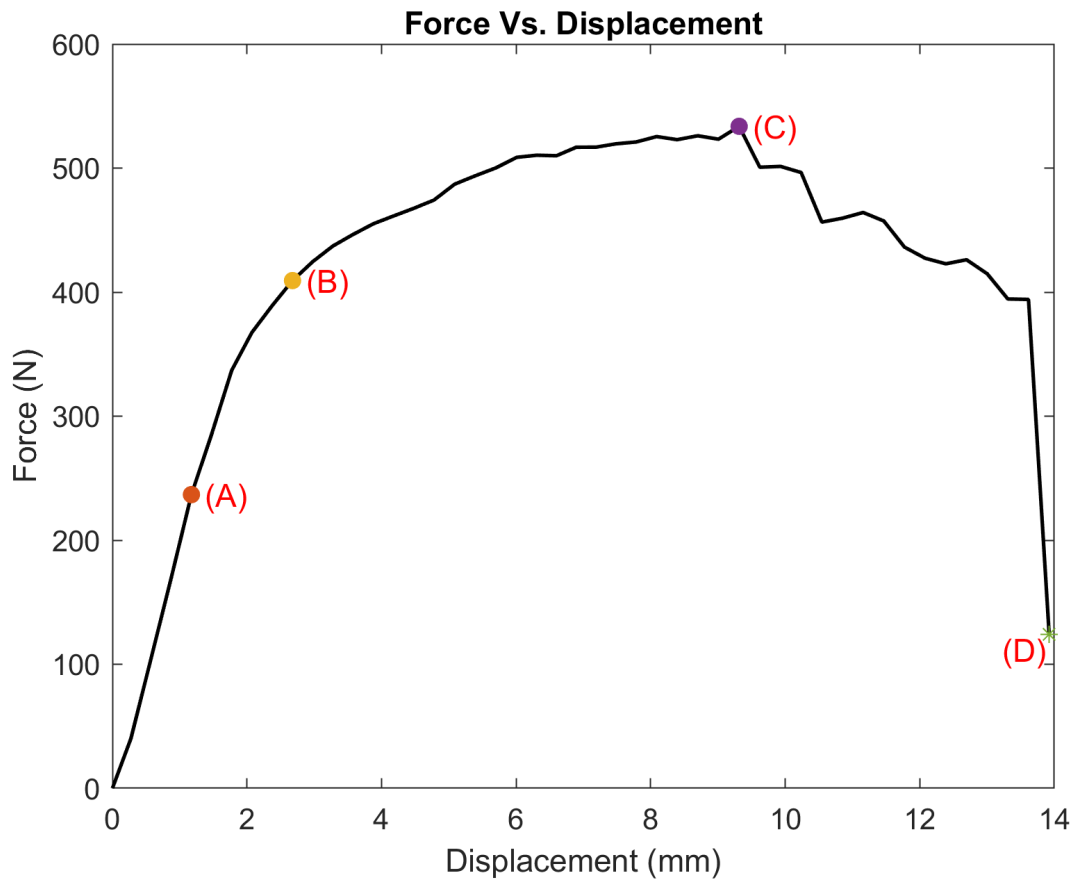
Figure 6.12: Flexural loading response: Force vs. Displacement curve of off- axis CARALL specimen

The Von-Mises stress is plotted for the off-axis CARALL layers, in Figure 6.13, at the four stages displayed in the Force vs. Displacement curve. The figure shows the Von-Mises stress state from a side view of the specimen, with a top view of the layer with the most critical stress at a certain stage. Initially, the stress was concentrated at the topmost and bottommost layers, specifically at Al_1 and Al_3, as these layers are exposed to the highest compressive and tensile loads respectively. During this stage, stage-A, the stress measures 3.52e2 MPa, with the peak stress accumulated in the central regions of Al-1 and Al-3. Notably, at this stage the stress values were minimal at carbon fibre laminates, also the middle aluminium layer did not show critical stress values as it is positioned at the neutral axis.

Following the yield point of CARALL, stress continues to concentrate at Al-1 and Al-3. However, the uppermost and lowermost carbon fibre layer ($CF_{11}, 45°$) and ($CF_{24}, 45°$) respectively, experience a higher level of stress, as shown in Figure 6.13, stage-B. This stress concentrates in the middle of these layers, corresponding to the load applied area. After stage-B has ended the aluminium layers became less sensitive to load as aluminium plastically deformed. In contrast, carbon fibre continues to resist load at a constant rate as it exhibits linear elastic behaviour. Hence, carbon fibre layers bear a higher load until reaching the peak point (Point-C) in the force vs. displacement curve.

Additionally, following stage-B, a significant shift has occurred in the concentration of stress within the carbon fibre layers. The stress translated from an elliptical stress distribution to lines oriented at 45 degrees within the bottommost carbon fibre layer, shown in Figure 6.13, stage-C. This shift is attributed to the fibres oriented at 45 degrees in this layer, which are resisting the tensile load. On the other hand, the topmost carbon fibre layer is exposed to a high

compressive load by the loading nose, leading to high stress concentration at the loading area, as highlighted in stage-C of Figure 6.10

The specimen started to lose its load bearing capacity following the completion of stage-C, as evidenced by the gradual decrease in force in Figure 6.12. This indicates that failure modes have approached critical values by this stage. Upon approaching the final stage (stage-D), both Al-3 and CF-2 lost their ability to bear the load and cracks started to propagate in these layers.
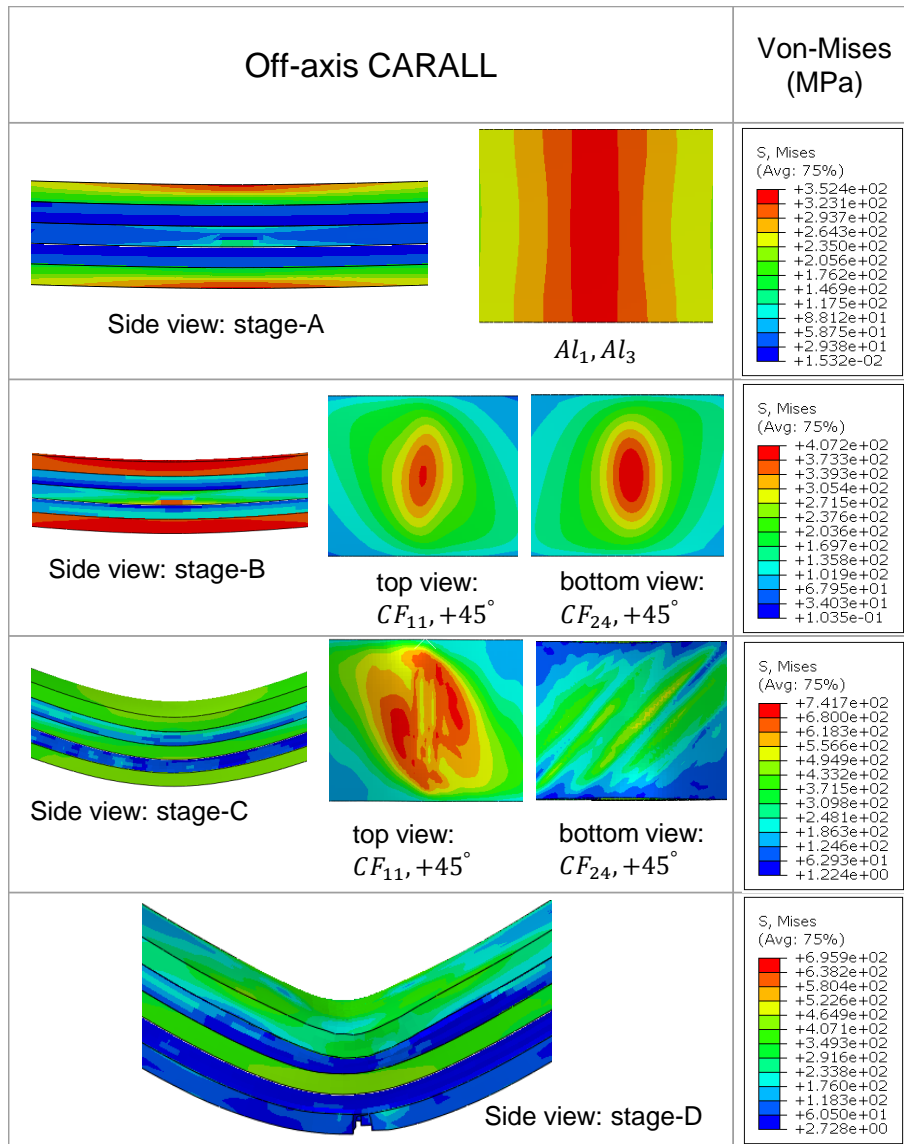

Figure 6.13: Von Mises stress in off-axis CARALL specimen across four stages

6.6.2   Damage modes and failure sequence in off-axis CAR-ALL

Progressive damage in carbon fibre layers

The first observed damage mode in the off-axis CARALL flexural test was matrix cracking within the lower carbon fibre laminate, specifically in the $(CF_{24}, 45°)$. The initiation and propagation of matrix tensile damage (d_{mt}) is illustrated in Figure 6.14 across various load levels in the force vs. displacement curve. Matrix cracking initiated at an early stage and concentrated in the central regions of $(CF_{24}, 45°)$, this concentration of damage expanded in an elliptical pattern at a load of 424.5 N. The occurrence of this damage is attributed to the high tensile stress in this layer due to the load applied by the nose. This followed cracks propagating from the specimen edges parallel to the fibres angle orientation $(\pm45°)$ in the four layers of (CF_2), as shown in Figure 6.14 at 510.4 N. In addition, some matrix cracks were observed in the top carbon fibre laminate (CF_1). The inclination in matrix cracks is is influenced by the fiber orientation at $(\pm45°)$, where matrix cracks expanded at matrix-dominated regions. A similar observation was made by Lu Yao et al. [104] for a similar FML under bending load. Additionally, the cracks occurred in two directions at the bottom of the specimen due the fully bonded laminae that in the model and the symmetric configuration of the laminate. At the final stage, elements were deleted from the $(CF_{24}, 45°)$ laminate during the final drop in force (stage-D).

The lower carbon fibre laminate (CF_2) also experienced fibre breakage, as evidenced by the fibre tensile damage (d_{ft}) illustrated in Figure 6.15. The initiation of (d_{ft}) started at 446.5 N due to the applied load. As the load continued to increase, cracks initiated at the fibre angle orientations, as shown in Figure 6.15 at 525.4 N. This damage mode was mainly observed in this laminate due to the

tensile stress that it experiences. Once the cracks increased to a certain level, (d_{ft} approached its critical value, leading to element deletion from the central area of the laminate.

	load: 424.5 N	load: 510.4 N	load: 124.1 N
Side view			
Matrix tension (d_{mt})	$d_{mt} = 0.4578$	$d_{mt} = 0.99$	$d_{mt} = 0.99$
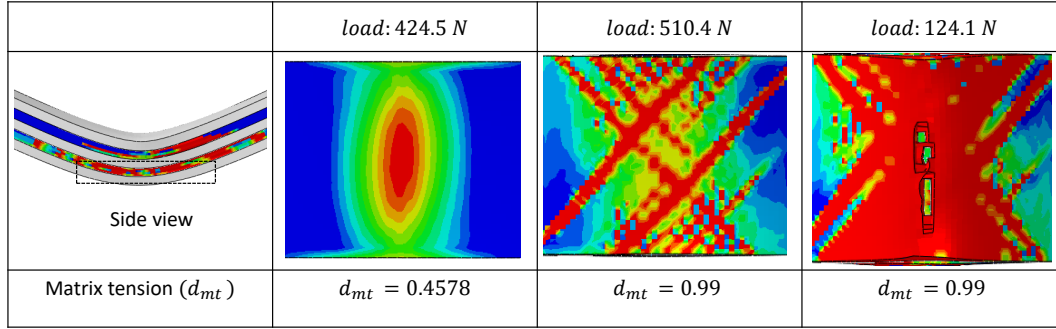
Figure 6.14: Matrix tensile damage (d_{mt}) at off-axis CARALL across various load levels

	load: 446.5 N	load: 525.4 N	load: 124.1 N
Side view			
Fibre tension (d_{ft})	$d_{ft} = 0.64$	$d_{ft} = 0.91$	$d_{ft} = 0.983$
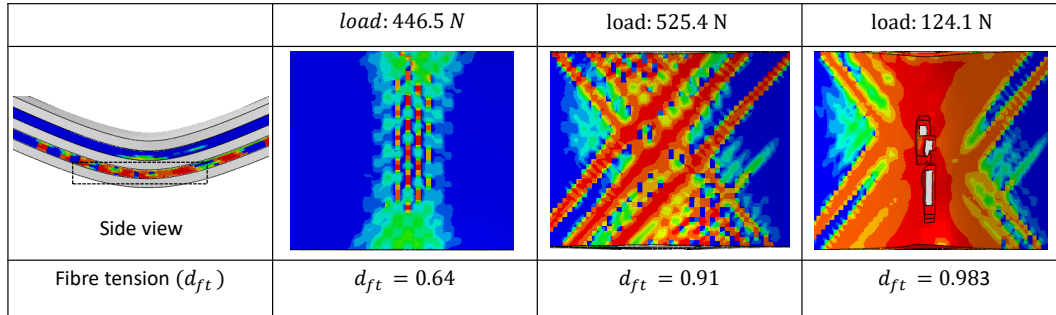
Figure 6.15: Fibre tensile damage (d_{ft}) at off-axis CARALL across various load levels

Above the neutral axis, (CF_1) experienced fibre kinking, as indicated by the fibre compressive damage (d_{fc}), as illustrated in Figure 6.16. Fibre compressive damage was initiated as a single line in the middle of ($CF_{11}, 45°$) at a load of 510.4 N. Subsequently, as the load approached the peak value in the force vs. displacement curve, multiple cracks propagated at the same location. As the load continued to increase, fibre kinking accumulated at the same layer, where the value of (d_{fc}) reached 0.95 at the final stage.

Matrix compressive damage (d_{mc}) was noticeable in both (CF_1) and (CF_2), but it was more evident in (CF_1). This damage mode initiated at a later stage in ($CF_{11}, 45°$), and approached a critical value near the peak of the force vs.

displacement curve, as shown in Figure 6.17 at a load of 521.0 N. Furthermore, d_{mc} accumulated at the central parts of the $(CF_{11}, 45°)$ lamina, indicating a localized stress concentration. For the (CF_2) the presence of (d_{mc}) was prior to the full failure of the specimen. However, more damage was observed in (CF_1), due to its exposure to higher compressive stress, being closer to the loading nose.
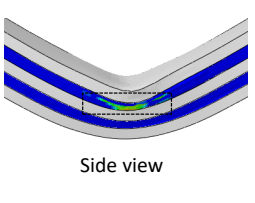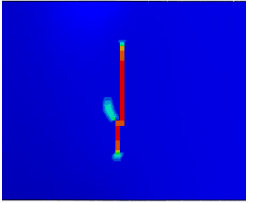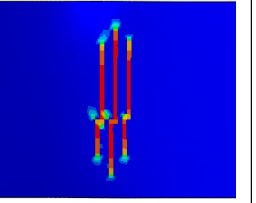
	load: 510.4 N	*load*: 523.3 N	*load*: 124.1 N
Side view			
Fibre compression (d_{fc})	$d_{fc} = 0.86$	$d_{fc} = 0.91$	$d_{fc} = 0.95$

Figure 6.16: Fibre compressive damage (d_{fc}) at off-axis CARALL across various load levels
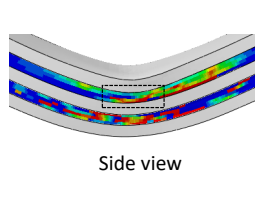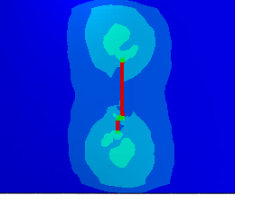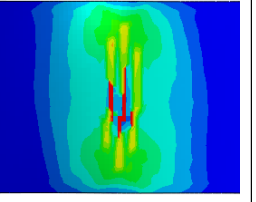
	load: 493.8 N	*load*: 521.0 N	*load*: 500.7 N
Side view			
Matrix tension (d_{mc})	$d_{mc} = 0.4578$	$d_{mc} = 0.99$	$d_{mc} = 0.99$

Figure 6.17: Matrix compressive damage (d_{mc}) at off-axis CARALL across various load levels

Progressive damage in aluminium layers

The progression of damage in aluminium layers is plotted in Figure 6.18 for the three layers in the off-axis CARALL across three stages. The damage initiated in the aluminium layers after passing the transition zone (point-B) in the F vs D curve. Where the damage initiated at the central area of the layers, as shown in Figure 6.18 at a load of 446.5 N. This led to an elliptical damage concentration, with a maximum value of JCCRT observed in (Al_3). The second column of Figure 6.18 captures the levels of plastic damage in aluminium layers prior to full

failure. At a load of 510.4 N, there is a noticeable increase in damage, especially in (Al_3), due to its exposure to the highest tensile stress among the layers. It is worth mentioning that the damage pattern in (Al_3) at this stage is affected by the fibre orientations in carbon fibre layers. The concentration of damage in this layer changed from an elliptical shape once the cracks appeared in the $(CF_{24}, 45°)$ layer parallel to the direction of the fibres. Moreover, at this stage, the damage values have also increased in both (Al_1) and (Al_2). During the final stage (124N), the elements were deleted from (Al_3) as it reached a fully failed state (1.0). This followed a dramatic increase in the damage of (Al_1) as it buckled under the influence of high compressive load, leading to an increase of the JCCRT value to 0.98. The middle aluminium layer (Al_2) also exhibited an increase in the damage value. Notably, the edges of (Al_2) have shown greater damage as they deformed extensively due to the buckling of (Al_1).

Progressive damage at Al/carbon fibre interface

The off-axis CARALL specimen experienced delamination primarily around the middle layers of the specimen when subjected to flexural loading. Delamination occurred at the most critical interfaces, as shown in Figure 6.19 at two stages. At the interface between CF_1 and Al_2 delamination occurs at the edges of the specimen with a CSMAXSCRT value of 0.76, as shown at 500.2 N in Figure 6.19. Further loading increased the delamination at almost the same location, with a value approaching 0.94. While for the interface between Al_2 and CF_2, delamination was approximately concentrated at the fibre angles orientation, this attributed to different stress states between the two layers. In other words, stress is concentrated at 45° in the CF_2 as fibres carry more load, leading to delamination along the direction of the fibres.

	Load: 446.5 *N*	*Load*: 510.4 *N*	*Load*: 124.1 *N*
Al-1	*max*: 0.07	*max*: 0.16	*max*: 0.98
Al-2	*max*: 0.034	*max*: 0.15	*max*: 0.42
Al-3	*max*: 0.15	*max*: 0.39	*max*: 1.0
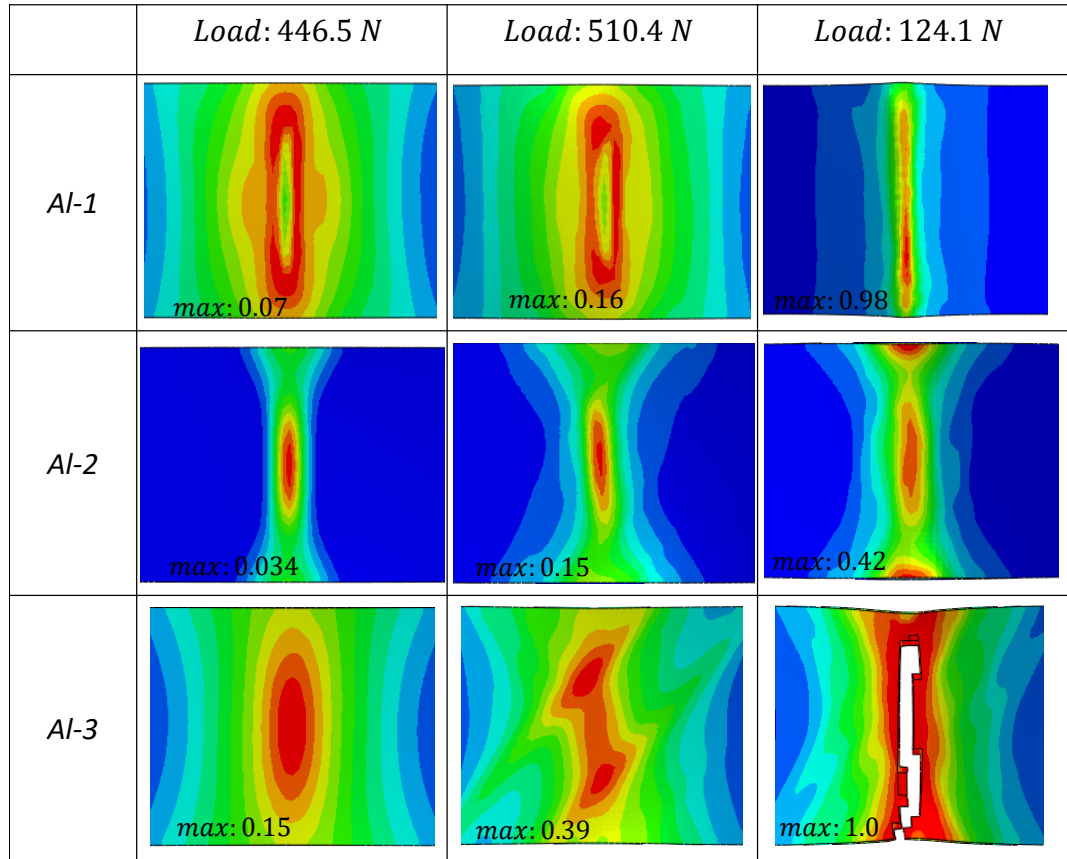
Figure 6.18: Johnson-cook damage ($JCCRT$) at off-axis CARALL across various load levels

load: 500.2 *N*	*load*: 521.0 *N*
max: 0.76	*max*: 0.94
Interface: $CF_{14}, 90°/Al_2$	Interface: $CF_{14}, 90°/Al_2$
max: 0.72	*max*: 1.0
Interface: $Al_2/CF_{21}, 90°$	Interface: $Al_2/CF_{21}, 90°$

Figure 6.19: Damage initiation at Al/carbon fibre interfaces in off-axis CARALL

6.7   Comparative analysis of the mechanical behaviour and failure Characteristics of on- and off-axis CARALL

This section highlights the differences between the flexural behaviour and failure mechanisms of the on-axis and off-axis CARALL specimens. Firstly, in terms of the force-displacement curve, the on-axis specimen showed higher force at failure, while the off-axis exhibited higher displacement at failure. At the point of failure, the on-axis specimen displayed a sudden drop in force, whereas the off-axis specimen showed a gradual decrease in force. Furthermore, the flexural strength and modulus of the on-axis CARALL are approximately 23.8% and 25.3% higher than those of the off-axis CARALL specimen.

In both cases stress concentration was initially observed at the Al_1 and Al_3, which are exposed to the highest compressive and tensile loads respectively. Prior to the yield point of aluminium, stress was concentrated at the $CF_{24}, 0°$ layer for the on-axis and at the $CF_{24}, 45°$ and $CF_{11}, 45°$ layers for the off-axis specimen. It was noted that stress is uniformly distributed across the layers of the on-axis specimen, while for the off-axis the stress was not uniform due to the off-axis fibre angles.

Both specimens showed two types of damage: fibre tensile/compressive and matrix tensile/compressive damage modes. In the on-axis specimen, each layer showed only one main damage mode. The 0° layers experienced fibre tensile/-compressive damage while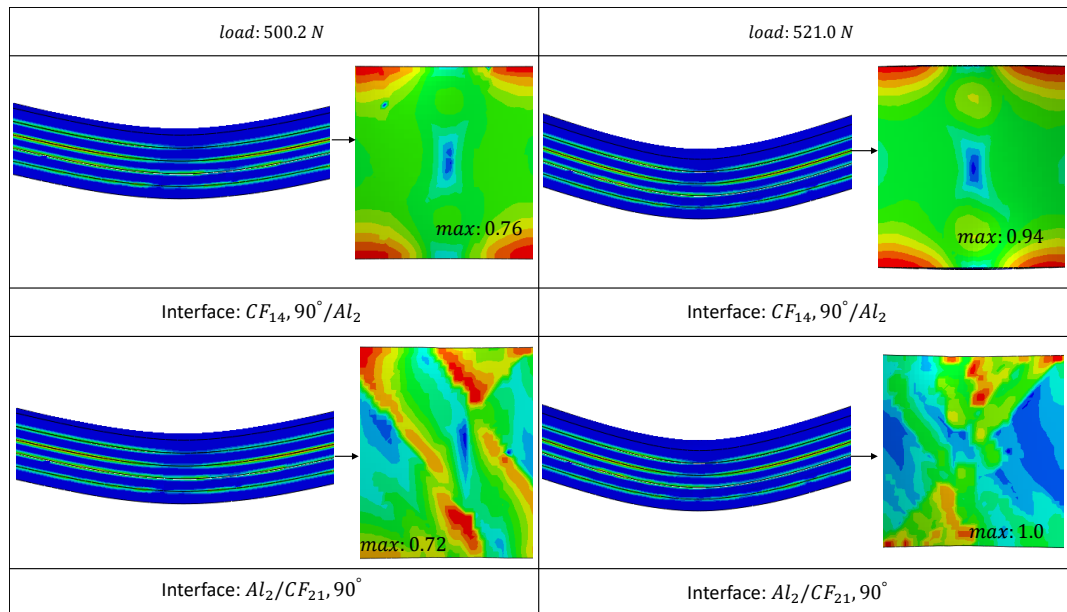 the 90° layers experienced matrix tensile/compressive damage. However, in the off-axis specimen, the two damage modes were evident in the ±45° layers. Since these layers were not loaded along their fibre direction, their load-bearing capacity was affected by both types of damage. This was also

concluded by Yuan Lin et al. [55] for an FML subjected to bending load. The occurrence of different types of damage within each specimen depends on the layer's position relative to the neutral axis. Carbon fibre layers located above the neutral axis tend to fail due to compressive damage modes, whereas layers positioned below the neutral axis fail due to tensile damage modes. Furthermore, the direction of cracks in carbon fibre layers was significantly affected by the fibre angles, specifically in the off-axis specimen.

Plastic deformation was observed in the aluminium layers of both the on and off-axis specimens. The central area of the layers in both specimens showed an elliptical pattern of damage concentration. However, it was found that plastic deformation was affected by the $\pm 45°$ fibre angles in the off-axis specimen. Additionally, the highest plastic deformation was observed in the bottom aluminium layer (Al_3) in both specimens since it is exposed to the highest tensile load. The main difference in plastic damage is in the damage of the (Al_1) and (Al_2). In the on-axis specimen, the highest plastic deformation was in (Al_2) once (Al_3) was fully damaged. However, in the off-axis case, more plastic damage was observed in the (Al_1) after the failure of (Al_3). This is attributed to the buckling that occurred in (Al_1) in the off-axis case due to the high deformation. Indeed the deformation at failure was $9.3mm$ in the off-axis case, while it was only $5.4mm$ in the on-axis specimen.

In conclusion, this chapter presented an analysis of CARALL's flexural behaviour and focused on the failure mechanisms occurring within its layers during testing. The developed framework, which includes Hashin's and Puck's failure criteria along with the Johnson-Cook and cohesive surface-based models, was used to simulate the progressive damage of CARALL constituents. This approach provided accurate and reliable predictions of CARALL's flexural behaviour in comparison

with both the existing literature and experimental data. Furthermore, this study provides an efficient tool for understanding damage progression at the layer level in FMLs.

Chapter 7

Conclusions and future work

7.1 Conclusions

A numerical framework aiming at predicting the behaviour and failure mechanisms in FMLs has been proposed in this research, which combined material models and failure criteria for metals and composite materials. The framework included damage models for assessing the plastic deformation of the metal layers as well as a surface-based cohesive model for assessing the delamination at the interface between the metal and composite layers. Within the framework, a novel 3D constitutive model has been proposed for predicting the damage in composites. The model adopts physically-based failure criteria for predicting the damage initiation in fibres and matrix within the composite lamina. The damage in fibres is assessed at the fibres coordinate system, while the matrix damage is assessed on a new coordinate system aligned with the fracture plane orientation. The fracture plane is obtained with a computationally efficient algorithm that combines two numerical methods: the golden search and the parabolic interpolation. The implementation of this algorithm showed approximately 50%

reduction in computational time when compared to the traditional method. The damage propagation in composites was implemented by reducing the stiffness of the material according to criteria based on the equivalent strain and stress, where the damage evolution model was modified to suit the selected damage initiation criteria. Furthermore, crack paths were simulated by deleting the elements which approach a critical value. This constitutive model was written in a user-material subroutine and linked with Abaqus/Explicit. The proposed constitutive model showed excellent agreement with stress-strain curves of experimental tensile test of CFRP specimens. Additionally, it predicted fibre breakage in the 0° specimen and matrix cracking in the 90° specimen.

The framework was applied to simulate the complex behaviour and failure mechanisms of GLARE in the open-hole tensile test. FE models were constructed for on-axis and off-axis GLARE tests, the models were verified with mesh sensitivity studies and validated against experimental results. The FE models were able to reproduce the experimental stress-strain curves of the on-axis and off-axis GLARE with excellent agreement. In addition, the models simulated various failure mechanisms, including Fibre breakage/kinking, matrix cracking, delamination and plastic deformation in the aluminium layers. The initiation and propagation of these damage mechanisms were recorded and discussed for each layer. Moreover, a comparative analysis has been carried out between the two specimens, focusing on the effect of fibre orientation on the failure behaviour of GLARE.

Furthermore, the current developed framework was applied for simulating the flexural test of CARALL. Where an FE model was constructed for the full experimental setup considering on-axis and off-axis specimens. The model was verified with a mesh convergence study and validated with experimental results. Force-

displacement curves were obtained from the FE-models where they show good agreement with experimental data. The damage mechanisms in CARALL layers were recorded at multiple stages of the (FvsD) curve. Where fibre breakage/kinking, matrix cracking, delamination and plastic deformation were observed at the CARALL layers. In addition, the progressive failure behaviour of the two specimens was compared to highlight the effect of fibre angle orientations on the failure behaviour of CARALL.

This study provided an efficient and reliable numerical tool for assessing the progressive damage in FML structures. This tool is beneficial for a wide range of engineering applications, particularly in assessing the behaviour of aerospace structures. During the design stage of aircraft development, this numerical tool could improve the testing campaigns' efficiency by offering a cost-effective means of investigating the complex failure mechanisms such as Fibre breakage/kinking, matrix cracking, delamination and plastic deformation. As a result, it can reduce the number of experimental tests required to assess failure behaviour in aerospace structures. Moreover, this tool is capable of visualising internal cracks within the structure in a 3D environment, which might be challenging to detect with traditional experimental techniques.

7.2 Future work

The research presented in this thesis focused on the development of a numerical framework for FMLs and was applied to two case studies. The following points provide suggestions for applications and further developments.

- This thesis provided a numerical model that is easy to implement in Explicit finite element software. The same model could be applied for studying the behaviour of various FMLs under different loading scenarios such as static,

and dynamic tests.

- The current model could be improved by including a more advanced approach to predict delamination within FMLs. This could involve cohesive layers instead of the cohesive-based surface currently being used. Although this approach might increase the computational time, it is expected to provide a more accurate prediction of delamination.

- Developing a multi-scale model that includes micro and meso-scale models will yield a more comprehensive framework. The micro-scale model will be used for determining the elastic properties of the composite lamina based on the specific properties of the fibres and matrix as well as the fibre volume fraction. Then these properties could be applied in meso or macro scale models.

- Developing a mesh optimization tool that aligns the mesh with fibre angle orientations could potentially enhance crack path prediction in composites, as proposed by [24,51,53,65]. However, additional experiments are required for validation. As the current literature lacks clear experimental results for crack paths in FMLs with multiple fibre ordinations.

- Investigating fibre angle reorientation during loading in composite layers within FMLs could improve the understanding of their mechanical behaviour. Although fibre angles are expected to slightly shift under load, these changes are not well-researched with numerical methods. A potential approach to capture this effect is by adding cohesive layers between the individual composite plies.

Bibliography

[1] René Alderliesten. *Fatigue and fracture of fibre metal laminates*, volume 236. Springer, 2017.

[2] D.H. Allen, C.E. Harris, and S.E. Groves. A thermomechanical constitutive theory for elastic composites with distributed damage—i. theoretical development. *International Journal of Solids and Structures*, 23(9):1301–1318, 1987.

[3] Zohreh Asaee, Shahin Shadlou, and Farid Taheri. Low-velocity impact response of fiberglass/magnesium fmls with a new 3d fiberglass fabric. *Composite Structures*, 122:155–165, 2015.

[4] Standard Test Method for Tensile Properties of Polymer Matrix Composite Materials. D3039, ASTM International, West Conshohocken, PA, November 2017.

[5] Standard Test Method for Flexural Properties of Polymer Composite Materials. D7264, ASTM International, West Conshohocken, PA, January 2021.

[6] Ever J Barbero. *Introduction to composite materials design*. CRC press, 2010.

[7] Ever J. Barbero. *Finite Element Analysis of Composite Materials using Abaqus™*. Taylor Francis Group, 2013.

[8] Zdeněk P Bažant and Byung H Oh. Crack band theory for fracture of concrete. *Matériaux et construction*, 16:155–177, 1983.

[9] Costanzo Bellini, Vittorio Di Cocco, Francesco Iacoviello, and Larisa Patricia Mocanu. Numerical modelling of fibre metal laminate flexural behaviour. *Material Design & Processing Communication*, 2022(1):3401406.

[10] Ravindranadh Bobbili, Vemuri Madhu, and Ashok Kumar Gogia. Tensile behaviour of aluminium 7017 alloy at various temperatures and strain rates. *Journal of Materials Research and Technology*, 5(2):190–197, 2016.

[11] Edson Cocchieri Botelho, Rogério Almeida Silva, Luiz Cláudio Pardini, and Mirabel Cerqueira Rezende. A review on the development and properties of continuous fiber/epoxy/aluminum hybrid composites for aircraft structures. *Materials Research*, 9:247–256, 2006.

[12] Fernando Cepero-Mejias. *Advanced Finite Element Strategies for Machining of Long Fibre Reinforced Polymer Composites*. University of Sheffield, 2021.

[13] Trevor William Clyne and Derek Hull. *An introduction to composite materials*. Cambridge university press, 2019.

[14] P. Cortes and W. J. Cantwell. The tensile and fatigue properties of carbon fiber-reinforced peek-titanium fiber-metal laminates. *Journal of Reinforced Plastics and Composites*, 23(15):1615–1623, 2004.

[15] P Cortes and WJ Cantwell. The prediction of tensile failure in titanium-based thermoplastic fibre–metal laminates. *Composites science and technology*, 66(13):2306–2316, 2006.

[16] J.L. Curiel Sosa and N. Karapurath. Delamination modelling of glare using the extended finite element method. *Composites Science and Technology*, 72(7):788–791, 2012.

[17] O. Das, N.K. Kim, and D. Bhattacharyya. 16 - the mechanics of biocomposites. In Luigi Ambrosio, editor, *Biomedical Composites (Second Edition)*, Woodhead Publishing Series in Biomaterials, pages 375–411. Woodhead Publishing, second edition edition, 2017.

[18] T.J. De Vries. Blunt and sharp notch behaviour of glare laminates. *Ph.D dissertation*, 2001.

[19] H Matthias Deuschle and Bernd-H Kröplin. Finite element implementation of puck's failure theory for fibre-reinforced composites under three-dimensional stress. *Journal of Composite Materials*, 46(19-20):2485–2513, 2012.

[20] H Matthias Deuschle and Alfred Puck. Application of the puck failure theory for fibre-reinforced composites under three-dimensional stress: Comparison with experimental results. *Journal of Composite Materials*, 47(6-7):827–846, 2013.

[21] Gurpinder S Dhaliwal and Golam M Newaz. Experimental and numerical investigation of flexural behavior of carbon fiber reinforced aluminum laminates. *Journal of Reinforced Plastics and Composites*, 35(12):945–956, 2016.

[22] Dandan Du, Yubing Hu, Huaguan Li, Cheng Liu, and Jie Tao. Open-hole tensile progressive damage and failure prediction of carbon fiber-reinforced peek–titanium laminates. *Composites Part B: Engineering*, 91:65–74, 2016.

[23] George Dvorak. *Micromechanics of composite materials*, volume 186. Springer Science & Business Media, 2012.

[24] O. Falcó, R.L. Ávila, B. Tijs, and C.S. Lopes. Modelling and simulation methodology for unidirectional composite laminates in a virtual test lab framework. *Composite Structures*, 190:137–159, 2018.

[25] Shiyi Gao, Wenbin Hou, Jianing Xing, and Lin Sang. Numerical and experimental investigation of flexural properties and damage behavior of cfrtp/al laminates with different stacking sequence. *Applied Sciences*, 13(3), 2023.

[26] JoséMiranda Guedes and Noboru Kikuchi. Preprocessing and postprocessing for materials based on the homogenization method with adaptive finite element methods. *Computer Methods in Applied Mechanics and Engineering*, 83(2):143–198, 1990.

[27] Fang Guo-dong, Liang Jun, and Wang Bao-lai. Progressive damage and nonlinear analysis of 3d four-directional braided composites under unidirectional tension. *Composite Structures*, 89(1):126–133, 2009.

[28] WenQin Han, KeJun Hu, QingHe Shi, and FuXian Zhu. Damage evolution analysis of open-hole tensile laminated composites using a progress damage model verified by ae and dic. *Composite Structures*, 247:112452, 2020.

[29] Z. Hashin. Failure criteria for unidirectional fiber composites. *Journal of Applied Mechanics*, 48(4):846–852, 06 1980.

[30] Z. Hashin and A. Rotem. A fatigue failure criterion for fiber reinforced materials. *Journal of Composite Materials*, 7(4):448–464, 1973.

[31] B. Hassani and E. Hinton. A review of homogenization and topology opimization ii—analytical and numerical solution of homogenization equations. *Computers Structures*, 69(6):719–738, 1998.

[32] B. Hassani and E. Hinton. A review of homogenization and topology optimization iii—topology optimization using optimality criteria. *Computers Structures*, 69(6):739–756, 1998.

[33] B. Hassani and E. Hinton. A review of homogenization and topology optimization i—homogenization theory for media with periodic structure. *Computers Structures*, 69(6):707–717, 1998.

[34] Wentao He, Changzi Wang, Shuqing Wang, Lu Yao, Linfeng Wang, and De Xie. Characterizing and predicting the tensile mechanical behavior and failure mechanisms of notched fmls—combined with dic and numerical techniques. *Composite Structures*, 254:112893, 2020.

[35] Wentao He, Changzi Wang, Shuqing Wang, Lu Yao, Jun Wu, and De Xie. Tensile mechanical behavior and failure mechanisms of multihole fiber metal

laminates—experimental characterization and numerical prediction. *Journal of Reinforced Plastics and Composites*, 39(13-14):499–519, 2020.

[36] Alton L. Highsmith and Kenneth L. Reifsnider. Stiffness-reduction mechanisms in composite laminates. *ASTM special technical publications*, pages 103–117, 1982.

[37] R. Hill. Elastic properties of reinforced solids: Some theoretical principles. *Journal of the Mechanics and Physics of Solids*, 11(5):357–372, 1963.

[38] Rodney Hill. *The mathematical theory of plasticity*, volume 11. Oxford university press, 1998.

[39] MJ Hinton and AS Kaddour. The background to the second world-wide failure exercise. *Journal of Composite Materials*, 46(19-20):2283–2294, 2012.

[40] Changzhi Hu, Lin Sang, Kai Jiang, Jianing Xing, and Wenbin Hou. Experimental and numerical characterization of flexural properties and failure behavior of cfrp/al laminates. *Composite Structures*, 281:115036, 2022.

[41] P. Iaccarino, A. Langella, and G. Caprino. A simplified model to predict the tensile and shear stress–strain behaviour of fibreglass/aluminium laminates. *Composites Science and Technology*, 67(9):1784–1793, 2007.

[42] Kai Jin, Hao Wang, Jie Tao, and Dandan Du. Mechanical analysis and progressive failure prediction for fibre metal laminates using a 3d constitutive model. *Composites Part A: Applied Science and Manufacturing*, 124:105490, 2019.

[43] L M Kachanov. On the time to failure under creep conditions. *Izv AN SSSR, Otd Tekhn*, 8:26–31, 1958.

[44] Sasanka Kakati and D. Chakraborty. Delamination in glare laminates under low velocity impact. *Composite Structures*, 240:112083, 2020.

[45] M. Kawai, M. Morishita, S. Tomura, and K. Takumida. Inelastic behavior and strength of fiber-metal hybrid composite: Glare. *International Journal of Mechanical Sciences*, 40(2):183–198, 1998.

[46] SMR Khalili, V Daghigh, and R Eslami Farsani. Mechanical behavior of basalt fiber-reinforced and basalt fiber metal laminate composites under tensile and bending loads. *Journal of Reinforced Plastics and Composites*, 30(8):647–659, 2011.

[47] Martin Knops. *Analysis of failure in fiber polymer laminates: the theory of Alfred Puck.* Springer, 2008.

[48] Akira Kuraishi, Stephen W Tsai, and Kevin K.S Liu. A progressive quadratic failure criterion, part b. *Composites Science and Technology*, 62(12):1683–1695, 2002.

[49] V.I. Kushch, S.V. Shmegera, P. Brøndsted, and L. Mishnaevsky. Numerical simulation of progressive debonding in fiber reinforced composite under transverse loading. *International Journal of Engineering Science*, 49(1):17–29, 2011. Recent Advances in Micromechanics of Materials.

[50] Ireneusz Lapczyk and Juan A. Hurtado. Progressive damage modeling in fiber-reinforced materials. *Composites. Part A, Applied science and manu-*

facturing, 38(11):2333–2341, 2007.

[51] Tobias Laux, Khong Wui Gan, Rodrigo P. Tavares, Carolina Furtado, Albertino Arteiro, Pedro P. Camanho, Ole T. Thomsen, and Janice M. Dulieu-Barton. Modelling damage in multidirectional laminates subjected to multi-axial loading: Ply thickness effects and model assessment. *Composite Structures*, 266:113766, 2021.

[52] Woei-Shyan Lee and Zih-Chao Tang. Relationship between mechanical properties and microstructural response of 6061-t6 aluminum alloy impacted at elevated temperatures. *Materials Design*, 58:116–124, 2014.

[53] Frank A Leone and Brian P Justusson. Effects of characteristic element length on fracture energy dissipation in continuum damage mechanics models. *Journal of Composite Materials*, 55(24):3551–3566, 2021.

[54] Mengze Li, Shuran Li, Yu Tian, Haowei Zhang, Weidong Zhu, and Yinglin Ke. Bottom-up stochastic multiscale model for the mechanical behavior of multidirectional composite laminates with microvoids. *Composites Part A: Applied Science and Manufacturing*, 181:108144, 2024.

[55] Yuan Lin, Yaxin Huang, Teng Huang, Binbin Liao, Dongdong Zhang, and Cong Li. Characterization of progressive damage behaviour and failure mechanisms of carbon fibre reinforced aluminium laminates under three-point bending. *Thin-Walled Structures*, 135:494–506, 2019.

[56] Yuan Lin, Yaxin Huang, Teng Huang, and Zhuchen Yin. Open-hole tensile behaviour and failure prediction of carbon fibre reinforced aluminium laminates. *Polymer composites*, 39(11):4123–4138, 2018.

[57] Peter Linde and Henk de Boer. Modelling of inter-rivet buckling of hybrid composites. *Composite Structures*, 73(2):221–228, 2006. International Conference on Buckling and Postbuckling Behavior of Composite Laminated Shell Structures.

[58] Cheng Liu, Dandan Du, Huaguan Li, Yubing Hu, Yiwei Xu, Jingming Tian, Gang Tao, and Jie Tao. Interlaminar failure behavior of glare laminates under short-beam three-point-bending load. *Composites Part B: Engineering*, 97:361–367, 2016.

[59] Ren-Horng Maa and Jung-Ho Cheng. A cdm-based failure model for predicting strength of notched composite laminates. *Composites Part B: Engineering*, 33(6):479–489, 2002.

[60] P Maimí, Pedro Ponces Camanho, JA Mayugo, and CG Dávila. A continuum damage model for composite laminates: Part ii–computational implementation and validation. *Mechanics of materials*, 39(10):909–919, 2007.

[61] PK Mallick. Materials, manufacturing, and design. *Mechanical Engineering (Marcel Dekker, Inc.)*, 83:74–81, 2007.

[62] G Thomas Mase, Ronald E Smelser, and George E Mase. *Continuum mechanics for engineers*. CRC press, 2009.

[63] Frank L. Matthews. Glare: History of the development of a new aircraft material a. vlot kluwer academic publishers, po box 17, 3300 aa dordrecht, the netherlands. 2001. 222pp. £30. isbn 140200124x. *The Aeronautical Journal*, 106(1057):154–154, 2002.

[64] A. Matzenmiller, J. Lubliner, and R.L. Taylor. A constitutive model for anisotropic damage in fiber-composites. *Mechanics of Materials*, 20(2):125–152, 1995.

[65] S.L.J. Millen, Z. Ullah, and B.G. Falzon. On the importance of finite element mesh alignment along the fibre direction for modelling damage in fibre-reinforced polymer composite laminates. *Composite Structures*, 278:114694, 2021.

[66] Fernando Naya Montáns. Prediction of mechanical properties of unidirectional frp plies at different environmental conditions by means of computational micromechanics. 2017.

[67] Mohsen Naghdinasab, Amin Farrokhabadi, and Hamidreza Madadi. A numerical method to evaluate the material properties degradation in composite rves due to fiber-matrix debonding and induced matrix cracking. *Finite Elements in Analysis and Design*, 146:84–95, 2018.

[68] D.R. Nolan, C. Lally, and J.P. McGarry. Understanding the deformation gradient in abaqus and key guidelines for anisotropic hyperelastic user material subroutines (umats). *Journal of the Mechanical Behavior of Biomedical Materials*, 126:104940, 2022.

[69] Monika Ostapiuk, Jarosław Bieniaś, and Barbara Surowska. Analysis of the bending and failure of fiber metal laminates based on glass and carbon fibers. *Science and Engineering of Composite Materials*, 25(6):1095–1106, 2018.

[70] Federico Paris and Karen E Jackson. A study of failure criteria of fibrous

composite materials. Technical report, 2001.

[71] Silvestre Pinho, Carlos Dávila, Pedro Camanho, Lorenzo Iannucci, and P. Robinson. Failure models and criteria for frp under in-plane or three-dimensional stress states including shear non-linearity. Technical report, 03 2005.

[72] Hemaraju Pollayi and Wenbin Yu. Modeling matrix cracking in composite rotor blades within vabs framework. *Composite Structures*, 110:62–76, 2014.

[73] William H. Press, Saul A. Teukolsky, William T. Vetterling, and Brian P. Flannery. Numerical recipes in c. *SMR*, 693(1):59–70, 1992.

[74] A. Puck, J. Kopp, and M. Knops. Guidelines for the determination of the parameters in puck's action plane strength criterion. *Composites Science and Technology*, 62(3):371–378, 2002.

[75] A. Puck and H. Schürmann. Failure analysis of frp laminates by means of physically based phenomenological models. *Composites Science and Technology*, 58(7):1045–1067, 1998.

[76] A. Puck and H. Schürmann. Failure analysis of frp laminates by means of physically based phenomenological models as. *Composites and Technology*, 62(12):1633–1662, 2002.

[77] Y N Rabotnov. On the equations of state for creep. In *Progress in Applied Mechanics: The Prager Anniversary Volume (W. T. Koiter*. McMillan, New York (USA, 1963.

[78] Seyed Saeid Rahimian Koloor, Atefeh Karimzadeh, Noorfaizal Yidris, Michal Petrů, Majid Reza Ayatollahi, and Mohd Nasir Tamin. An energy-based concept for yielding of multidirectional frp composite structures using a mesoscale lamina damage model. *Polymers*, 12(1), 2020.

[79] Ali Rajabi, Mehran Kadkhodayan, and Sadegh Ghanei. An investigation into the flexural and drawing behaviors of gfrp based fiber-metal laminate. *Mechanics of Advanced Materials and Structures*, 03 2017.

[80] Pavuluri MV Rao and VV Subba Rao. Degradation model based on tsai-hill factors to model the progressive failure of fiber metal laminates. *Journal of composite materials*, 45(17):1783–1792, 2011.

[81] J. Reinoso, G. Catalanotti, A. Blázquez, P. Areias c, P.P. Camanhod, and F. Parísa. A consistent anisotropic damage model for laminated fiber-reinforced composites using the 3d-version of the puck failure criterion. *International Journal of Solids and Structures*, 126:37–53, 2017.

[82] M. Rezasefat, Daniel Badel Torres, Alvaro Gonzalez-Jimenez, M. Giglio, and A. Manes. A fast fracture plane orientation search algorithm for puck's 3d iff criterion for ud composites. *Materials Today Communications*, 28:102700, 2021.

[83] Ebrahim Sadeghpour, Mojtaba Sadighi, and Soheil Dariushi. An investigation on blunt notch behavior of fiber metal laminates containing notch with different shapes. *Journal of Reinforced Plastics and Composites*, 32(15):1143–1152, 2013.

[84] F.J. Schirmaier, J. Weiland, L. Kärger, and F. Henning. A new efficient

and reliable algorithm to determine the fracture angle for puck's 3d matrix failure criterion for ud composites. *Composites Science and Technology*, 100:19–25, 2014.

[85] Ankush P. Sharma, R. Velmurugan, K. Shankar, and SK Ha. High-velocity impact response of titanium-based fiber metal laminates. part i: experimental investigations. *International Journal of Impact Engineering*, 152:103845, 2021.

[86] Michael Smith. *ABAQUS/Standard User's Manual, Version 6.9*. Dassault Systèmes Simulia Corp, United States, 2009.

[87] M. Stroeven, H. Askes, and L.J. Sluys. Numerical determination of representative volumes for granular materials. *Computer Methods in Applied Mechanics and Engineering*, 193(30):3221–3238, 2004. Computational Failure Mechanics.

[88] C.T. Sun and Yuting Rui. Orthotropic elasto-plastic behavior of as4/peek thermoplastic composite in compression. *Mechanics of Materials*, 10(1):117–125, 1990.

[89] C.T Sun and Jianxin Tao. Prediction of failure envelopes and stress/strain behaviour of composite laminates. *Composites Science and Technology*, 58(7):1125–1136, 1998.

[90] Ramesh Talreja. Stiffness properties of composite laminates with matrix cracking and interior delamination. *Engineering Fracture Mechanics*, 25(5):751–762, 1986.

[91] W. Tan, F. Naya, L. Yang, T. Chang, B.G. Falzon, L. Zhan, J.M. Molina-Aldareguía, C. González, and J. Llorca. The role of interfacial properties on the intralaminar and interlaminar damage behaviour of unidirectional composite laminates: Experimental characterization and multiscale modelling. *Composites Part B: Engineering*, 138:206–221, 2018.

[92] Wei Tan and Brian G. Falzon. Modelling the crush behaviour of thermoplastic composites. *Composites Science and Technology*, 134:57–71, 2016.

[93] M. Thomas, N. Boyard, L. Perez, Y. Jarny, and D. Delaunay. Representative volume element of anisotropic unidirectional carbon–epoxy composite with high-fibre volume fraction. *Composites Science and Technology*, 68(15):3184–3192, 2008.

[94] S. W. Tsai. *"Strength Theories of Filamentary Structures," Fundamental aspects of fiber reinforced plastic composites.* Wiley-Interscience, 1968.

[95] Stephen W Tsai. A survey of macroscopic failure criteria for composite materials. *Journal of Reinforced Plastics and Composites*, 3(1):40–62, 1984.

[96] Stephen W Tsai and Edward M Wu. A general theory of strength for anisotropic materials. *J. Compos. Mater.*, 5(1):58–80, January 1971.

[97] A. Turon, P.P. Camanho, J. Costa, and C.G. Dávila. A damage model for the simulation of delamination in advanced composites under variable-mode loading. *Mechanics of Materials*, 38(11):1072–1089, 2006.

[98] L. Távara, V. Mantič, E. Graciani, and F. París. Modelling interfacial debonds in unidirectional fibre-reinforced composites under biaxial trans-

verse loads. *Composite Structures*, 136:305–312, 2016.

[99] Ad Vlot and Jan Willem Gunnink. *Fibre metal laminates: an introduction.* Springer Science & Business Media, 2001.

[100] LB Vogelesang. Fibre metal laminates; the development of a new family of hybrid materials. In *Proceedings of the 22rd fatigue of aeronautical structures as an engineering challenge, ICAF symposium*, pages 1–21. EMAS publishing, 2003.

[101] J.M. Whitney. On the 'ply discount method' for determining effective thermo-elastic constants of laminates containing transverse cracks. *Composites Part A: Applied Science and Manufacturing*, 36(10):1347–1354, 2005. Special Issue Honouring Jack Vinson on his 75th Birthday.

[102] J. Wiegand, N. Petrinic, and B. Elliott. An algorithm for determination of the fracture angle for the three-dimensional puck matrix failure criterion for ud composites. *Composites Science and Technology*, 68(12):2511–2517, 2008. Deformation and Fracture of Composites: Analytical, Numerical and Experimental Techniques, with regular papers.

[103] Guocai Wu and Jenn-Ming Yang. Analytical modelling and numerical simulation of the nonlinear deformation of hybrid fibre–metal laminates. *Modelling and Simulation in Materials Science and Engineering*, 13(3):413, 2005.

[104] Lu Yao, Lizhou Mao, Yanchao Wang, Wentao He, Yan Ma, and Hang Yu. In-situ damage monitoring and numerical characterization of three-point bending and incremental cycle flexural behavior of fmls. *Mechanics*

of Advanced Materials and Structures, pages 1–19, 2023.

[105] Po-Ching Yeh, Po-Yu Chang, Jenn-Ming Yang, Peter H Wu, and Ming C Liu. Blunt notch strength of hybrid boron/glass/aluminum fiber metal laminates. *Materials Science and Engineering: A*, 528(4-5):2164–2173, 2011.

[106] Donghyun Yoon, Sangdeok Kim, Jaehoon Kim, and Youngdae Doh. Development and evaluation of crack band model implemented progressive failure analysis method for notched composite laminate. *Applied Sciences*, 9(24):5572, 2019.

[107] Kequan Yu, Lingzhi Li, Jiangtao Yu, Yichao Wang, Junhong Ye, and QingFeng Xu. Direct tensile properties of engineered cementitious composites: A review. *Construction and Building Materials*, 165:346–362, 2018.

[108] Guoqi Zhang, Bing Wang, Li Ma, Jian Xiong, Jinshui Yang, and Linzhi Wu. The residual compressive strength of impact-damaged sandwich structures with pyramidal truss cores. *Composite Structures*, 105:188–198, 2013.

[109] Xia Zhou, Yuting Zhao, Xingchi Chen, Zifan Liu, Junlei Li, and Yafu Fan. Fabrication and mechanical properties of novel cfrp/mg alloy hybrid laminates with enhanced interface adhesion. *Materials Design*, 197:109251, 2021.

Appendix A

Failure theories

Puck 2D [75]:

Fibre failure ($\sigma_{11} \geq 0$)

$$\frac{1}{\epsilon_{1T}} \left(\epsilon_1 + \frac{v_{f12}}{E_{f1}} m_{\sigma f} \sigma_2 \right) = 1 \tag{A.1}$$

Fibre compression ($\sigma_{11} < 0$)

$$\frac{1}{\epsilon_{1C}} \left| \left(\epsilon_1 + \frac{v_{f12}}{E_f 1} m_{\sigma f} \sigma_2 \right) \right| + (10\gamma_{21})^2 = 1 \tag{A.2}$$

Matrix Mode A ($\sigma_{22} \geq 0$)

$$\sqrt{\left(\frac{\sigma_{12}}{R_{\perp\|}^A} \right)^2 + \left(1 - \frac{p_{\perp}^{(+)}}{R_{\perp\|}^A} R_{\perp}^{(+)A} \right)^2 \left(\frac{\sigma_{22}}{R_{\perp}^{(+)A}} \right)^2} + \frac{p_{\perp\|}^{(+)}}{R_{\perp\|}^A} \sigma_{22} \geq 1 \tag{A.3}$$

Matrix Mode B $\left(\sigma_{22} < 0 \text{ and } \sigma_{22} > -R_{\perp 1}^{A}\right)$

$$\sqrt{\left(\frac{\sigma_{12}}{R_{\perp\parallel}^{A}}\right)^{2} + \left(\frac{p}{R}\right)^{2}\sigma_{22}^{2}} + \left(\frac{p}{R}\right)\sigma_{22} \geq 1 \tag{A.4}$$

Matrix Mode C $\left(\sigma_{22} \leq -R_{\perp\perp}^{A}\right)$

$$\frac{1}{2\left[1 + \left(\frac{p}{R}\right)R_{\perp\perp}^{A}\right]} \left[\left(\frac{\sigma_{12}}{R_{\perp\parallel}^{A}}\right)^{2} + \left(\frac{\sigma_{22}}{R_{\perp\perp}^{A}}\right)^{2}\right] \frac{R_{\perp\perp}^{A}}{-\sigma_{22}} \geq 1 \tag{A.5}$$

Definitions:

$$R_{\perp\perp}^{A} = \frac{Y_{C}}{2\left(1 + p_{\perp\perp}^{(-)}\right)} \tag{A.6}$$

$$\left(\frac{p}{R}\right) = \frac{p_{\perp\parallel}^{(-)}}{R_{\perp\parallel}^{A}} \tag{A.7}$$